DCE-MRI for assessment of hypoxia-induced prostate cancer aggressiveness

Torgeir Mo

Thesis presented for the degree of
Master of Science

Department of Physics
University of Oslo
May 2016

2016
DCE-MRI for assessement of hypoxia-induced prostate cancer aggressiveness
Torgeir Mo
http://www.duo.uio.no
Trykk: Reprosentralen, Universitetet i Oslo

Abstract

Prostate cancer is a disease characterized by severely heterogeneous behavior. Some tumors remain indolent, and without risk for the patient for many years, while others can progress to life threatening disease rapidly. This represents a challenge when choosing therapeutic modalities for patients diagnosed with prostate cancer, as the aggressiveness of the therapy should be in concordance with the aggressiveness of the disease. The clinical management of prostate cancer continues to be controversial, without clear consensus on choice of diagnostic tests or treatment modality. In this study the potential of using functional magnetic resonance imaging(MRI) to assess the aggressiveness of prostate cancer has been explored, and parameters obtained from dynamic contrast enhanced(DCE) MRI have been correlated to clinical data obtained from biopsies and post-surgical examinations of the prostate gland. Particularly the prognostic power of hypoxia levels, and the ability of MRI to reflect the levels of hypoxia have been examined.

The aims of this study is to combine and correlate data from functional MRI, molecular signatures of hypoxia, and tumor hypoxia, with the goal being prediction of prostate cancer aggressiveness. The endpoints of prostate cancer aggressiveness in this study is the clinical data obtained from assessment of histopathological specimens at the time of surgery.

This project included 79 patients diagnosed with intermediate and high-risk prostate cancer(D'Amico risk classification), referred to Oslo University Hospital, Radiumhospitalet, for surgical treatment. In vivo functional MRI examination, DCE imaging of the prostate, were preformed on the patients within a few days prior to surgery. Within 24 hours prior to surgery the patients received a dose of pimonidazole, either intravenously or orally, by pill, to act as a hypoxia marker which was used to assess the hypoxia in the prostatectomy specimens after the surgery.

The dynamic images provided have been analyzed using pharmacokinetic

models, to obtain parameters that relates to the tumor physiology, and in particular, to parametrize the blood perfusion in the tumor. The blood perfusion is assumed to be related to the distribution of oxygen, and thus the hypoxic regions can potentially be identified.

The methods used in this project were not able to reveal any strong correlations between the pharmacokinetic parameters and the pimonidazole staining, or between the pimonidazole staining and the clinical parameters commonly used for assessment of prostate cancer aggressiveness(Gleason score, Tumor- node- metastasis staging, and prostate specific antigen serum levels). Some weak correlation ($R = 0.40$, $p < 0.05$) were observed between pimonidazole staining and tumor size.

Acknowledgements

I would like to express my very great appreciation to my supervisors Therese Seierstad and Eirik Malinen, for their patient guidance, and enthusiastic follow up of my work. I would also like to thank Tord Hompland at the department of radiation biology at Radiumhospitalet, for helping me get to grips with the pharmacokinetic modeling, and the numerical calculations.

The staff and students at the bio- and medical physics group at the university also deserves an appreciative thanks, for never failing to provide good answers to more or less poorly constructed questions on everything from cellular metabolism to all things typographical, and for letting me listen to all the discussions taking place over lunch. I have probably gained more insight from listening in on discussions than from most of the scientific papers I have read throughout the past year.

Finally, I would like to extend my appreciation to all the staff at Radiumhospitalet (most of whom I have probably never met), who have been involved in providing me with the data used in this study.

Oslo, May 2016

Torgeir Mo

List of Abbreviations

AIF	Arterial input function
AUC	Area under RSI time-curve
CA	Contrast agent
cT	Clinical T-stage
DCE	Dynamic contrast enhanced
DW	Diffusion weighted
EES	Extravascular- extracellular space
HIF	Hypoxia inducible factor
iAUC	Initial area under RSI time-curve
MRI	Magnetic resonance imaging
PSA	Prostate specific antigen
pT	Pathological T-stage
ROI	Region of interest
RSI	Relative signal increase
SD	Standard deviation
T1W	T1 weighted
T2W	T2 weighted
TNM	Tumor Node Metastasis
TTP	Time to peak

Contents

1. Introduction

Prostate cancer is among the most frequently diagnosed cancers in the western world[14], and it is the single most common type of cancer in Norwegian men[28]. Over the past two decades the occurrence of prostate cancer in the western world, including Norway, has increased substantially, but the mortality rates has remained relatively constant. The increase in diagnosed prostate cancer incidence may be related to an increase in the use of Prostate-specific antigen(PSA)-testing for early diagnosis, improved biopsy techniques, or increased public awareness. It is not, however, reflected in the mortality rates related to prostate cancer. The disparity between reported incidence and mortality rate leads to the probable conclusion that only a small fraction of diagnosed low-risk prostate cancers will progress to life-threatening disease during the lifetime of the patient [14]. Yet, even though only a small proportion of patients diagnosed with prostate cancer will die from the disease, prostate cancer was, according to *Kreftregisteret*, the third most frequent cause of cancer-related deaths in Norway in 2014[39]. Prostate cancer is a heterogeneous disease with varied biology, and in some cases the disease can be aggressive and fatal if untreated, whilst many patients can remain symptom-free for a long time, even without any treatment. This represents a considerable challenge in making it difficult to predict the need for treatment in the individual patient. Patients with diagnosed prostate cancer run the risk of either being over- or under-treated. Over-treatment may result in unwanted, and unneeded complications related to surgery or radiation-therapy in patients who could have otherwise lived on with a non-aggressive prostate cancer. Under-treatment could result in patients dying, who could have otherwise been saved with a more aggressive treatment modality. In 2010 Hernes

et al. published a paper on treatment practice in Norway, where statistical data from *Kreftregisteret* were analyzed. Their data indicated some evidence of over-treatment of low-risk patients and under-treatment of intermediate- and high-risk patients[23].

A prerequisite for being able to offer correct treatment is reliable information on the prevalence and aggressiveness of the disease. This is today determined on a combined basis of clinical examination(digital rectal exploration and trans-rectal ultrasound), blood samples(determining the amount of prostate-specific antigen), and histological examination of tissue-biopsies. These examinations form the basis on which the treatment modality is chosen. However, clinical assessment of tumor aggressiveness and extent is limited by poor accuracy of digital rectal examination[21], and Histopatological evaluation of tumor aggressiveness is limited since less than one percent of the prostate gland is represented in the biopsies. Some tumors may also be inaccessible using trans-rectal biopsy. Therefore, preoperative biopsies may not demonstrate the most aggressive tumor[27][4]. Thus, there is a need for noninvasive diagnostic techniques to depict the extent and heterogeneity of the cancer with fairly high spatial resolution.

Hypoxia, or oxygen depletion, has been shown to correlate to poor prognosis, and poor treatment response in cancer[20], and is therefore a potential candidate as a bio-marker of cancer. Oxygen is transported to the tissue through diffusion from the capillaries, and has a limited diffusion range. Thus, the tissue needs to have a certain minimum capillary-density in order to stay sufficiently oxygenated. As a tumor grows it displaces the vasculature in the region, cutting off the oxygen supply to the tumor tissue, and construction of new blood vessels is required to oxygenate the tumor. The construction of blood vessels is done through the process of angiogenesis, but in tumors this process is highly unstructured, resulting in a chaotic capillary architecture. To ensure sufficient oxygenation the capillaries must be able to support enough blood-flow to allow enough oxygen to be available for diffusion into the tissue. Poorly constructed vascular architecture may result

in low blood flow, or low vascular permeability, resulting in hypoxic regions of tissue. Magnetic Resonance Imaging(MRI) has the potential ability to depict tissue characteristics, such as vascularization, blood-flow, cellularity, and vascular permeability, with a fairly high temporal and spatial resolution. MRI can thus assess tissue heterogeneity in both the time- and spatial dimensions, possibly identifying regions of potentially hypoxic tissue.

In 2010 a study was designed at *Radiumhospitalet* to examine to what degree advanced MR-techniques could be used to identify hypoxic tumors in prostate cancer. Patients having tumors with anticipated high metastatic potential according to D'Amico risk categories were subjected to a selection of different modalities of MR-examination, prior to a surgical removal of the prostate gland(prostatectomy). Prior to the surgery the hypoxia marker pimonidazole was also administered to the patients, so that the prostatectomy specimens could be immunostained and provide a measurement on the hypoxia of the tumor. The prostatectomy specimens also provides other pathological data to act as a gold standard, against which the MRI-analysis can be compared. The aim of this thesis is to use the Dynamic Contrast-Enhanced MR-images(DCE-MRI) provided by the study, and analyze the dynamics of the contrast agent(CA) in the tissue to obtain parameters describing the blood perfusion through the tumor. The goal is to be able to assess the vascular characteristics of the tumor, and compare them to the pathological data provided by the prostatectomy specimens.

2. Background

2.1 Prostate cancer

Cancers in general are characterized by abnormal growth of cells, which tends to proliferate in a manner that bypasses the regular control-mechanisms of cell-growth in the body. Cancer is a common term to describe several different diseases, all of which share the characteristics of abnormal cell growth and uncontrolled proliferation. Different cancer types do however display highly different biological behavior. Some cancer types can result in solid tumors, while others, like leukemia, does not. Even within cancers of the same type the biological behavior can be very different between individual cancers. Although the majority of cancer tumors arises from one singular cell, some tumors display a high degree of intra-tumor heterogeneity, meaning that the cells of the tumors display a large difference in phenotypic features, such as proliferation rate, metastatic potential, degree of differentiation, vascularization and metabolism [41].

2.1.1 Tumor physiology and vascularization

All cells require oxygen and nutrients to survive. These are transported to the cell by a complex network of blood vessels and capillaries in the organs called the vasculature. From the vasculature the oxygen and nutrients diffuse into the tissue and into the cells. As a tumor grows, it eventually reaches a size where passive diffusion of nutrients and oxygen is insufficient to sustain continued growth. As the diffusion limit for oxygen in tissue is about $100 - 200\mu m$, additional vasculature is required to reach the central cells of a large

tumor[26]. Accordingly, the tumor induces the production of new vessels through the process of angiogenesis. Angiogenesis is a process where new blood vessels are grown from preexisting vessels, and is a crucial step in the path to forming a solid tumor. Without angiogenesis a tumor cannot grow, and will remain small without any threat of progressing to lethal disease or to metastasize[16]. Angiogenesis is induced by an increase of the gene regulatory protein *Hypoxia Inducible Factor*-1α(HIF-1α), which is provoked in response to low oxygen levels[2], thus the process of angiogenesis is a response to low oxygen levels in the tissue. The vasculature produced from angiogenesis in tumors is, however, uniquely different from that of normal tissue[36], as it is characterized by vigorous and unstructured proliferation. The difference in vasculature in normal and tumor tissue, for three different tissue types, is shown in figure 2.1.

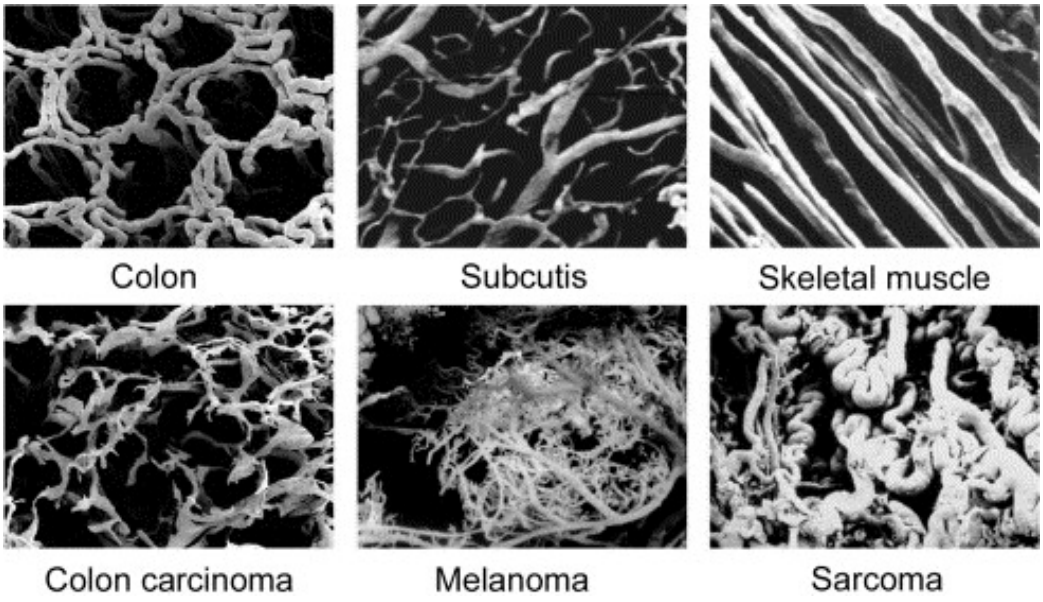

Figure 2.1: Illustration of the differences between cancerous tumors (lower panel) and the corresponding host tissue (upper panel) in terms of vascular architecture. The images shows the blood-vessel structure in three different types of tissues. The figure is taken from Vaupel[36].

The chaotic and vigorous way of creating the vasculature leads to structurally defective, leaky, and in terms of perfusion, ineffective micro-vessels.

In turn this results in irregular and heterogeneous blood flow[36][2]. The blood perfusion has also been shown to vary amongst different tumor types, different tumors of the same type, and to show large intra-tumor variations and temporal instability[17]. This abnormality of the blood flow is potentially detectable with dynamic contrast enhanced MRI, which detects the exchange of CA between tissue and vasculature.

2.1.2 Hypoxia and pimonidazole staining

Hypoxia is a state of low oxygen concentration in the tissue. Tumor cells proliferate quickly and require large amounts of oxygen. In tumors the supply of oxygen is also often limited by poor vascular architecture and low blood supply. As hypoxia induces angiogenesis, which leads to poorly constructed vasculature leading to poor oxygen supply, further fueling the process of angiogenesis, malignant tumors tends to be particularly prone to becoming hypoxic[20]. Hypoxic cells are often devided into two subgroups according to the cause of hypoxia[26]: Acute, or perfusion limited hypoxia, and chronic, or diffusion limited hypoxia. Acute hypoxia is caused by a temporary decrease in blood supply resulting from e.g. a temporary obstruction of the vessels. Chronic hypoxia is due to the diffusion limit of oxygen in tissue, making cells located at a distance close to the diffusion limit from the blood vessels hypoxic[20].

Pimonidazole hydrochloride is a molecular compound that forms covalent bonds with cellular macromolecules when the oxygen concentration is below 1.3%[30]. Thus, poorly oxygenated regions of tissue will accumulate pimonidazole, making it possible to visualize the hypoxic regions in a prostatectomy specimen. Administering pimonidazole to patients before surgically removing the prostate gland allows for immunostaining of sections of the gland to identify regions, and quantify, degrees of hypoxia in the tissue.

2.1.3 Clinical classification of prostate cancer

Prostate cancer is a cancer type with particularly heterogeneous biology[9]. Some tumors can remain indolent for many years, whilst others rapidly progresses to a life-threatening disease. Many different classifications, and prognostic factors exists to stratify patients into groups with different cancer aggressiveness(Gleason score and prostate specific antigen level), tumor extent(tumor- node- metastasis-classification) and risk or recurrence(D'Amico risk classification). In the following the classifications used in this study are introduced.

Prostate specific antigen

Prostate specific antigen(PSA) is a protein that is produced by the cells of the prostate. It is mainly released into the seminal fluid, and only small amounts are leaked in to the circulatory system in normal prostate[33]. In pathological prostate tissue, however, the amount of PSA leaked into the blood is increased, and elevated PSA levels in the blood is thus a sensitive marker for prostate cancer[33]. However, despite being an organ-specific marker, it is not a cancer-specific marker as several benign conditions can result in elevated PSA levels. Prostatitis and benign hyper prostatic hyperplasia (enlargement of the prostate) are both conditions that can result in higher PSA values in the blood [1]. Furthermore, prostate cancer can be present in men without elevated PSA values in the blood[1].

Gleason score

The Gleason scoring system is a cancer grading system that is unique for prostate cancer. It was developed by Donald Gleason in 1966, and is based solely on glandular architecture, and not structural abnormality of the cells. Five different patterns of glandular architecture with increasing abnormality are graded from one to five, and the Gleason score is compiled from the grade of the two most prevalent patterns in the biopsies or prostatectomy specimen[31].

The Gleason score is determined by the sum of the Gleason grades of the two most prevalent patterns in the biopsies, giving a pure grade 3 biopsy a Gleason score of $3 + 3 = 6$, a grade 3 biopsy with regions of grade 4 is a Gleason score of $3 + 4 = 7$a, and a grade 4 biopsy with regions of grade 3 is a Gleason score of $4 + 3 = 7$b. Gleason grade 1 is generally not reported, and Gleason grade 2 is rarely used in contemporary practice, and thus the Gleason scoring system categorizes cancers as Gleason scores 6, 7a, 7b, 8, and $9 - 10$[31]. Examples of Gleason graded biopsies are shown in figure 2.2.

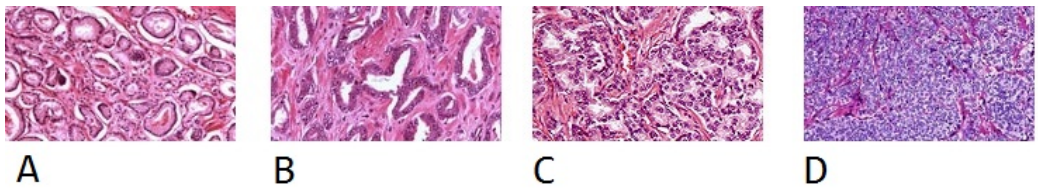

Figure 2.2: Examples of Gleason graded biopsies. The images are showing: A) a grade 2 biopsy, with fairly well differentiated glands with moderate spacing. B) a grade 3 biopsy, where the glands are starting to infiltrate eachother. They are of variable size, and with distinctly infiltrative margins. C) a grade 4 biopsy, consisting of complex and irregular glands. D) a grade 5 biopsy, with none, or only occasional gland formation. The images are taken from http://oncolex.no [28]

.

Tumor- node- metastasis-staging

The tumor- node- meatastasis(TNM) staging aims to describe the severity of a cancer based on the size and reach of the primary tumor, whether it has spread to the lymph nodes, and also whether the cancer has metastasized or not. Three different staging factors are reported:

- **T** - Size and reach of the primary tumor
- **N** - Spread to the lymphatic system
- **M** - Metastasis

The staging is typically performed prior to treatment, and is called the clinical stage(cT,cN,cM). Cancer can then be classified further after surgery or biopsies, when the extent of the cancer is better known. This classification is called the pathological stage(pT, pN, pM), and combines the results from the clinical staging with results from surgeries or biopsies. In this study, only the T-stage factor is reported, and it is determined according to the recomandations of the international society of urological pathology(ISUP) of 2010 [25]:

- **Tx:** Unable to evaluate.
- **T0:** No evidence of primary tumor.
- **T1:** Clinically in-apparent tumor neither palpable nor visible by imaging.
- **T2:** Tumor confined within prostate.
  - −T2a: Tumor involves one half of one lobe or less.
  - −T2b: Tumor involves more than one half of one lobe, but not both lobes
  - −T2c: Tumor involves both lobes.
- **T3:** Tumor extends through the prostate capsule.
  - −T3a: Extracapsular extension (unilateral or bilateral).
  - −T3b: Tumor invades seminal vesicle(s).
- **T4:** Tumor is fixed or invades adjacent structures other than seminal vesicles.

D'Amico risk classification

The D'Amico risk classification is a combined modality staging system that aims to stratify patients into groups as either low, intermediate or high risk of biochemical recurrence after radiotherapy or surgery. The prediction model is based on the PSA levels, clinical TNM-stage, and biopsy Gleason score[22]. The definitions of the groups as originally described by D'Amico[15], are:

- **Low-risk:** cT1 or T2a, PSA$\leq 10 ng/ml$ and Gleason score ≤ 6.

- **Intermediate-risk:** cT2b, PSA between $10ng/ml$ and $20ng/ml$ and a Gleason score = 7.

- **High-risk:** T2c, PSA$\geq$ 8, and Gleason score $\geq$ 8.

2.2 The basic physics of magnetic resonance imaging

The hydrogen nuclei(protons) in the human body are positively charged spin-$\frac{1}{2}$ particles, thus they carry a magnetic moment. In the natural state these magnetic moments are completely incoherent, and the net magnetization of the body is zero. In MRI the body is placed in an external magnetic field $\vec{B}_0$ which results in a net magnetization of the body $\vec{M}_0$ parallel to $\vec{B}_0$. A RF-pulse is then used to excite the nuclei by *flipping* their magnetic moments down in the plane normal to $\vec{B}_0$, and since the protons precess with the larmor frequency about the B_0-axis[19], this will induce a current in the MR-scanner receiver coils giving rise to the signal used to reconstruct the MR-image. This signal will decay with the nuclei relaxation through two processes:

- **Spin-lattice relaxation** The process by which the magnetization along $\vec{B}_0$ is regained, returning to thermodynamic equilibrium with its surroundings (the lattice). Characterized by the time-constant $T1$

- **spin-spin relaxation** The process by which the signal is gradually lost because of the proton spins phase dispersion after the RF-pulse, due to local inhomogeneities in the B-field arising from the magnetic moment of neighbouring spins. Characterized by the time-constant $T2$.

In clinical MRI a series of RF-pulses are applied consecutively, in combination with different constellations of magnetic gradient fields in order to manipulate the image contrast by suppressing, or enhancing, the different relaxation processes effect on the signal. Several different such pulse-sequences exists, but it suffices in this brief introduction to mention that the net steady state

transverse magnetization arising from the sequence used in this investigation, the gradient echo sequence, behaves according to[6]:

$$M_t = M_0 \frac{\sin\alpha(1 - e^{-\frac{TR}{T1}})}{1 - \cos\alpha(1 - e^{-\frac{TR}{T1}})} e^{-\frac{TE}{T2}} \tag{2.1}$$

where α is angle by which the magnetic moment is flipped(the amount of excitation, determined by the amplitude and duration of the RF-pulse), TR is the time between consecutive excitation pulses (repetition time) and TE is the time between the RF-pulse and the signal echo (echo time).
Several books have been written on the subject, and for a more comprehensive and exhaustive explanation, the interested reader is referred to [38] or [6].

2.3 Contrast agent effects on signal intensity

2.3.1 Contrast agent relaxivity

The effect on signal intensity by the presence of CA is given by the CAs (CA) ability to alter the $T1$ and/or $T2$ relaxation times of the protons in the vicinity of the CA. The ability of the CA to enhance the proton relaxation rate ($R_{1,2} = \frac{1}{T_{1,2}}$) is, according to the Solomon and Bloomberg equation, defined in terms of its relaxivity [6]:

$$R_{1,2} = \frac{1}{T_{1,2}} = R^0_{1,2} + r_{1,2}C \tag{2.2}$$

Where $R^0_{1,2}$ are the $T1$ and $T2$ relaxation rates without the presence of CA, C is the molar concentration of CA, and $r_{1,2}$ are the relaxivity constants ($\frac{1}{T1}, \frac{1}{T2}$) of the CA, and are dependent on the type of CA, and the tissue.

Note, however, that even though the enhancement of the relaxation rates of the protons have a linear relationship with the concentration of CA, the signal response in MRI is in general not linear with CA concentration. Looking at the signal response in a contrast enhanced gradient echo image, inserting

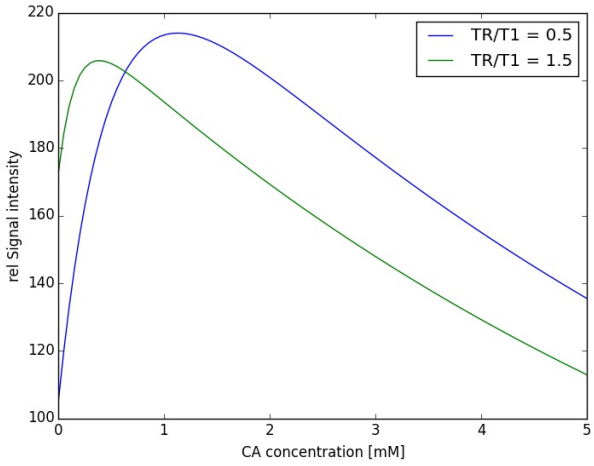

Figure 2.3: Simulated dose response of a contrast enhanced MR-image

equation (2.2) into equation (2.1), the following equation for the signal intensity is obtained:

$$SI(C) = k\rho \frac{\sin\alpha(1 - e^{-TR(1/T1+r_1C)})}{1 - \cos\alpha(1 - e^{-TR(1//T1+r_1C)})} e^{-TE(\frac{1}{T2}+r_2C)} \tag{2.3}$$

When plotting this signal intensity (fig. 2.3) we can see that it is highly non-linear. When the concentration is high, the $T1$ time is short enough to allow full recovery of longitudinal magnetization within each TR. At this point increasing the concentration does not result in any increased signal, and the image is *saturated*. However, in the initial, low concentration range we observe a fairly linear increase in SI with increased concentration. Furthermore, the linear range is dependent on $\frac{TR}{T1}$, and should thus be able to be manipulated by correct scanner tuning. In the following this possibility will be assessed.

2.3.2 Signal intensity in a contrast enhanced spoiled gradient echo image

The total transverse magnetization produced by the bulk of proton spins in a steady state gradient-echo MRI sequence is given by:

$$M_T = M_0 \frac{\sin\alpha(1 - e^{-\frac{TR}{T1}})}{1 - \cos\alpha(1 - e^{-\frac{TR}{T1}})} e^{-\frac{TE}{T2}}$$

where α is the flip-angle, TE and TR is the echo time and the repetition time respectively. The tissue-specific parameters are $T1$; the spin-lattice relaxation time, and $T2$; the spin-spin relaxation time.

The MR signal is proportional to the net magnetization, giving the signal intensity as:

$$SI(T1, T2) = k\rho \frac{\sin\alpha(1 - e^{-\frac{TR}{T1}})}{1 - \cos\alpha(1 - e^{-\frac{TR}{T1}})} e^{-\frac{TE}{T2}}$$

Here k is a scanner-specific constant, and ρ is the proton density.

Assuming perfect spoiling of the transverse magnetization (i.e. $TR >> T2$)makes the signal independent of $T2$. Further, when $TR << T1$ the approximation $e^{-\frac{TR}{T1}} \approx 1 - \frac{TR}{T1}$ can be made.

In this case the signal in a spoiled gradient-echo sequence is purely T1-weighted, and given by:

$$SI = k\rho \frac{\sin\alpha\frac{TR}{T1}}{1 - \cos\alpha\frac{TR}{T1}} \tag{2.4}$$

If the flip angle α is large, the term $\frac{TR}{T1}\cos\alpha \approx 0$, making the signal intensity proportional to $\frac{TR}{T1}$:

$$SI = k\rho \sin(\alpha)\frac{TR}{T1}$$

Applying equation 2.2 to find the signal response as a function of CA concentration C the following expression for the signal intensity is obtained:

$$SI(C) = k\rho \sin(\alpha)TR(\frac{1}{T1} + r_1C) = SI_0(1 + TRr_1C)$$

$$\frac{SI(C) - SI_0}{SI_0} = RSI = TRr_1C \tag{2.5}$$

where SI_0 is the signal intensity without the presence of CA, and RSI is the relative signal increase. Under the aforementioned assumptions the relative signal increase is in other words directly proportional to CA concentration.

Note however, that at very high concentrations of CA the assumption $TR << T1$ may no longer be valid, as the CAs effect on the tissue is to decrease the $T1$-value. Making $\frac{TR}{T1}$ big decreases the linear range as illustrated in figure 2.3.

2.4 Pharmacokinetic modelling

By taking several images before, during and after the injection of CA, the blood perfusion and CA exchange can be mapped over time in each voxel. The temporal kinetics of the signal enhancement is dependent on the local circulatory system, and can be analyzed using different strategies to obtain descriptive, or semi-quantitative criteria, or even microvascular physiological parameters [13].

Although the differentiation is somewhat arbitrary, a separation between two different kinds of concentration time-curve analysis is usually made: semi-

quantitative analysis, where certain parameters are obtained directly from the RSI time-curve, such as the time-to-peak, area under the time-curve (AUC) or the slope of the washout curve. The other kind of analysis is one which aims to describe the distribution of the CA by a mathematical model of the perfusion and/or permeability and the volume fraction of different kinds of tissue in the voxel. Then, by fitting the time-curve data to said model, quantitative parameters describing the underlying physiology may be obtained.

2.4.1 Semi-quantitative analysis

The uptake of CA may be assessed by the relative signal increase, or by parameters that may be directly read from the RSI time-curve. Such parameters include the area under the curve (AUC) and the initial area under the curve (iAUC), which reflects the total uptake of CA in the voxel, and the uptake in the early stages after the infusion. The time-to-peak(TTP), which is the time it takes for the signal to reach its maximum, reflecting the wash-in rate of CA in the voxel. And the slope of the washout curve which reflects the rate at which signal-enhancement is lost from the voxel. These semi-quantitative measures are illustrated in a typical RSI time-curve in figure 2.4.

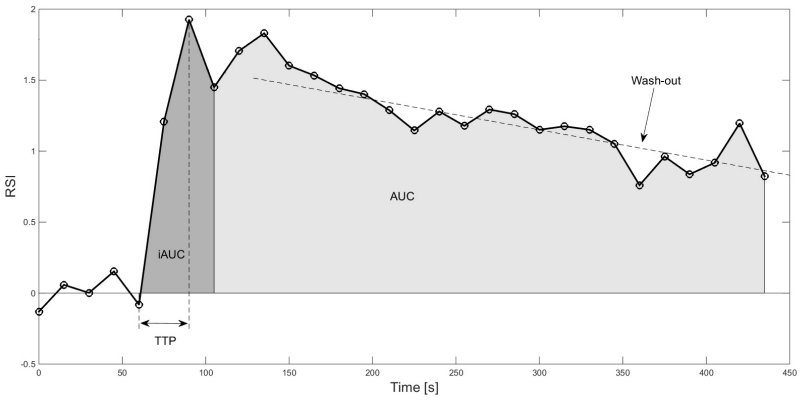

Figure 2.4: Schematic figure showing a typical signal time-curve and the semi-quantitative parameters. At time $t = 60s$ the CA arrives in the region.

Several investigators have found correlations between different semi-quantitative parameters and various physiological properties in prostate cancer [12][11], and others yet have used them successfully to monitor cancer growth and treatment response[42]. Although these methods are fairly straightforward to implement, they have certain obvious limitations. The parameters obtained does not necessarily have any clear relation to any singular physical trait, and may reflect several physiological features at once. In a study by Walker-Samuel *et al.* the iAUC was found to display correlations with tissue blood-flow, vascular permeability-surface-area product, tissue density, and the extra-vascular extra-cellular volume fraction in the tissue of interest [37]. The degree to which these different physiological parameters contributes to the iAUC is difficult to determine, and is at least partially influenced by the somewhat arbitrary time-point set to define the end of the initial uptake of CA. In addition, it is inherently difficult to quantitatively compare results from different scan preformed at different times, and results from semi-quantitative analysis are difficult to compare between different studies and institutions, since these methods rely on analysis of the signal intensity which is a measure without physical units that is influenced by technical image acquisition parameters[5].

2.4.2 Quantitative analysis

In order to obtain parameters that relate more directly to the underlying physiology a more rigorous method of data analysis is required. The goal is to find a model that describes the distribution of CA by the physiological processes such as blood flow/perfusion, vessel wall permeability, cell density etc. The principal assumption, when performing such pharmacokinetic modelling is that the body may be decomposed into several interacting subsystems called *compartments*. Such compartments may be considered as units of volume that the CA appears to occupy, into and out of which the CA dynamically flows.

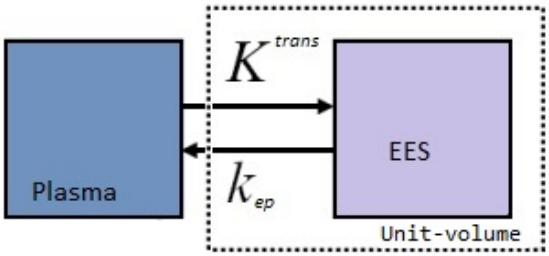

Figure 2.5: Single compartment model. The blood capillaries are treated as a reservoir from which CA is infused into the EES with a rate K^{trans}, and eliminated with a rate k_{ep}.

The CA is administered through an intravenous injection, and reaches the tissue of interest from the blood vessels. In the case of Gd-DTPA, the CA used in these experiments, its molecules are small enough to leak through the capillary wall and into the tissue, but too big to enter the cells and is therefore confined to the extra-vascular extra-cellular space (EES). The simplest pharmacokinetic model depicts each voxel in the MR-image as a single compartment, of which the CA occupies the fraction that is the EES. Into, and out of this compartment the CA flows with a rate-constant $K^{trans}[min^{-1}]$, that is assumed to be the same in both directions. However since the CA only can can occupy the fraction of the voxel-space that is the EES, the back-flux to the blood plasma is given by the rate constant k_{ep}, defined by $K^{trans} = \nu_e k_{ep}$, where ν_e is the (dimensionless) EES-fraction of the total volume. If the voxel-volume contains zero cells, ν_e will be equal to 1. This simple model is illustrated in figure 2.5

Assuming no destruction or accumulation of CA within the EES the concentration of CA in the voxel may then be expressed by the following equation[35]:

$$\frac{dC_t}{dt} = K^{trans}C_p - K^{trans}C_e = K^{trans}C_p - k_{ep}C_t \tag{2.6}$$

Where C_p is the concentration in the plasma, C_e is the concentration in the EES, and C_t is the concentration in the unit volume(the voxel-volume). In the last relation in eq. (2.6) the identity $K^{trans}C_e = K^{trans}\nu_e C_t = k_{ep}C_t$ has been used.
Eq. (2.6) can be solved using Laplace-transforms, using the fact that $\mathcal{L}[\frac{dC}{dt}] = s\mathcal{L}[C] - C(0)$, and the linearity properties of the Laplace-transform[7], the differential equation can be transformed to an algebraic equation, assuming the concentration of CA in the unit volume at time $t = 0$ is zero, i.e. $C_t(0) = 0$:

$$\mathcal{L}[\frac{dC_t}{dt}] = s\mathcal{L}[C_t] = K^{trans}\mathcal{L}[C_p] - k_{ep}\mathcal{L}[C_t]$$

Renaming $\mathcal{L}[C(t)] = \tilde{C(s)}$ we obtain:

$$\tilde{C}_t(s) = \frac{K^{trans}}{s + k_{ep}}\tilde{C}_p(s)$$

This expression can be transformed back to the time-domain by an inverse Laplace-transform, using the fact that $\mathcal{L}\big[\frac{1}{s+\alpha}\big] = e^{-\alpha t}$ [7], giving:

$$C_t(t) = K^{trans}e^{-k_{ep}t} * C_p(t) \tag{2.7}$$

Where $*$ denotes the convolution operation:

$$K^{trans}e^{-k_{ep}t} * C_p(t) = K^{trans}\int_0^t C_p(\tau)e^{-k_{ep}(t-\tau)}d\tau$$

Thus, the concentration in the unit-volume of tissue may be regarded as a response-function of the concentration in the blood-plasma.

2.4.3 The Brix-model

In the simple one-compartment model described above (eq. (2.7)) knowledge of the concentration in the blood-plasma at all times during the imaging is required. The concentration of CA in the plasma as a function of time is called the Arterial Input Function(AIF), and may either be measured by sampling blood during the imaging, or estimated from images containing a large vessel or artery. The estimation of the AIF from arteries in an image is however troublesome, as concentrations in the arteries may be high enough to fully saturate the image making accurate estimation of the concentration difficult. The need for an accurate AIF may be avoided by extending the model to include a second compartment that models the concentration in the plasma as a response to a known infusion-rate of CA.

In the studies by Brix *et al.* a two-compartment model was proposed [10]. A plasma compartment was included, modelling the CA transport in the plasma compartment and its exchange with the EES. The model is illustrated in figure 2.6. This model uses a linear one-compartment open model to describe the CA in plasma, and incorporates the EES of the lesion as a peripheral compartment which is connected to the central plasma-compartment by linear exchange processes in both directions.

The CA-kinetics may then be expressed by the following set of differential equations:

$$\frac{dM_p}{dt} = K_{in} - (k_{12} + k_{el})M_p + k_{21}M_e \tag{2.8}$$

$$\frac{dM_e}{dt} = k_{12}M_p - k_{21}M_e \tag{2.9}$$

Where M_p and M_e are the amounts of CA in the plasma and the EES, respectively. k_{12} and k_{21} are the rate constants $[time^{-1}]$ for transfer of CA between the compartments, k_{el} is the elimination rate from the plasma-compartment,

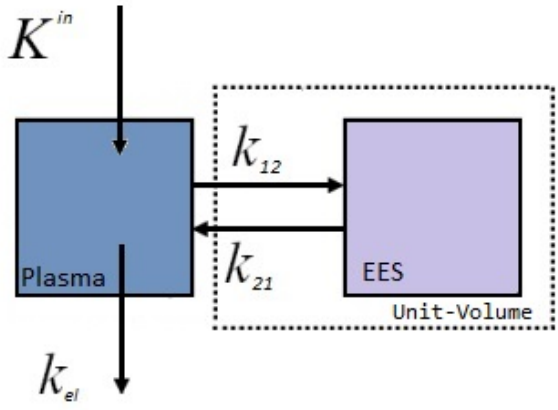

Figure 2.6: Open two-compartment model. The tissue(unit volume) contains a plasma-compartment with constant rate infusion, and a peripheral EES-compartment. Elimination occurs only from the central plasma-compartment.

and K_{in} is the CA infusion rate $[mass/time]$. The concentration is related to the total amount by $C_i = \frac{M_i}{V_i}$ where V_i is the volume of compartment i. Assuming $V_p >> V_e$, i.e. the volume of the plasma compartment is much larger than the volume of EES, the transport of CA between the EES and the plasma will result in a negligible change the concentration in the plasma, and the terms $k_{12}M_p$ and $k_{21}M_e$ may be neglected in eq (2.8). This yields the following set of differential equations describing the kinetics of the CA:

$$\frac{dC_p}{dt} = \frac{K_{in}}{V_p} - k_{el}C_p \tag{2.10}$$

$$\frac{dC_e}{dt} = \frac{V_p}{V_e}k_{12}C_p - k_{21}C_e \tag{2.11}$$

In the one-compartment model described earlier (eq.(2.6)) the assumption was made that the transfer velocities between the plasma and the EES were equal in both directions. By assuming no accumulation or different forms of binding of the CA in the two compartments the same assumption can be made again, giving $k_{12}V_p = k_{21}V_e$, or, equivalently $\frac{V_p}{V_e}k_{12} = k_{21}$. Acknowl-

edging that k_{21} is the same as k_{ep} described in the one-compartment model, and using the fact that the total concentration in the unit tissue-volume is $C_t = \nu_e C_e$ equation (2.11) may be written as:

$$\frac{dC_t}{dt} = \nu_e k_{ep} C_p - k_{ep} C_t \tag{2.12}$$

In the study by Brix *et al.* the intravenous infusion of CA was given at a constant rate for a period of time τ. With initial conditions $C_p(0) = 0$ and $C_t(0) = 0$ the decoupled system of differential equations (2.10 and 2.12) has a solution for $t > \tau$ [10]:

$$C_p(t) = \frac{K_{in}}{V_p k_{el}}(e^{k_{el}\tau} - 1)e^{-k_{el}t} \tag{2.13}$$

$$C_t(t) = \frac{K_{in}}{V_p}\nu_e \frac{k_{ep}}{k_{ep} - k_{el}}\Big(\frac{e^{k_{el}\tau} - 1}{k_{el}}e^{-k_{el}t} - \frac{e^{k_{ep}\tau} - 1}{k_{ep}}e^{-k_{ep}t}\Big) \tag{2.14}$$

In this investigation the CA was given as a rapid bolus, so equations 2.13 and 2.14 need to be altered to fit this somewhat different situation. By letting τ tend to zero, a solution that fits this case is obtained. As $\tau \to 0$, $e^{k\tau} \approx k\tau + 1$ giving the final solution to the concentration in the unit tissue-volume as:

$$\begin{aligned} C_t(t) &= \frac{K_{in}\nu_e}{V_p}\frac{k_{ep}}{k_{ep} - k_{el}}\Big(\frac{k_{el}\tau}{k_{el}}e^{-k_{el}t} - \frac{k_{ep}\tau}{k_{ep}}e^{-k_{ep}t}\Big) \\ &= \frac{K_{in}}{V_p}\nu_e \tau k_{ep}\frac{e^{-k_{el}t} - e^{-k_{ep}t}}{k_{ep} - k_{el}} \end{aligned} \tag{2.15}$$

This expression(2.15) can now be inserted into eq (2.5) to obtain the signal response in a dynamic contrast-enhanced T1-weighted spoiled gradient echo image as a function of the physiological parameters k_{ep} and k_{el}:

$$\frac{SI(t) - SI_0}{SI_0} = Ak_{ep}\frac{e^{-k_{ep}t} - e^{-k_{el}t}}{k_{el} - k_{ep}} \tag{2.16}$$

Here A is a function, referred to as the amplitude, depending on the MR-scanner parameters (TR,TE,α,B_0), tissue-specific parameters ($T1_0$,V_p,ν_e) and the type of CA, and its infusion rate (r_1,$K_{in}\tau$). Thus, in the approximations discussed, the shape of the temporal response-curve $\frac{SI-SI_0}{SI_0}$ is determined, apart from multiplication by the multidimensional amplitude A, by the transfer rate k_{ep} between the plasma-compartment and the EES, and the elimination rate k_{el} from the plasma compartment.

3. Methods and Materials

3.1 Patients

Between October 2011 and July 2012, 110 patients with biopsy- confirmed prostate cancer who had been stratified for surgical treatment were recruited to the ongoing study *FuncProst* at Oslo University Hospital, *Radiumhospitalet*. Only patients with intermediate- or high-risk cancer, according to D'Amico risk classification were included. In all participating patients, the aggressiveness and extent of the cancer had been determined by routine digital rectal examination(DRE), and trans rectal ultra Sound(TRUS) preformed at referral hospitals. Biopsies were preformed to determine the Gleason score. The clinical data, including T-stage, obtained from DRE and TRUS, together with Gleason score and histopathological T-stage deduced from the biopsies are summarized in table 3.2 on page 28.

The study was approved by the regional committees for medical and health research ethics(REK), and the patients provided written informed concent.

3.1.1 MRI

The participants underwent preoperative, multiparametric MRI using a $1.5T$ Discovery MR450 MR scanner(GE Medical Systems, Erlangen, Germany). The MRI protocol consisted of morphologic images(T1 weighted(T1W) and T2-weighted(T2W)), and functional images(diffusion-weighted(DW) MRI and dynamic contrast-enhanced(DCE) MRI). The details of the MR protocol are listed in table 3.1 on page 25. For the functional images, the gadolinium-

based CA Gd-DTPA was administered intravenously during the imaging. All images, and associated meta-data, were transferred to the institutional picture and archiving system(PACS), and exported as .DICOM-files to separate patient-folders for analysis.

3.1.2 Pimonidazole administration

The hypoxia marker pimonidazole hydrochloride(Hypoxyprobe Inc., Burlington, MA, USA) was given to the patients 12-24 hours prior to surgery, to identify regions- and quantify the degree of hypoxia post surgury. The patient group was devided into two subgroups, one consisting of 53 patients who were given pimonidazole intravenously, and one consisting of the remaining 56 patients who were given the hypoxia marker orally, as a pill. The patients received $500mg$ pimonidazole per m^2 body surface, with a upper limit of $1000mg$ per patient.

Acquisition parameters	T2W FSE	ADC	DWI	T2W CUBE	T1W CUBE	DCE	T1W post Gd
Pulse sequence	2D SE	SE-EPI	SE-EPI	3D-SE	3D-SE	3D spoiled GE-Dixon	3D spoiled GE-Dixon
Acquisition plane	sagittal/transversal/coronal	transversal	transversal	transversal	coronal	transversal	transversal
Echo time [ms]	99	59	64	89	8.0	3.1	3.6
Repetition time [ms]	3376/2954/2954	3000	6000	1200	400	5.8	7.9
Flip angle	90	90	90	variable	variable	15	15
Slice thickness Acquired Interpolated	3	4	4	1 1	2	2.6	2.0
Slice gap	1	1	1	0	0	0	0
Number of excitations	6	2	16	2	1	1	1
Inplane resolution [mmxmm] Acquired Interpolated	 0.56x0.56 0.35x0.35	 1.96X1.96 0.70x0.70	 1.96x1.96 0.70x0.70	 1.00x1.00 0.63x0.63	 1.20x1.20 0.90x0.90	 1.50x1.50 0.94x0.94	 1.00x1.00 0.86x0.86
Echo train	28	92	92	90	30		1
Bandwidth [Hz/pixel]	325	1953	1953	488	488		325
FOV [mmxmm]	180x180	180x180	180x180	320x320	460x460	240x240	440x440
Matrix size Acqired Interpolated	 320x320 512x512	 92x92 256x256	 92x92 256x256	 320x320 512x512	 384x384 512x512	 160x160 256x256	 440x440 512x512
Parallel imaging factor	2	1	1	2.5x2	2x2	2	3x2
Motion correction	PROPELLER	no	no	no	no	yes*	no
b-values $[s/mm^2]$	NA	0-100-200-300-400-500-600-700-800-900-1000	1500	NA	NA	NA	NA
Time resolution [sec]	NA	NA	NA	NA	NA	11.4	NA
Acquisition time	4:37/4:02/4:02	4:09	6:30	7:33	2:56	5:43	1:13

Table 3.1: MR-protocol. ADC; Apparent Diffusion Coefficient, DCE; dynamic contrast-enhanced, DWI; Diffusion-Weighted Imaging; EPI; echo planar imaging, FSE; Fast Spin Echo, FOV; field of view, MR; Magnetic Resonance, T2W; T2 weighted, PROPELLER; Periodically Rotated Overlapping ParallEL Lines with Enhanced Reconstruction, SE; spin echo, , GE; gradient echo.
∗performed using nICE (Nordic Neurolab, Bergen, Norway)

3.1.3 Radical prostatectomy

A radical prostatectomy, a full surgical removal of the prostate gland, was preformed by a three-armed DaVinci system(Intuitive Surgical, Sunnyvale, CA, USA). The gland was immediately transported from the operating room to the pathology department for tissue biobanking. The localization and extent of index tumor was predicted from the MR-images. By a combination of low signal intensity in the T1W and T2W images, high signal intensity in the heavily DW images, rapid wash-in and wash-out in the DCE images, and by low apparent diffusion coefficient, the index tumor could be identified(see figure 3.1).

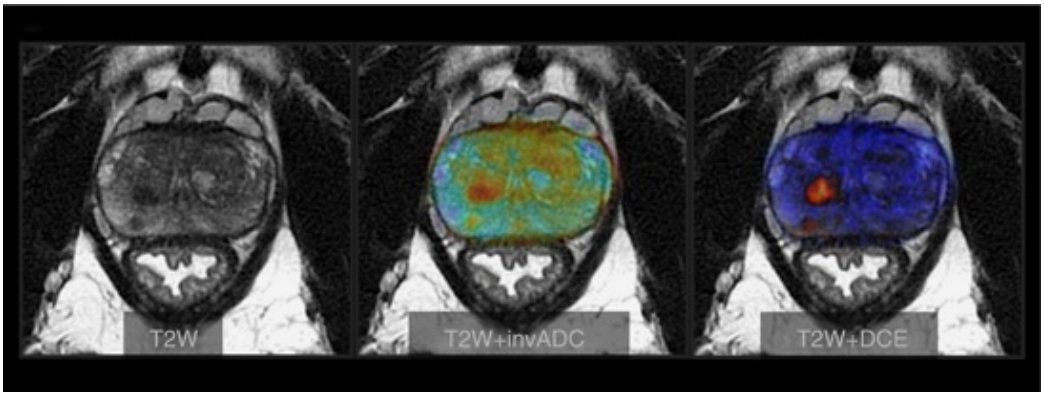

Figure 3.1: Multiparametric MR-images used to identify index tumor. The picture is taken from a paper by Ragnum *et al.*[30] produced from the FuncProst study.

3.1.4 Histopathology

Based on the MR images two punch hole biopsies were taken from the tumor, and the prostatectomy specimens were sliced and fixed according to standard procedures described by Ragnum *et al.*[30]. Sections of the prostate gland were stained with Hematoxylin and eosin stain(HE-stain) to indicate cellular architecture. The punch hole biopsies, and prostatectomy specimen slices underwent histopathological assessment, and were TNM classified, and graded according to the Gleason-grading system.

Immunohistochemistry was performed on slices containing index tumor, using standardized protocols. Hypoxic regions in the histological sections were visualized by the staining of monoclonal mouse antibodies for pimonidazole, and the staining patterns of malignant glands were evaluated blindly to other immunuhistochemistry data[30]. Fractions of moderate to strong cytoplasmic staining, and nuclear staining were determined independently by two study pathologists, and given immunoscores from 0 to 5 where $0 = 0\%$, $1 = 1-10\%$, $2 = 11-50\%$, $3 = 51-90\%$, $4 = 91-100\%$, $5 = 100\%$. Total pimonidazole score is reported as the average of the cytoplasmic staining score, and the nucleus staining score. The pimonidazole scores, Gleason scores from prostatectomy specimens, and histopatological T-stages of the patient group are summarized in table 3.2 of page 28. In the table the patients are devided into two cohorts based on whether they recieved pimonidazole intravenously or orally. The p-value listed in the table is the significance of the difference between the cohorts as determined by a two sided student t-test. Pictures of an example HE-section and a pimonidazole immunostained section are shown in figure 3.2

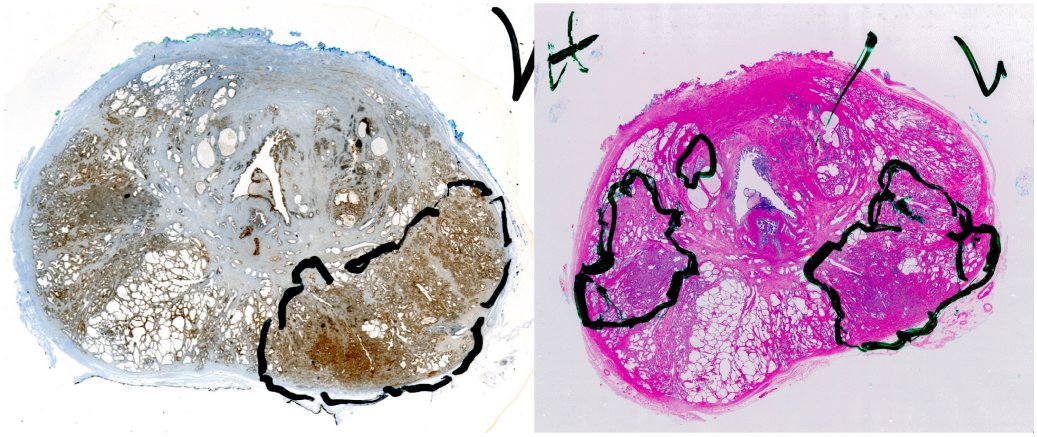

Figure 3.2: Left: Pimonidazole immunostained section of the prostate gland. The brown areas are regions of high concentration of pimonidazole, indicating low oxygen concentration. Right: HE section with cancer foci (black circles).

Patient and tumor characteristics	IV cohort	Pill cohort	p-value	Total
Age(years)				
Mean ± SD	64.7 ± 6.0	62.7 ± 7.3	0.14	63.7 ± 6.7
Range	$49 - 75$	$45 - 76$		$45 - 76$
Largest tumor extent				
Mean ± SD	484.0 ± 419.4	303.4 ± 213.5	0.37	400.0 ± 348.7
Range	$24 - 2000$	$40 - 900$		$24 - 2000$
PSA(ng/ml)				
Mean ± SD	13.1 ± 0.4	12.2 ± 20.9	0.76	12.7 ± 16.0
Range	$2.0 - 42.0$	$2.2 - 145.0$		$2 - 145$
≤ 10	26(49.0%)	39(76.5%)		65(62.5%)
> 100 and ≤ 20	21(39.6%)	8(15.7%)		29(27.8%)
> 20	6(11.3%)	4(7.8%)		10(9.6%)
Gleason score from core biopsies			0.16	
$5 - 6$	2(3.8%)	6(12.0%)		8(7.8%)
7a$(3 + 4)$	21(39.6%)	22(44.0%)		43(41.7%)
7b$(4 + 3)$	14(26.4%)	7(14.0%		21(20.4%)
$8 - 10$	16(30.2%)	15(30.0%)		31(30.1%)
Gleason score from prostatectomy specimen			0.03	
$5 - 6$	2(3.8%)	6(12.0%)		8(7.8%)
7a$(3 + 4)$	19(35.8%)	25(50.0%)		44(42.7%)
7b$(4 + 3)$	15(28.3%)	12(24.0%)		27(26.2%)
$8 - 10$	17(32.1%)	7(14.0%)		24(23.3%)
Clinical T-stage			0.55	
T1c	22(43.1%)	23(51.1%)		45(46.8%)
T2a/T2b/T2c	19(37.3%)	21(46.7%)		40(41.7%)
T3	10(19.6%)	1(2.2%)		11(11.5%)
Histopatological T-stage			0.51	
T2	16(30.2%)	21(42.0%)		37(35.9%)
T3a/T3b	37(69.8%)	29(58.0%)		48(64.1%)
T4	0(0.0%)	0(0.0%)		0(0%)
D'Amico risk classification			0.04	
Low risk	0(0.0%)	3(6.0%)		3(2.9%)
Intermediate risk	24(45.3%)	28(56.0%)		52(50.5%)
High risk	29(54.7%)	19(38.0%)		48(46.6%)
Pimonidazole score			0.00	
≤ 1.5	11(25.6%)	26(55.3%)		37(41.1%)
> 1.5 and < 3.5	23(53.3%)	19(40.4%)		42(46.7%)
≥ 3.5	9(20.9%)	2(4.3%)		11(12.2%)

Table 3.2: Sumarization of the patient and tumor characteristics

3.2 Pharmacokintic modelling

All images were analyzed using Matlab. The images were extracted from the DICOM-files using the built in dicomread-function from the Image Processing Toolbox. The images were then sorted to obtain a complete time-series for the slice in which the tumor region of interest(ROI) was drawn by the radiologist. The time of arrival of CA was different in each patient, due to the difference in time taken to prepare and administer the injection of CA. Since the model used(eq. (2.16)) assumes CA-arrival at $t = 0$, a routine for

identifying the actual time of arrival of CA was made in order to be able to compare the pharmocokinetic parameters across the patient-population. This routine compared the relative changes in mean signal intensity between each consecutive image to a set threshold. If the difference between image i and $i+1$ was greater than the threshold, image i was set as image 0, and the time $t[i]$ was set as $t = 0$. Initially the threshold value was set to two times the standard deviation of the difference between the two first pre-contrast images, but due to large variations in the noise range between patients, a global patient-independent value was used instead. The threshold level was set by manually examining the arrival of CA in the iliac veins visible in the image (see figure 3.3), and comparing it to the relative increase in the mean signal intensity in the image for the first ten patients. The threshold value was then controlled by comparing the arrival of CA by manual inspection, to the arrival-time determined by the numerical routine for patients 11 to 50.

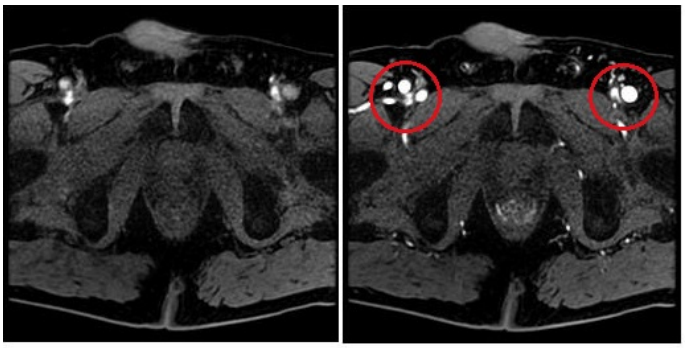

Figure 3.3: The difference in mean signal intensity between image i(left) and image $i+1$(right) is greater than the threshold, thus image i is set as image 0, and the time $t[i]$ was set as $t = 0$. The iliac veins used for manual control of the arrival-time of CA are shown by the red markers.

Once the arrival time of CA was defined, the relative signal increase, $RSI = \frac{SI - SI_0}{SI_0}$, was determined for each pixel, by letting the mean pixel intensity of the pre-contrast images define the relative signal at time $t = 0$:

$$SI_{0,i,j} = \frac{1}{N-1} \sum_{n=1}^{N-1} SI_{i,j}(n)$$

Where $SI_{i,j}(n)$ is the signal intensity of pixel (i, j) in the n'th time-frame, and $N - 1$ is the number of pre-contrast time-frames. The RSI time-curves for each patient could then be interpolated over a standard time-vector which is the same for all patients by letting the patient-specific value N define the time $t = 0$:

$$RSI_{i,j}(k) = \frac{SI_{i,j}(k + N) - SI_{0,i,j}}{SI_{0,i,j}}$$

Where k denotes the entry in the standardized time-vector, and $k + N$ is the corresponding entry in the patient-specific time-vector where the offset in time is not accounted for. N is, as above, the frame-number in which the CA appears in the region.

Once the RSI has been interpolated over the standard time-vector, the semi-quantitative parameters can be extracted and compared between patients. The AUC and iAUC was determined by numerical integration using the trapezoidal method, defining the first 45 seconds as the initial uptake phase. The trapezoidal method is defined, in terms of the RSI as:

$$\int_a^b RSI(t)dt \approx \frac{1}{2} \sum_{k=1}^{K-1} (t_{k+1} - t_k)[RSI_k + RSI_{k+1}]$$

Where K is the entry in the time-vector corresponding to the time $t = b$. Thus, for the iAUC, with the first 45 seconds as the initial uptake phase $b = 45$, $K = 3$. The AUC was calculated using $K = 30 - max(N)$, the number of frames after the arrival of CA in the patient with the latest arrival.

The time to peak was found by reading out the time at which the RSI was at its maximum, and the washout gradient was found by a simple linear regression fit to the RSI from three minutes and until the end of the imaging sequence. The estimated semi-quantitative parameters were estimated pixel by pixel and stored in corresponding parameter images.

In addition to the semi-quantitative parameters, the parameters A,k_{ep} and k_{el} from the Brix-model (equation 2.16) were estimated pixel by pixel by

minimizing the sum Q of the square deviation between the measured signal intensities $RSI_{i,j,k}$ and the fitted model-value $F(RSI_{i,j,k}, t[k])$, $F(RSI, t)$ being the function defined by equation (2.16):

$$Q = \sum_{k=1}^{30-N} (F(RSI_{i,j,k}, t[k]) - RSI_{i,j,k})^2$$

Where $30 - N$ is the number of 15 second time steps in the interpolated RSI-vector, and $t[k]$ is the k'th entry in the standardized time-vector. The computation was done iteratively with the 'trust-region-reflective' algorithm from Matlabs optimization toolbox, setting a lower bound on all parameters to zero, as only positive values would represent a physically acceptable parameter. Again the estimated parameters were stored in parameter images for further statistical analysis.

To limit the computation time, the parameters were estimated only for pixels within the ROI surrounding the tumor. The ROI had been drawn by the radiologists, and was available as a set of coordinates defining the vertices of the polygon that is the ROI.

In addition to calculating the Brix-model parameters within the ROI surrounding the tumor for all patients, the same parameters were calculated for the entire prostate gland for the first 50 patients. This was done in order to examine whether there was any statistical difference in the parameters between the defined tumor and the rest of the prostate. The prostate gland was delineated crudely, with approximately five pixels between the delineation and the assumed edge of the prostate. This was done to ensure that only prostate gland-tissue, and not surrounding muscle-tissue was included in the region delineated.

3.3 Statistical analysis

Once the Brix model had been fitted, its reliability was examined by assessing the *goodness of fit*, and by examining the distributions of the residuals. The residuals are defined as the difference between the measured values and the values predicted by the model:

$$res = y_i - \hat{y}_i \tag{3.1}$$

and if the model is correctly specified, they should behave according to certain criteria: If the model provides a complete explanation of the response, then the residuals should arise from random error or noise, and should thus behave as a sample from a normal distribution with mean zero. In addition, there should be no dependence of the response variable on the residuals, or in other words, the variance of the residuals should be constant(homoscedastic). The residual distribution and the homoscedasticity was examined for the entire patient-population, to check the models ability to account for the variation in the measured data.

The measure used to compare the goodness of fit between patients, and between single voxels, was the residual standard error:

$$s_{res} = \sqrt{\frac{\sum_{i=1}^{n}(y_i - \hat{y}_i)^2}{n-p}} \tag{3.2}$$

Where n is the number of data-points, and p is the number of predictors. s_{res} is an estimator of σ_ϵ, the standard deviation of the errors. It has the advantage of having the same natural units as the response variable, making it easily interpretable as the the average distance that the data-points falls from the regression line. The s_{res} was used as a mean to identify pixels where the least squares algorithm had failed to supply the best fit of the data. For a fit to be deemed reasonable the demand was made that $s_res \leq 0.4$

The Pearson product moment correlation test was used to search for lin-

ear correlation between the clinical prognostic factors and the calculated DCE-MRI-parameters. The median values, as well as percentile values of the pharmacokinetic parameters were correlated to the clinical data, and the Pearson correlation coefficient and corresponding p-value was calculated. In addition, the Spearman rank correlation-coefficient was calculated to search for nonlinear correlation. All correlation analysis was done using the built-in functions from matlabs statistics and machine learning toolbox.

A two sided student t-test was used to check for any statistical difference between the parameters in the primary tumor and the rest of the prostate for the first 50 patients. Additionally, a logistic regression was performed with the Brix model parameters as predictors, and the binary outcome was defined as 1 within the primary tumor, and 0 in the rest of the prostate. The logistic regression was performed pixel by pixel, and cancer probability maps of the entire prostate gland were created based on the logistic regression model:

$$p_{i,j}(x_{1,i,j}, x_{2,i,j}, x_{3,i,j}) = \frac{e^{\beta_{0,i,j}+\beta_{1,i,j}x_{1,i,j}1+\beta_{2,i,j}x_{2,i,j}+\beta_{3,i,j}x_{3,i,j}}}{1+e^{\beta_{0,i,j}+\beta_{1,i,j}x_{1,i,j}1+\beta_{2,i,j}x_{2,i,j}+\beta_{3,i,j}x_{3,i,j}}} \tag{3.3}$$

where $p_{i,j}$ is the estimated probability of cancer in pixel i,j, $x_{n,i,j}$ are the model predictors (the Brix model parameters) in pixel i,j, and $\beta_{n,i,j}$ are the coefficients of the binomial fit in pixel i,j.

The predictive value of the logistic regression model was assessed by computing the Dice- and Jaccard similarity coefficients between a mask of the probability maps and a mask of the prostate gland. In the mask of the prostate gland pixels had the value 1 within the primary tumor, and 0 otherwise, and in the mask of the probability maps pixels had the value 1 where the probability of cancer was larger than a set threshold, and 0 otherwise. To obtain the optimal threshold value, a screening of Jaccard coefficients with 100 different threshold values between 0 and 1 was performed, and the threshold value that gave the closest match between the estimated probability and the delineated primary tumor across the patient population was

chosen.

The computer routines generated are available in the appendix.

4. Results

Out of the 110 patients initially recruited to the study, some withdrew for various reasons before the surgery. For other patients the ROI specifying the primary tumor was not available at the time of writing, thus the total number of patients analyzed in this study is $n = 48$ in the IV cohort, and $n = 31$ in the oral cohort.

4.1 RSI

Figure 4.1 shows the evolution of the RSI in two different patients. The figure shows the prostate gland in the pre-contrast image, with the RSI overlaid at different time points. At time $t = 0$ the CA appears in the iliac veins, and spreads through the tissue by perfusion in the following images. The primary tumor is delineated in the images. The signal intensity in the RSI map is shown only for voxels that showed a signal increase larger than the standard deviation of the absolute difference between two pre-contrast images, to separate actual signal increase from noise. There is a difference in CA uptake patterns both within the tumor, and within the prostate gland between the two patients: Patient A shows a relatively fast uptake, with high RSI in the early stages, while patient B shows a slow initial uptake, but with even higher uptake in the later time points. Difference in time activity curve between tumorous tissue and non-tumorous tissue is also clearly different for these two patients: In patient A the primary tumor clearly has a higher initial uptake than the surrounding tissue, while in patient B, no such tendency is observed. Rather, patient B shows significant CA uptake outside

the primary tumor. Figure 4.1 also illustrates the intra-tumor heterogeneity that is present in many of the tumors. Patient A shows larger variations in the RSI time-curve over the tumor than patient B, particularly in the early phases.

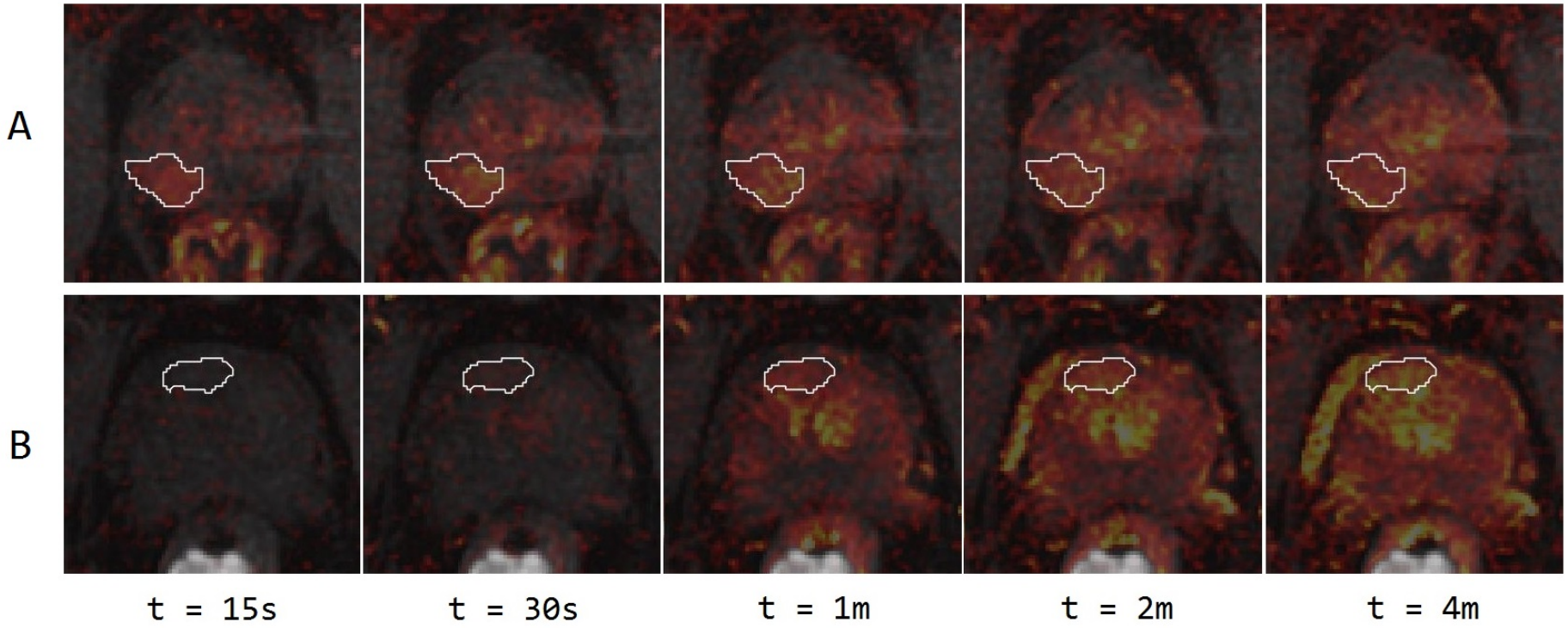

Figure 4.1: CA dynamics; RSI map overlaid onto the pre-contrast T1W axial images of the prostate gland at selected time-points for patients A and B. Dark red indicates low RSI, and yellow indicates high RSI. Patient A has a faster uptake, yet patient B shows a larger uptake than patient A. Patient A also shows a faster uptake in the primary tumor than the rest of the prostate This is not visible in patient B.

Figure 4.2 shows the RSI time-curve for two different voxels from regions within the tumors with different uptake. The RSI overlaid onto the pre-contrast image is shown to the left, and two voxels from regions with different CA uptake in the primary tumor are marked. To the right the RSI time-curve for the same two voxels are shown. This plot shows three different types of RSI versus time curves: Type 1 is the type illustrated by the *red voxel* in patient A, where the RSI in unit volume depicted is increasing throughout the imaging time. Type 2 is shown by both voxels in patient B, where the unit volume shows a relatively slow initial uptake and flattens out after the initial wash-in of CA, reaching a plateau that persists throughout the imaging. The type 3 curve is shown in the *blue voxel* of patient A, and is characterized by a fast wash-in of CA to a maximum, followed by a fast wash-out.

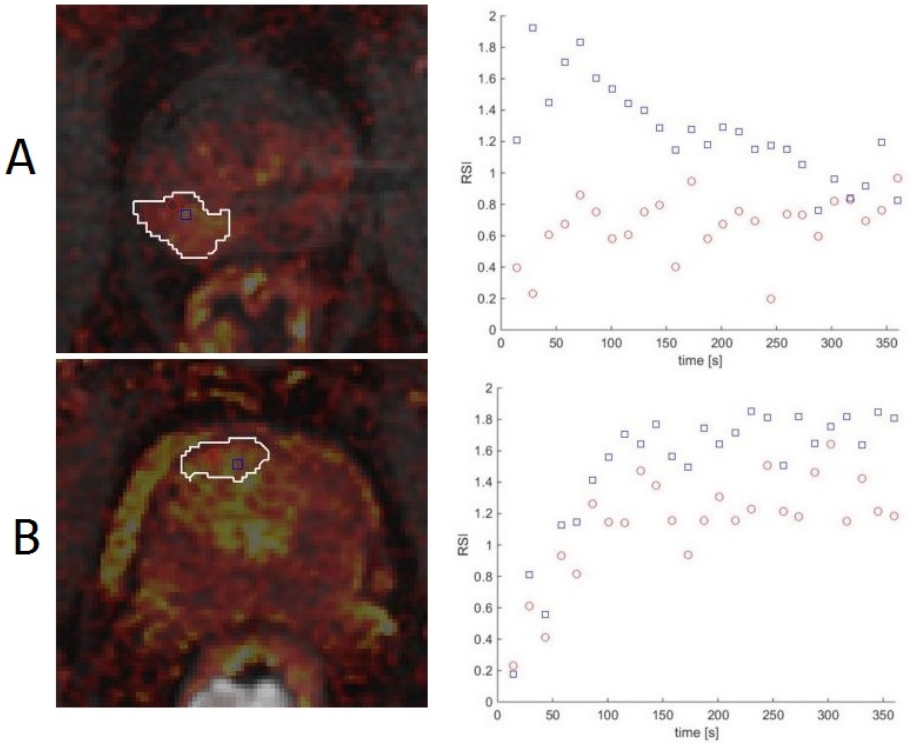

Figure 4.2: RSI time-curve from two selected voxels within the tumor for patient A and B. The pixels marked with a blue square in the images to the left are plotted as blue squares in the RSI time-curves to the right. Similarly for the red circles.

The distributions of CA in the primary tumors of patients A and B, shown as cumulative distribution plots at four different time points figure 4.3, clearly illustrates the heterogeneity of the CA accumulation within the tumor in both time and space. The bottom plot in figure 4.3 shows that the tumor in patient B has a fairly homogeneous accumulation of CA in the early stages, but the CA becomes more and more heterogeneous as time passes. Patient A on the other hand has a fairly constant distribution of CA throughout the first four minutes of the imaging.

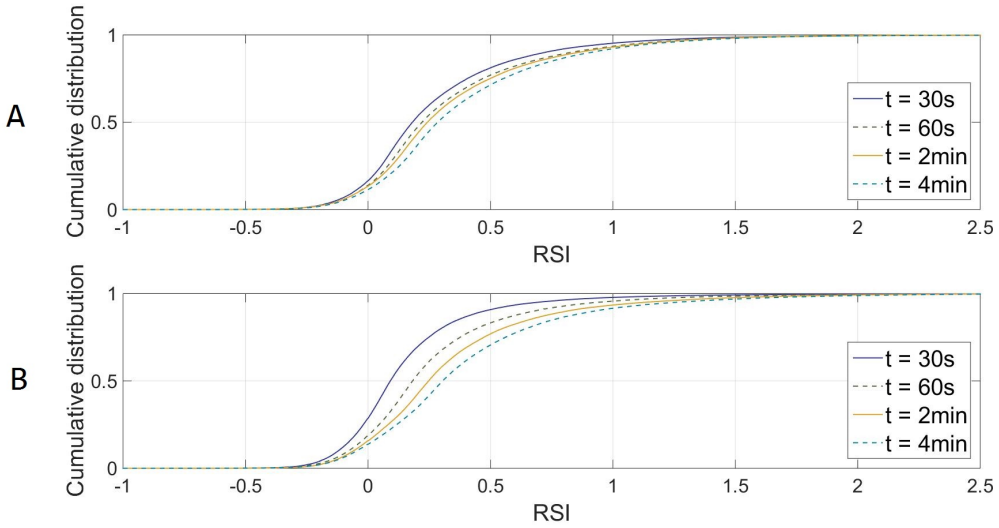

Figure 4.3: Cumulative distribution of the RSI within the primary tumors of patient A, and B, at different time-points.

4.2 semi-quantitative parameters

4.2.1 Within patients

Figures 4.4 and 4.5 show the iAUC and AUC for patients A and B. Looking at the iAUC map it is clear that the uptake in patient A is generally faster than that in patient B. For both patients the initial uptake is, however, heterogeneous showing regions of both high and low iAUC. Comparing the iAUC in figure 4.4 to the AUC in figure 4.5 reveals one major difference

between patients A and B. Whereas patient A shows areas of both low and high iAUC, the map of the AUC is more homogeneous with a relatively low total uptake throughout the patient, indicating that the areas of high iAUC predominantly consists of voxels displaying type 3 time-curves. In patient B areas of high initial uptake stands out as areas of high total uptake, which is indicative of type 1 or 2 time-curves.

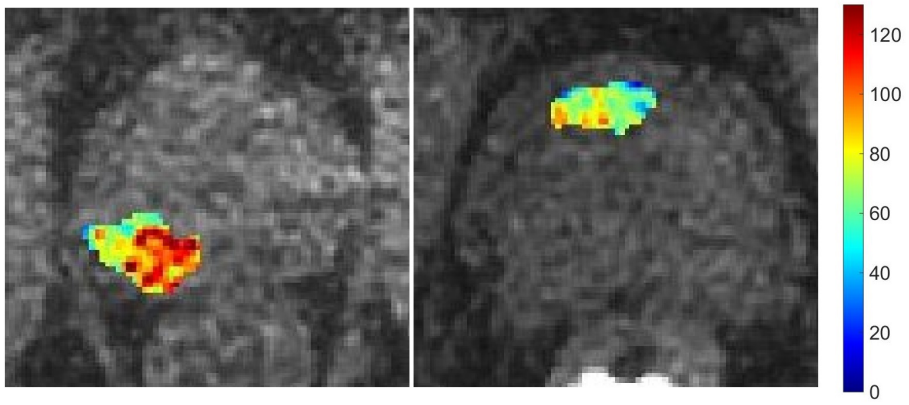

Figure 4.4: iAUC maps of the primary tumor in patients A (left) and B (right). Patient A shows a much higher uptake of CA in the first 45 seconds than patient B.

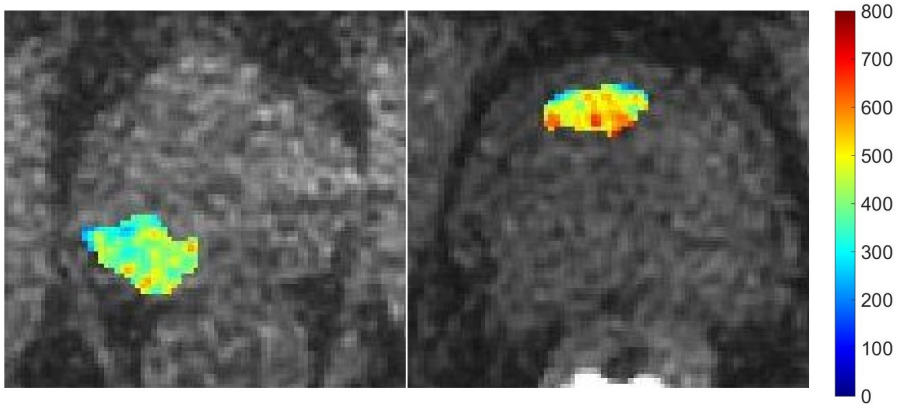

Figure 4.5: AUC maps of the primary tumor in patients A (left) and B (right). Patient B shows a higher and more heterogeneous total uptake of CA than patient A.

TTP maps for patients A and B are shown in figure 4.6. The areas of high iAUC in patient A corresponds to a low value in the TTP map, i.e. a fast wash-in of CA. For the majority of voxels within the tumor of patient B the TTP is more than four minutes, indicating type 1 or 2 time-curves.

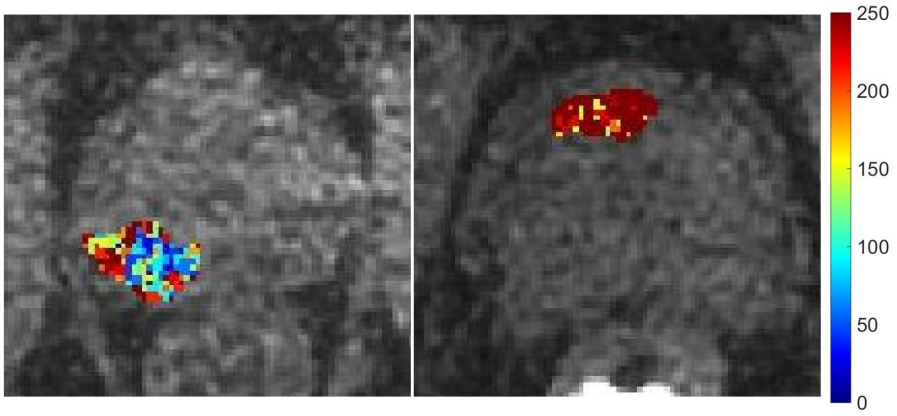

Figure 4.6: TTP maps of the primary tumor in patients A and B. In patient B most of the voxels show a time-to-peak larger than $250s$, indicating a very slow uptake of CA throughout the tumor.

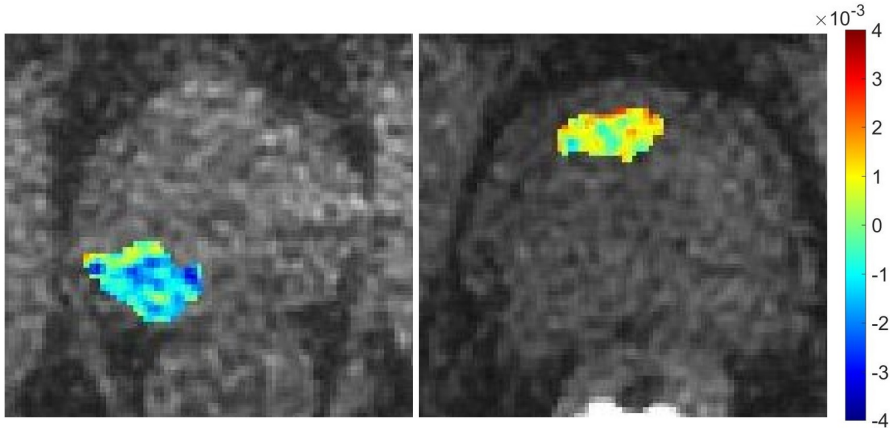

Figure 4.7: Slope of the wash-out curve in the tumor of patients A and B. A positive slope indicate that no wash-out phase was detected.

Figure 4.7 shows the slope of the wash-out curve for patients A and B. The regions of high iAUC and low TTP in patient A correspond to a steep wash-out curve, resulting in a fairly homogeneous AUC throughout the tumor. In patient B the slope of the wash-out curve is mainly positive throughout the tumor, resulting in a similarity between the maps of the iAUC and the AUC, and high TTP-values.

In summary, figures 4.4 through 4.7 paint a picture of two tumors with a slightly different blood perfusion. In patient A, a high iAUC, low TTP and negative wash-out slope indicates a tumor with a relatively fast blood exchange, where blood quickly washes in and out of the tumor tissue. Patient B shows a slow influx and slow wash-out of blood, but has a high AUC, indicating that the CA tends to accumulate in the region during the imaging.

4.2.2 Across the patient population

The median values of the semi-quantitative parameters for the entire patient population are shown in figure 4.8. The values are sorted in descending order in terms of their median iAUC value. The data indicates a that tumors with high iAUC tend to have a low TTP and a negative wash-out slope.

The normalized cumulative distributions of the semi-quantitative parameters are shown in figure 4.9. The distributions of the median, the 5% percentile, and the 95% percentile shows that TTP is particularly heterogeneous, both within tumors, and between different tumors.

The distributions of the median values of the semi-quantitative parameters are shown separately for the i.v. and the oral pimonidazole cohorts in figure 4.10. There were no significant differences between the parameters. The p-values obtained from a two-sided student t-test is displayed over the histograms.

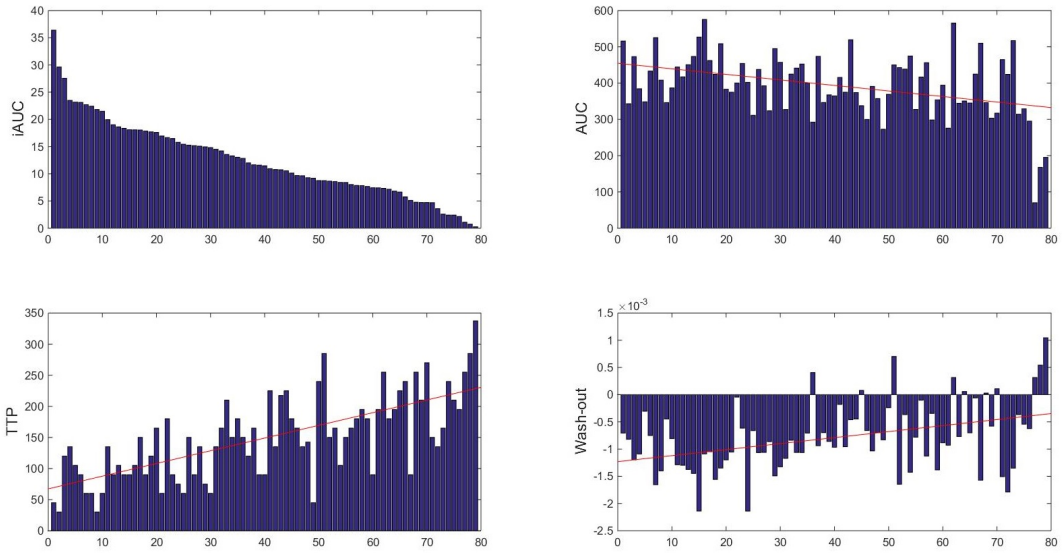

Figure 4.8: Plots of the median values of iAUC(top left), AUC(top right), TTP(bottom left) and the wash-out slope(bottom right), sorted by decreasing iAUC. The red line is the least squares regression line fitted to the data.

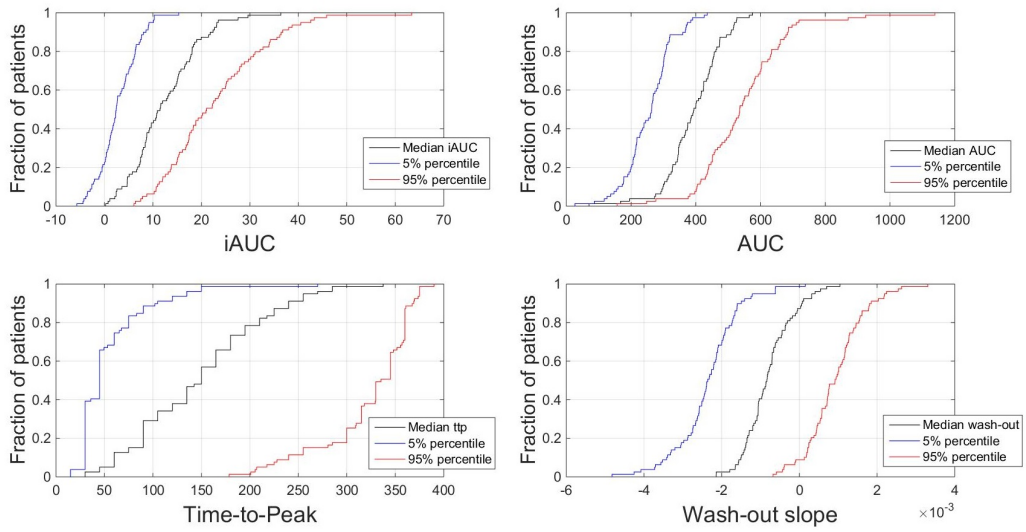

Figure 4.9: Normalized cumulative distributions of iAUC(top left), AUC(top right), TTP(bottom left) and wash-out slope(bottom right). The figure shows the distributions of the median, 5% percentile, and 95% percentile of the parameters.

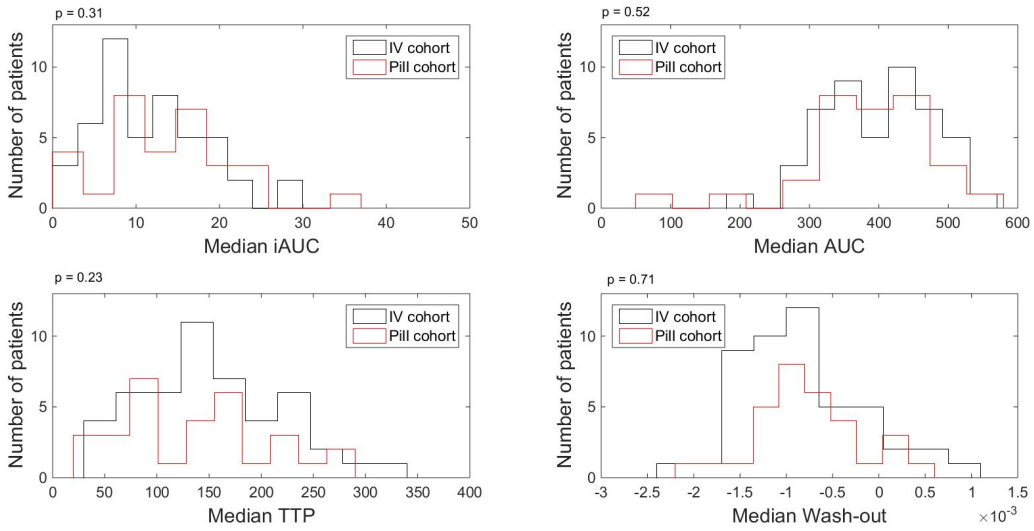

Figure 4.10: Histograms of the median values of iAUC(top left), AUC(top right), TTP(bottom left), and the wash-out slope(bottom right). The patients who had the pimonidazole administered intravenously are shown in black, and patients who had the pimonidazole administered orally are shown in red.

4.3 Fitting the Brix model

The fitting of the Brix model to the RSI time-curves is illustrated in figure 4.11. In table 4.1 the Brix model parameters corresponding to the fits are listed. The blue unit volume in patient A (figure 4.11) has the fastest elimination of CA from the plasma k_{el}, corresponding to a steep wash-out curve. The red unit volume increases in RSI throughout the scan-time, and its k_{el} value is essentially zero. A qualitative examination of figure 4.11 and table 4.1 also shows that the maximum uptake is related to the amplitude A, and that a steep increase in RSI is related to a high k_{ep}.

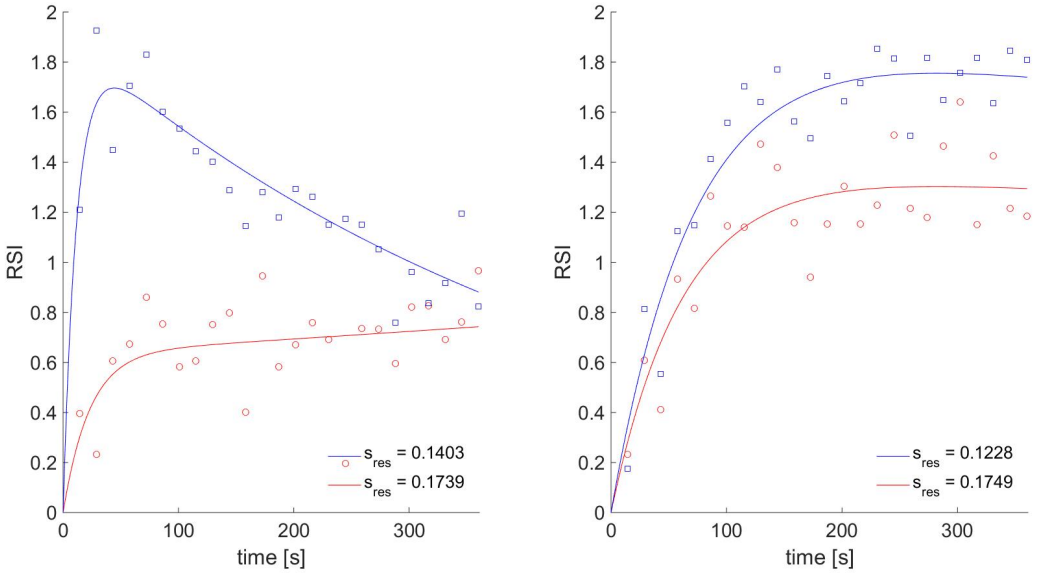

Figure 4.11: The fitting of the Brix model for patients A(left) and B(right) for the voxels indicated in figure 4.2.

	A	k_{ep} $[s^{-1}]$	k_{el} $[s^{-1}]$	s_{res}
Patient A:				
Blue unit volume	1.81	0.08	0.002	0.14
Red unit volume	0.64	0.03	2.6×10^{-14}	0.17
Patient B				
Blue unit volume	1.80	0.01	3.8×10^{-4}	0.12
Red unit volume	1.35	0.02	2.0×10^{-4}	0.17

Table 4.1: Values of the Brix model parameters associated with the model fits in figure 4.11. The *Blue unit volume* references the data points marked with blue squares in the figure, and the *Red unit volume* references the data points marked with red circles.

The quality of the model fits are illustrated in figures 4.12 through 4.14. At the top of figure 4.12 a plot of the residuals from the two example unit volumes in patient A, shown in figure 4.11, are plotted against time, and at the bottom a histogram of the residuals in the entire tumor of patient A is shown together with a plot of the standard normal distribution.

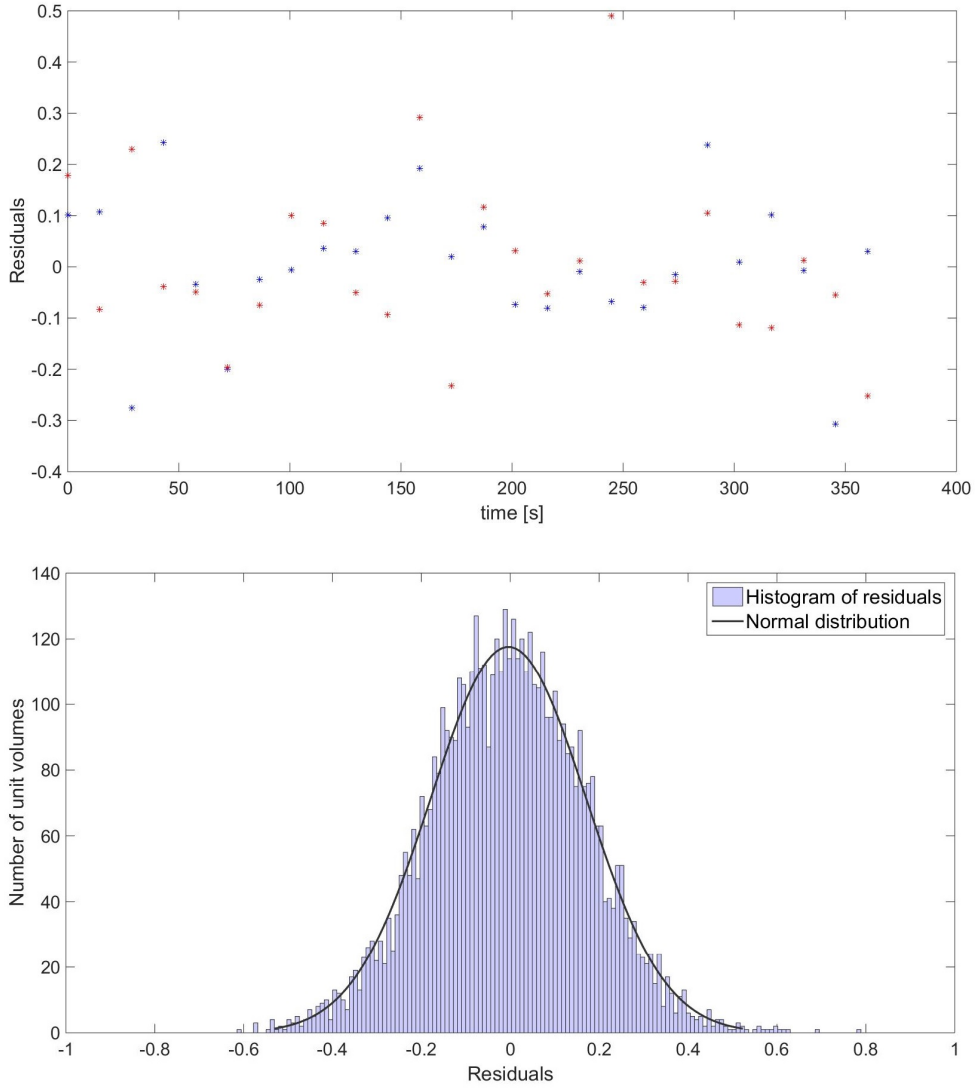

Figure 4.12: The residuals of the fitted Brix model. Top: The residuals plotted as a function of time for the two unit volumes introduced in figure 2 in patient A. No systematic behavior of the residuals indicates that the demand of homoscedasticity is fulfilled. Bottom: Histogram of the residuals in the entire tumor of patient A. The black line is the standard normal distribution with mean $\mu = 0.0$ and standard deviation $\sigma = 0.18$. The residuals comply with the demand of normally distributed errors.

Figure 4.12 reveals no systematic behavior of the residuals across the measurements in the plot of the residuals as a function of time, i.e. there is no indication of any systematic variance not accounted for by the model. The histograms of the residuals show that they are normally distributed with mean zero, thus the model is concluded to adequately describe the systematic behavior of the measurements.

Figure 4.13 shows the histogram of the residual standard error s_{res} in all voxels of all patients. 0.8% of the voxels failed to comply with the demand of $s_{res} < 0.4$, and were excluded from further analysis. The rightmost bin in the histogram in figure 4.13 contains these 161 voxels.

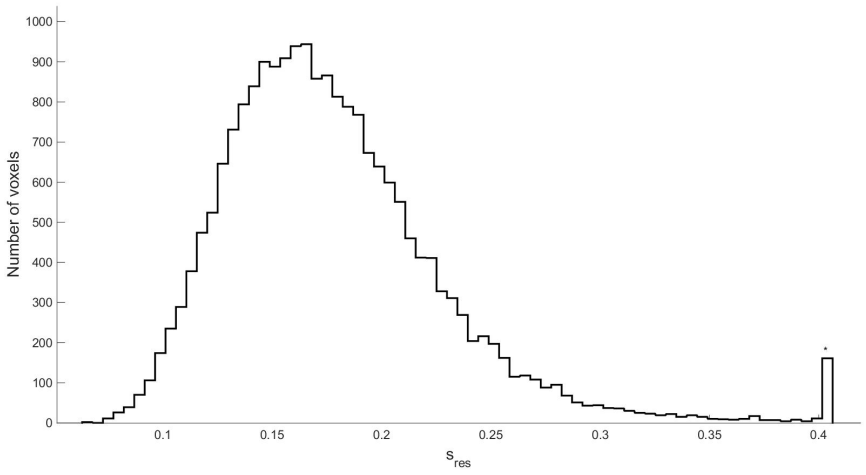

Figure 4.13: Histogram of s_{res} for all voxels in all patients. The leftmost bin contains the 161(0.8%) voxels with $s_{res} > 0.4$.

Figure 4.14 shows the histogram of all the residuals in the tumors of all the patients. The residuals are normally distributed with mean $\mu = 0$, and the Brix model is concluded to be capable of adequately accounting for the systematic variations of the data.

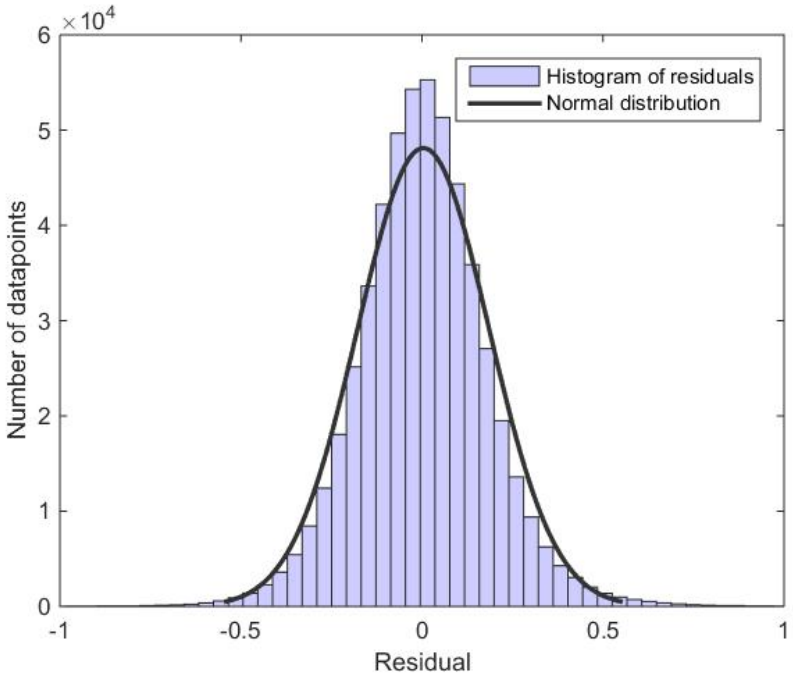

Figure 4.14: Histogram of the residuals from the fitted Brix model for all voxels in all patients. The standard normal distribution with mean $\mu = 0.0$ and standard deviation $\sigma = 0.2$ is shown in the black line.

4.4 Brix model parameters

4.4.1 Within patients

Figure 4.15 shows the Brix model parametric maps of patient A. Areas of high k_{ep} and k_{el} correspond to the areas of high iAUC, low TTP and steep wash-out curve in figures 4.4,4.6 and 4.7, wheras the amplitude map is concordant with the AUC map in figure 4.5.

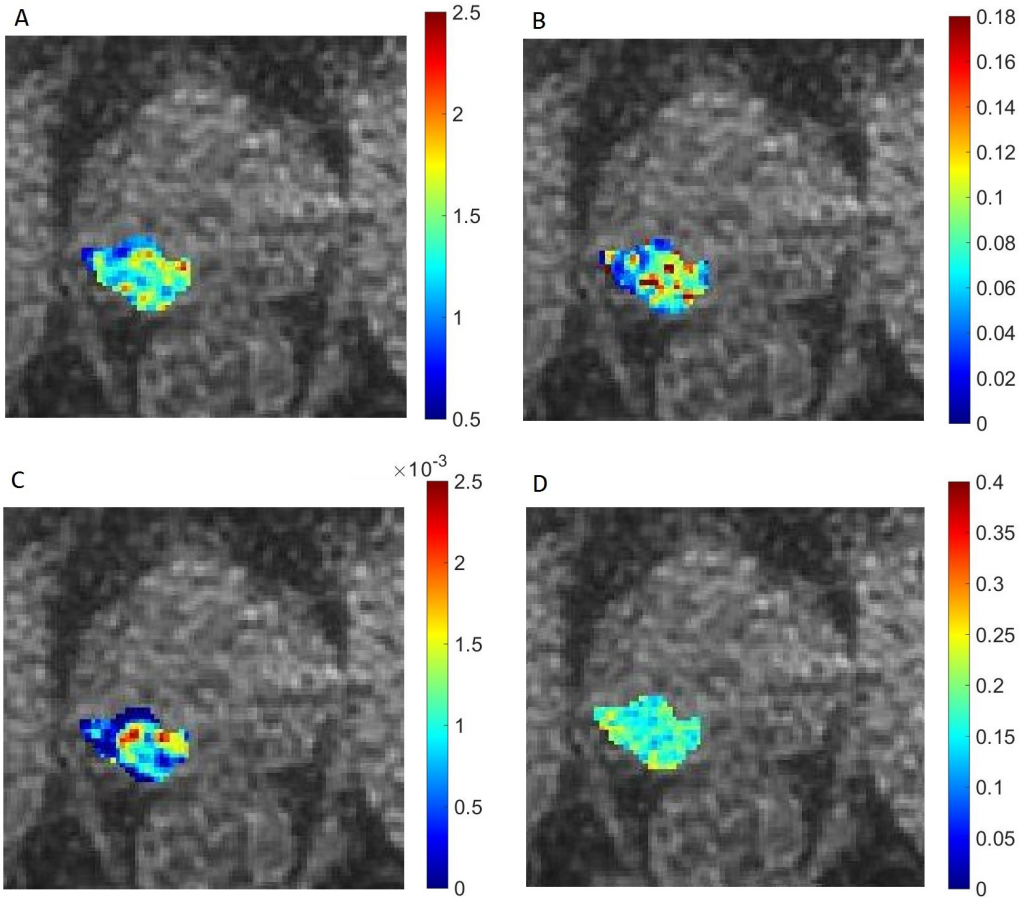

Figure 4.15: Parametric maps from the Brix modeling of the RSI time-curve. A: The (dimensionless) amplitude A, B: The transfer rate constant from blood plasma to the EES k_{ep} $[s^{-1}]$, C: The rate constant of elimination of CA from the blood plasma k_{el} $[s^{-1}]$, D: The residual standard error s_{res}.

4.4.2 Across patient population

Figure 4.16 shows the median values of the Brix model parameters for the entire patient population, sorted in descending order in terms of their median amplitude. The least squares regression lines of the data are shown by the red lines in the plots, indicating a weak tendency of high amplitude tumors having a high k_{el}. In one of the patients the median value of k_{ep} was nonphysically high (more than 36 times higher than median of the other patients), and that patient has thus been excluded from further analysis.

The overall distributions of the Brix model parameters for the patient population are shown by normalized cumulative distributions in figure 4.17. The figure shows the distributions of the median, the 5% percentile, and the 95% percentile of the parameters, and of the residual standard error.

The distributions of the median values of the Brix model parameters are compared between the two patient cohorts by histograms in figure 4.18. No significant difference is observed between the cohorts in the Brix model parameters. The p-values from a two sided student t-test is displayed over the histograms.

Figure 4.19 shows the correlations between the pharmacokinetic parameters. A strong correlation between the k_ep and the iAUC, between the k_el and the wash-out, and between the amplitude and the AUC is observed.

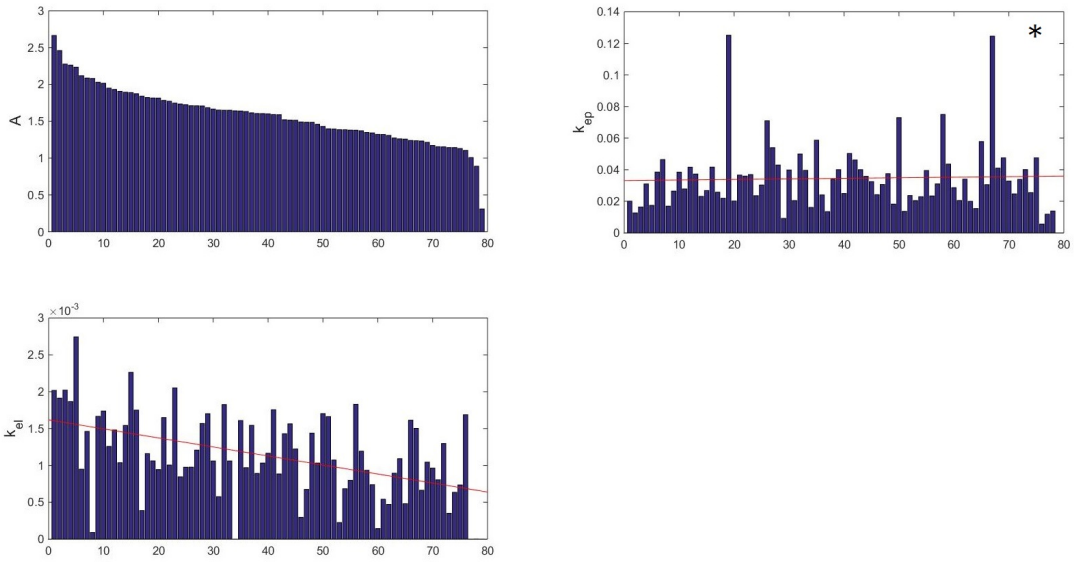

Figure 4.16: Plots of the median values of the Brix model parameters, sorted by decreasing amplitude A. The plots show the amplitude(top left). k_{ep}(top right), and the k_{el}(bottom left).
*In one of the patients the median k_{ep} was nonphysically high, and has been removed from this figure, and further analysis.

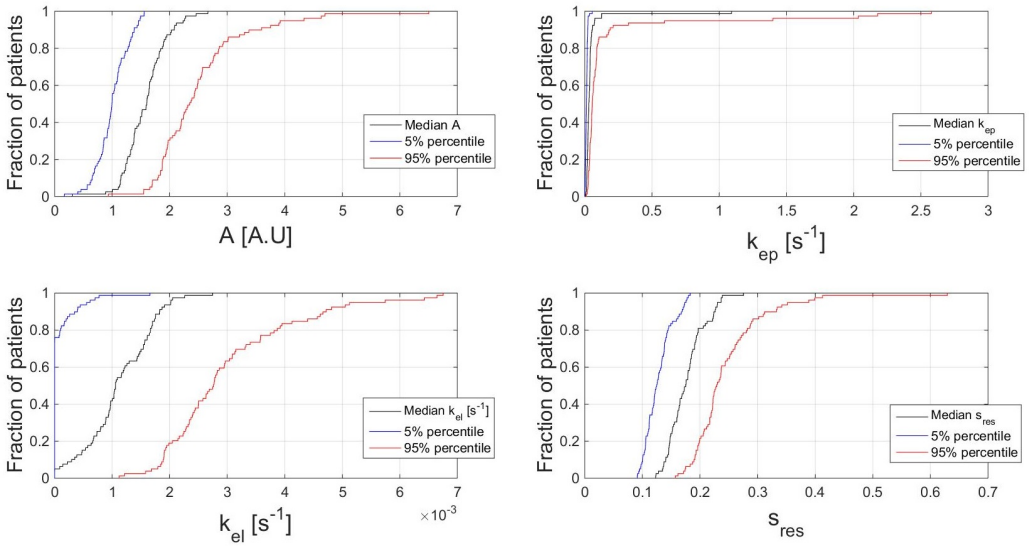

Figure 4.17: Normalized cumulative distributions of the median, 5% percentile, and 95% percentile of the amplitude A(top left), the k_{ep}(top right), k_{el}(bottom left), and s_{res}(bottom left).

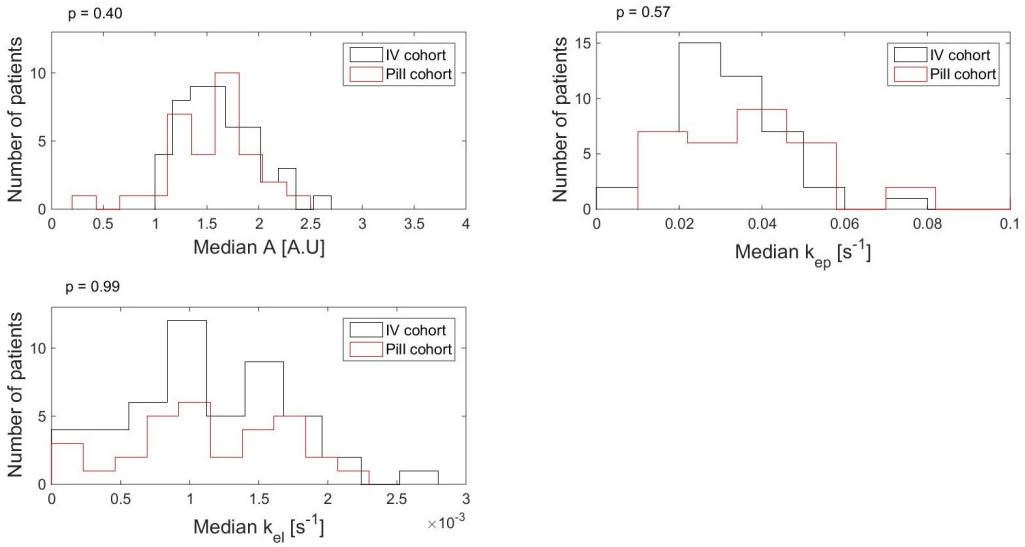

Figure 4.18: Histograms of the median values of the Brix model parameters for all patients. Patients who were given pimonidazole intravenously are shown in black, and patients who were given pimonidazole orally are shown in red.

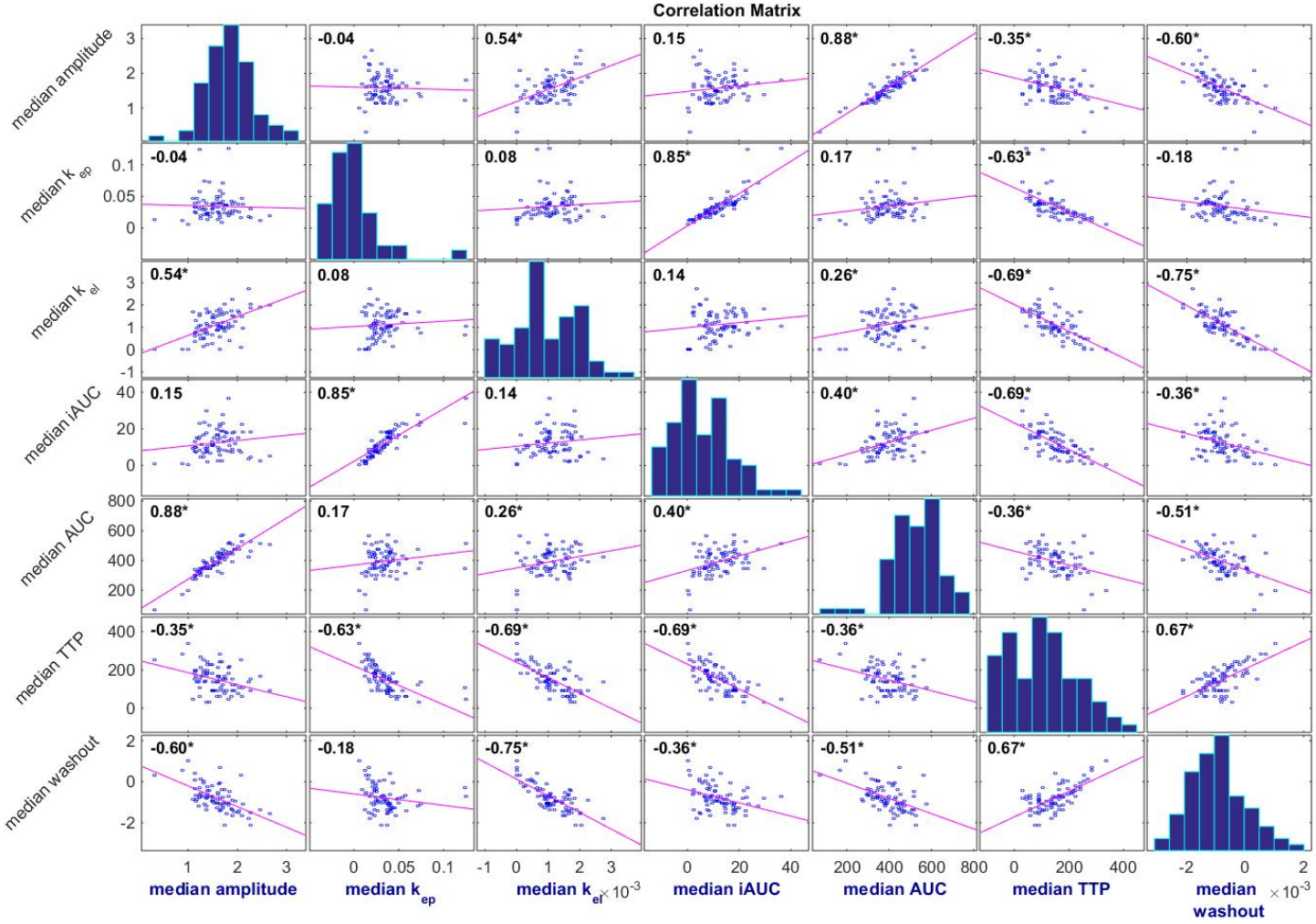

Figure 4.19: Scatterplot matrix of correlations between the pharmacokinetic parameters for all the patients ($n = 79$). The Pearson correlation coefficient is shown in the upper left corner of the plots.
Significant correlations($p < 0.05$).

A scatter plot of the median values of the pharmacokinetic parameters, and their correlations to each other is shown in figure 4.19. The figure shows how the different semi-quantitative and quantitative parameters are related. Each sublot shows the median values of the parameters in the entire patient population(both cohorts), $n = 79$.

4.5 Comparing image parameters to clinical data

Of the clinical parameters in table 3.2 on page 28, three showed a significant difference($p < 0.05$) between the cohort that received the pimonidazole intravenously and the cohort that recieved it orally. Pimonidazole score in the IV cohort (mean: 2.3 SD: 1.1) was significantly higher than in the oral cohort(mean: 1.5 SD: 1.2)($p = 0.001$). Additionally the Gleason score from the prostatectomy was higher in the IV cohort(mean: 7.4 SD: 0.9) than in the oral cohort (mean: 7.0 SD: 0.9)($p = 0.03$), and the D'Amico risk classification was higher in the IV cohort (mean: 2.5 SD: 0.5) than in the oral cohort (mean: 2.5 SD: 0.6) ($p = 0.04$).

The parameters that showed a difference between the two cohorts at 5% significance ($p < 0.05$) are shown with box plots in figure 4.20.

In figures 4.21 through 4.27 the median values of the image parameters are plotted, and color coded according to the pimonidazolenidazole score of the tumors: Green colored bars are tumors with pimonidazole score ≤ 1.5, blue bars are tumors with pimonidazole score between 1.5 and 3.5, and red bars are tumors with pimonidazole score ≥ 3.5.

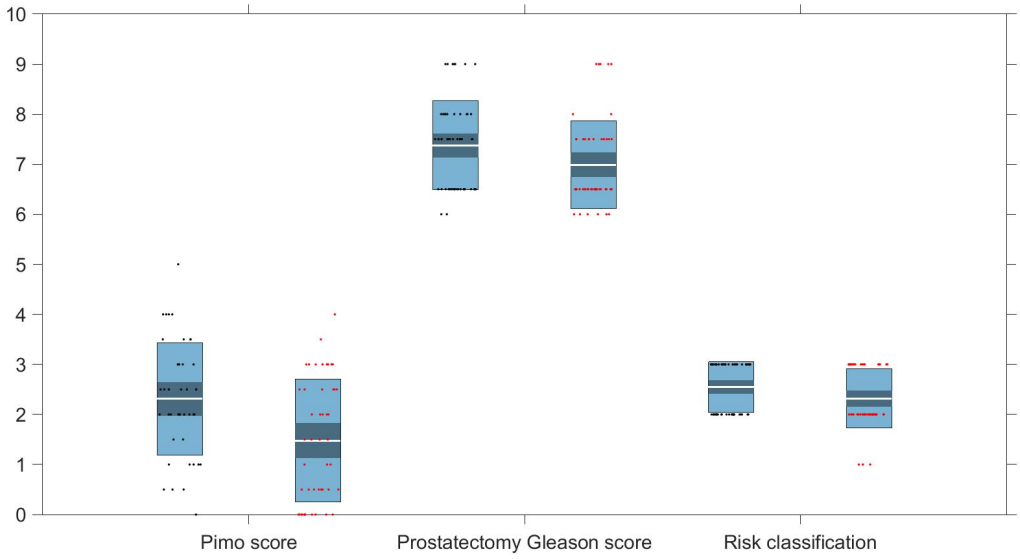

Figure 4.20: Box plots of the clinical factors that showed a statistical difference at 5% significance. The dark areas shows one standard deviation, and the light areas shows the 95% confidence interval. The raw data distribution is shown with black markers for the IV cohort, and red markers for the pill cohort.

Table 4.2 shows the Pearson correlation coefficients of all parameters, and table 4.3 shows the Spearman correlations coefficients. Significant correlations are highlighted. Scatter plots and correlations, with p-values are available in the appendix. In the table the median value in the tumor of the pharmacokinetic parameters is shown.

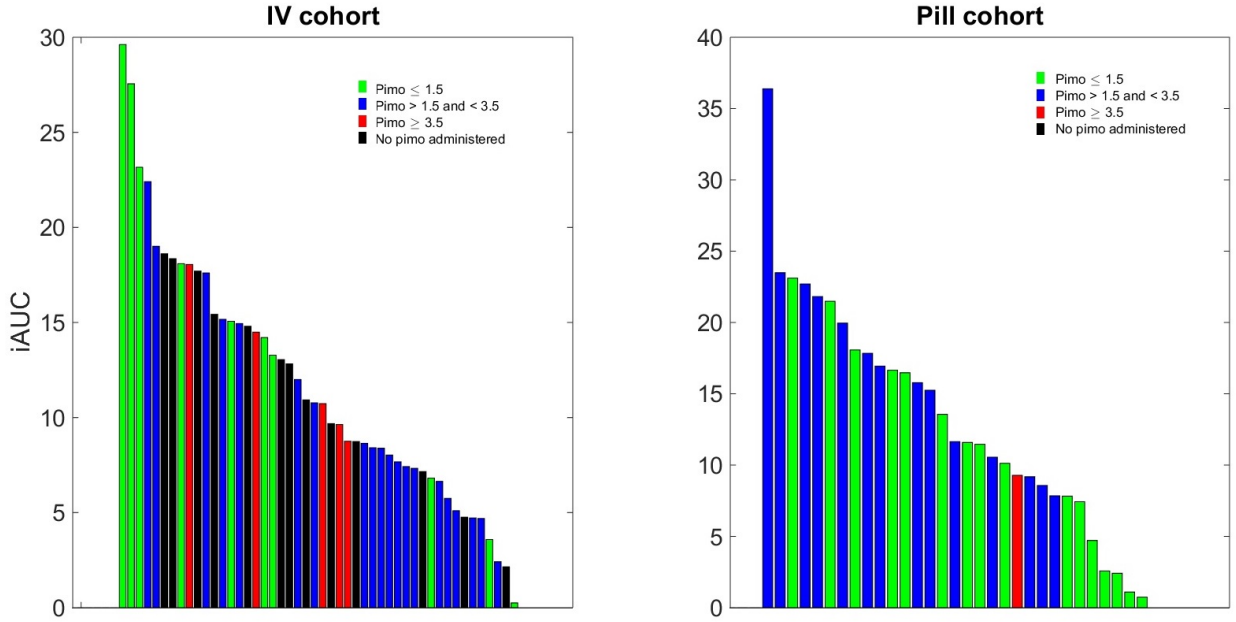

Figure 4.21: The median iAUC of the patients in the two cohorts in descending order. Color coded according to pimonidazole score.

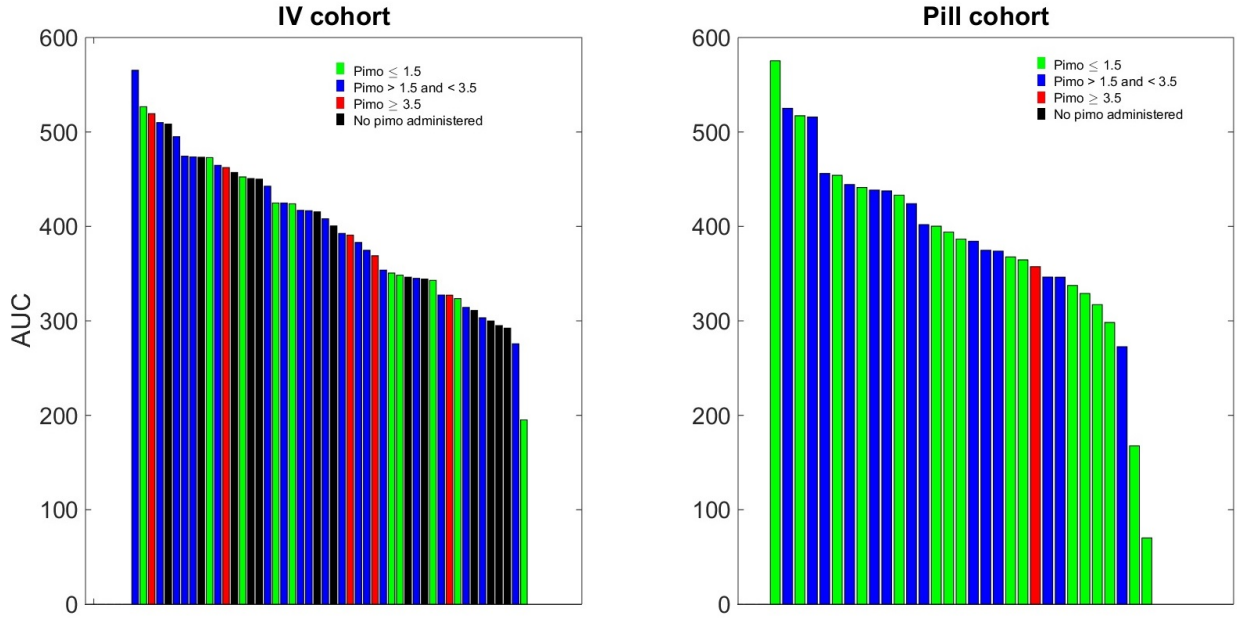

Figure 4.22: The median AUC of the patients in the two cohorts in descending order. Color coded according to pimonidazole score.

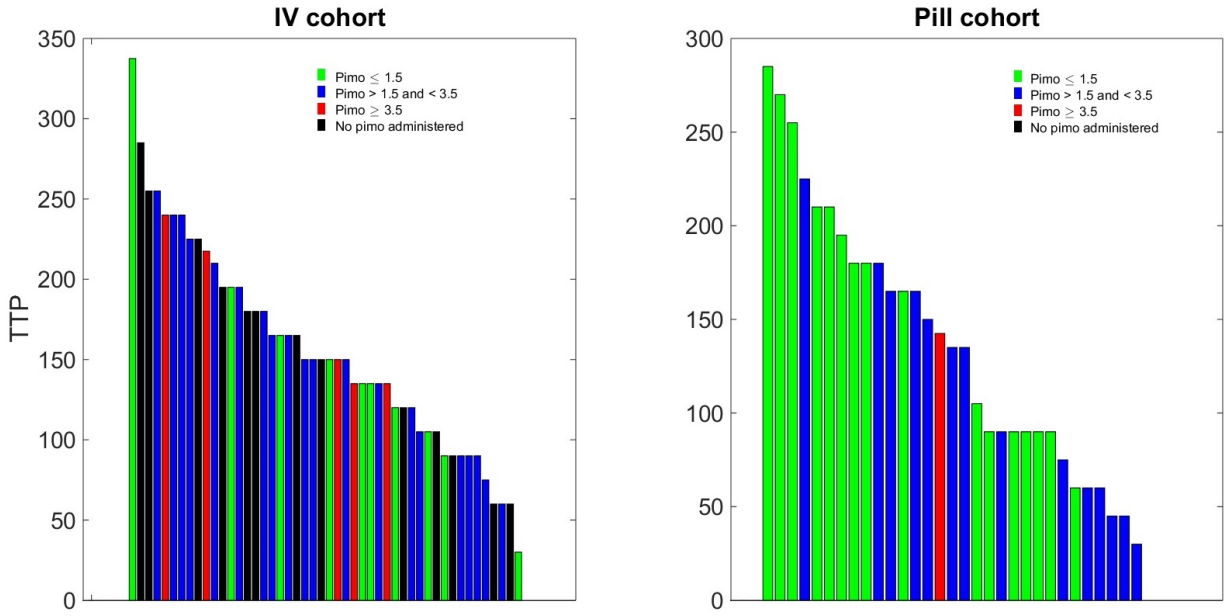

Figure 4.23: The median TTP of the patients in the two cohorts in descending order. Color coded according to pimonidazole score.

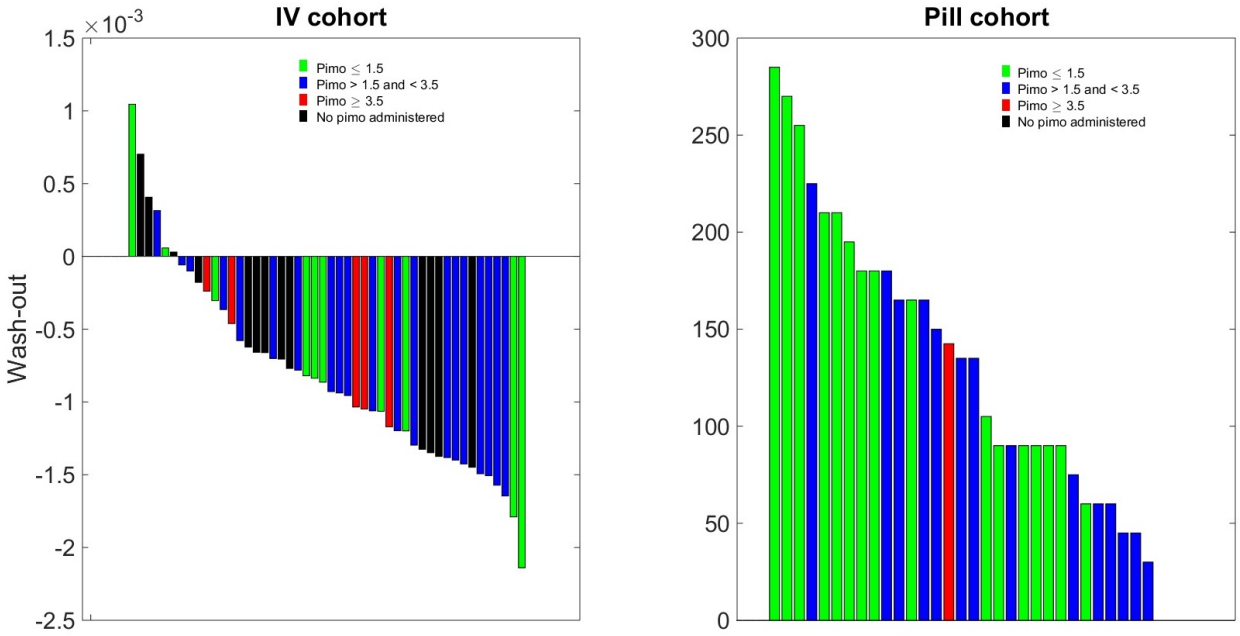

Figure 4.24: The median wash-out of the patients in the two cohorts in descending order. Color coded according to pimonidazole score.

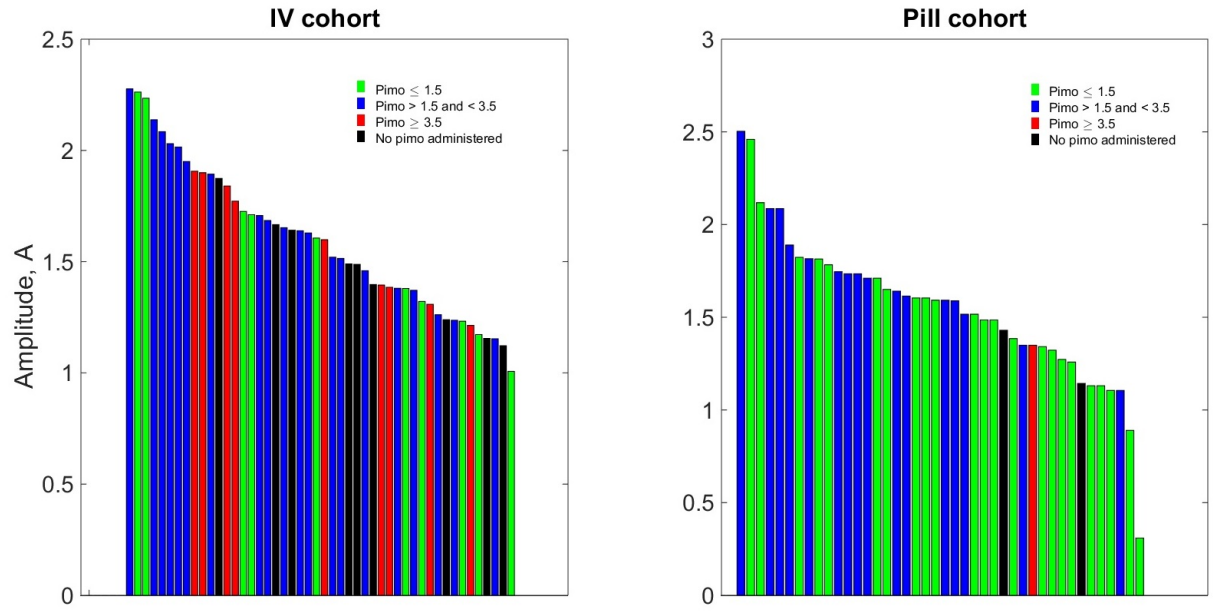

Figure 4.25: The median amplitude, A, of the patients in the two cohorts in descending order. Color coded according to pimonidazole score.

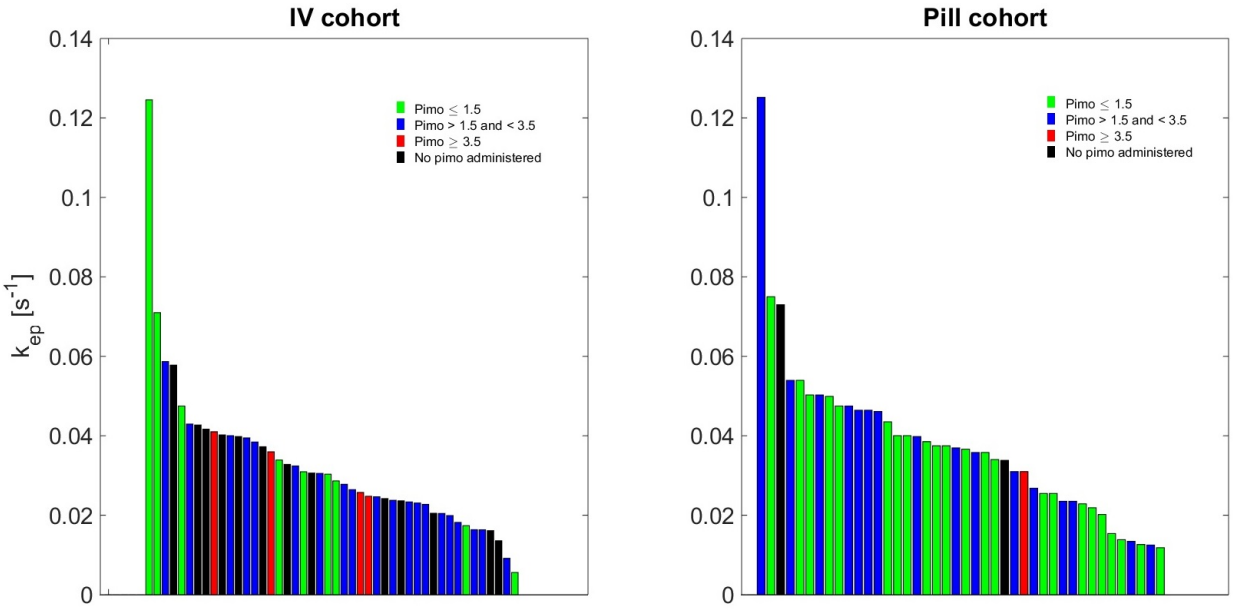

Figure 4.26: The median k_{ep} of the patients in the two cohorts in descending order. Color coded according to pimonidazole score.

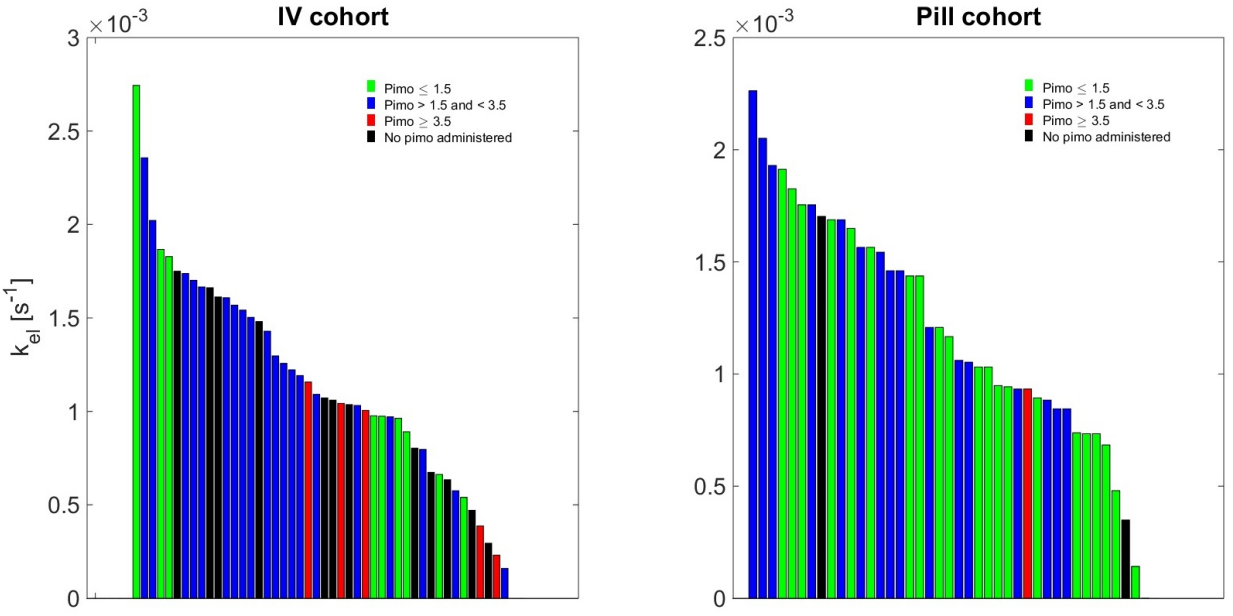

Figure 4.27: The median k_{el} of the patients in the two cohorts in descending order. Color coded according to pimonidazole score.

Table 4.2: Pearson correlation coefficients between the clinical data and image parameters for both patient cohorts.

IV cohort	1	2	3	4	5	6	7	8	9	10	11	12	13	14	15	16
1. Age																
2. Largest extent	0.08															
3. PSA	0.16	0.17														
4. Gleason score from core biopsies	−0.07	0.09	0.04													
5. Gleason score from prostatectomy	0.15	0.12	0.15***	0.62												
6. Clinical T-stage	−0.01	0.23	−0.09	0.24	0.20											
7. Pathological T-stage	−0.06	0.45***	0.24	0.22	0.14	0.13										
8. D'Amico risk classification	−0.03	0.20	0.31**	0.61***	0.50***	0.33**	0.31**									
9. iAUC	−0.20	0.13	0.05	0.16	0.15	−0.01	0.02	0.11								
10. AUC	0.04	0.05	0.27	0.19	0.19	0.12	0.12	0.26	0.27							
11. TTP	0.20	0.04	−0.11	−0.22	−0.09	0.05	0.10	−0.10	−0.68 ***	−0.30 *						
12. Wash-out	0.21	−0.10	0.01	−0.25	0.04	−0.05	−0.14	−0.05	−0.35 **	−0.43 ***	0.73***					
13. Amplitude A	0.12	0.00	0.21	0.19	0.05	0.05	0.07	0.23	0.03	0.88***	−0.30 *	−0.54 ***				
14. k_{ep}	0.00	−0.05	0.04	0.14	0.11	−0.15	−0.22	0.13	0.49***	−0.10	−0.35 **	−0.02	−0.12			
15. k_{el}	0.02	−0.09	0.05	0.12	−0.11	−0.10	−0.12	0.02	0.08	0.17	−0.68 ***	−0.77 ***	0.48***	0.17		
16. pimonidazole score	0.23	0.40***	−0.12	−0.02	0.03	0.30	0.42***	−0.01	−0.14	0.09	0.16	0.01	−0.02	−0.21	−0.22	
Pill cohort																
1. Age																
2. Largest extent	−0.01															
3. PSA	−0.02	0.53														
4. Gleason score from core biopsies	0.25	0.09	0.20													
5. Gleason score from prostatectomy	0.31*	0.18	0.32**	0.38**												
6. Clinical T-stage	−0.02	0.15	−0.09	0.13	0.42***											
7. Pathological T-stage	0.26	0.39**	0.21	0.16	0.15	0.20										
8. D'Amico risk classification	0.05	0.38**	0.28	0.73***	0.27	0.23	0.19									
9. iAUC	−0.29	0.17	0.17	0.17	0.19	0.04	0.09	0.12								
10. AUC	0.15	0.21	0.18	0.17	0.26	−0.16	0.10	−0.01	0.56***							
11. TTP	−0.08	0.05	0.11	−0.30	−0.25	0.00	−0.01	−0.16	−0.69 ***	−0.47 **						
12. Wash-out	−0.11	−0.16	−0.09	−0.17	−0.22	0.09	−0.19	−0.02	−0.41 **	−0.65 ***	0.60***					
13. Amplitude A	0.21	0.16	0.14	0.25	0.25	−0.12	0.21	−0.06	0.17	0.44**	−0.14	−0.45 **				
14. k_{ep}	−0.19	0.13	0.11	0.24	0.14	0.09	0.09	0.18	0.63***	0.13	−0.47 **	0.09	0.07			
15. k_{el}	0.22	0.13	−0.05	0.17	0.10	−0.10	0.34*	−0.05	−0.17	0.06	−0.22	−0.36 *	0.59***	0.16		
16. pimonidazole score	0.09	0.40***	−0.01	0.08	0.20	0.21	0.48***	0.22	0.33	0.25	−0.16	−0.31	0.26	0.06	0.16	

*p<0.05, **p<0.03, ***p<0.01

Table 4.3: Spearman correlation coefficients between the clinical data and image parameters for both patient cohorts.

IV cohort	1	2	3	4	5	6	7	8	9	10	11	12	13	14	15	16
1. Age																
2. Largest extent	−0.02															
3. PSA	0.18	0.21														
4. Gleason score from core biopsies	−0.08	0.07	−0.04													
5. Gleason score from prostatectomy	0.11	0.11	0.18	0.61***												
6. Clinical T-stage	−0.07	0.19	−0.09	0.19	0.13											
7. Pathological T-stage	−0.11	0.58***	0.17	0.22	0.15	0.11										
8. D'Amico risk classification	−0.10	0.18	0.24	0.63***	0.49***	0.30*	0.31**									
9. iAUC	−0.23	0.22	0.10	0.12	0.15	0.05	0.05	0.10								
10. AUC	0.10	0.03	0.17	0.14	0.13	0.07	0.11	0.23	0.27							
11. TTP	0.16	0.02	−0.10	−0.17	−0.09	0.07	0.13	−0.10	−0.69 ***	−0.30 *						
12. Wash-out	0.14	−0.04	0.16	−0.20	0.05	−0.01	−0.12	−0.06	−0.34 **	−0.49 ***	0.69***					
13. Amplitude A	0.16	0.02	0.11	0.14	0.07	0.06	0.08	0.23	0.07	0.90***	−0.30 *	−0.57 ***				
14. k_{ep}	−0.28	0.14	0.04	0.09	0.12	0.04	−0.08	0.02	0.91***	0.05	−0.75 ***	−0.31 *	−0.13			
15. k_{el}	0.07	−0.06	0.00	0.07	−0.14	−0.05	−0.11	0.01	0.06	0.14	−0.66 ***	−0.73 ***	0.41***	0.14		
16. pimonidazole score	0.26	0.42**	−0.16	0.03	0.03	0.29	0.39**	−0.01	−0.05	0.05	0.20	0.07	0.01	−0.13	−0.16	
Pill cohort																
1. Age																
2. Largest extent	−0.02															
3. PSA	0.13	0.41***														
4. Gleason score from core biopsies	0.28	0.11	0.22													
5. Gleason score from prostatectomy	0.26	0.24	0.26	0.48***												
6. Clinical T-stage	−0.02	0.24	−0.09	0.11	0.38**											
7. Pathological T-stage	0.26	0.43***	0.22	0.17	0.16	0.19										
8. D'Amico risk classification	0.05	0.33**	0.29*	0.75***	0.33**	0.20	0.19									
9. iAUC	−0.28	0.06	0.07	0.12	0.22	0.00	0.04	0.09								
10. AUC	0.10	0.23	0.14	0.24	0.29	−0.04	0.16	0.11	0.50***							
11. TTP	−0.01	0.06	−0.08	−0.26	−0.32	−0.04	−0.03	−0.20	−0.66 ***	−0.31						
12. Wash-out	−0.07	−0.15	−0.19	−0.09	−0.26	0.01	0.23	0.05	−0.43 **	−0.65 ***	0.49**					
13. Amplitude A	−0.01	0.07	0.06	0.25	0.15	−0.06	0.23	0.05	0.26	0.58***	−0.13	−0.46 **				
14. k_{ep}	−0.02	0.06	0.19	0.25	0.24	0.05	0.01	0.19	0.44**	−0.12	−0.53 ***	0.15	0.03			
15. k_{el}	0.14	0.11	0.11	0.21	0.17	0.03	0.32*	0.03	−0.22	0.01	−0.17	−0.34	0.51***	0.30		
16. pimonidazole score	0.04	0.42***	−0.07	0.12	0.20	0.21	0.50***	0.22	0.32	0.28	−0.12	−0.26	0.30	−0.01	0.11	

*p<0.05, **p<0.03, ***p<0.01

A percentile screening of the correlation coefficients and the significance between the pharmacokinetic parameters and the pimonidazole score is shown in figures 4.28 and 4.29. The significance is higher in the high percentile region for correlations between pimonidazole score and k_{ep} in both cohorts, and between pimonidazole score and the slope of the wash out curve in the oral cohort. Additionally the k_{ep}, and iAUC shows a stronger correlation to pimonidazole score in the lower percentile range in the oral cohort.

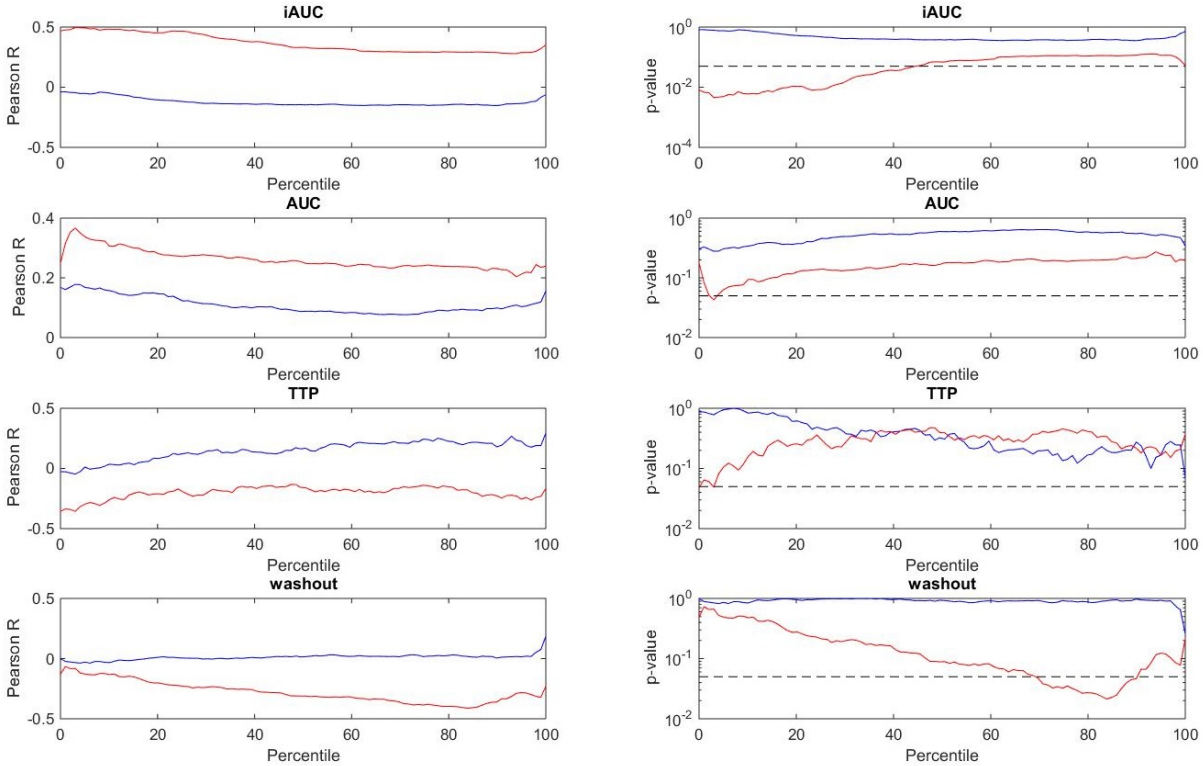

Figure 4.28: Percentile screening of the correlation between the semi-quantitative parameters and pimonidazole score. The IV cohort is shown in blue, and the oral cohort is shown in red. The right column shows the Pearson R-coefficients, and the left column shows the p-values. The stapled black line is the $p = 0.05$ significance line.

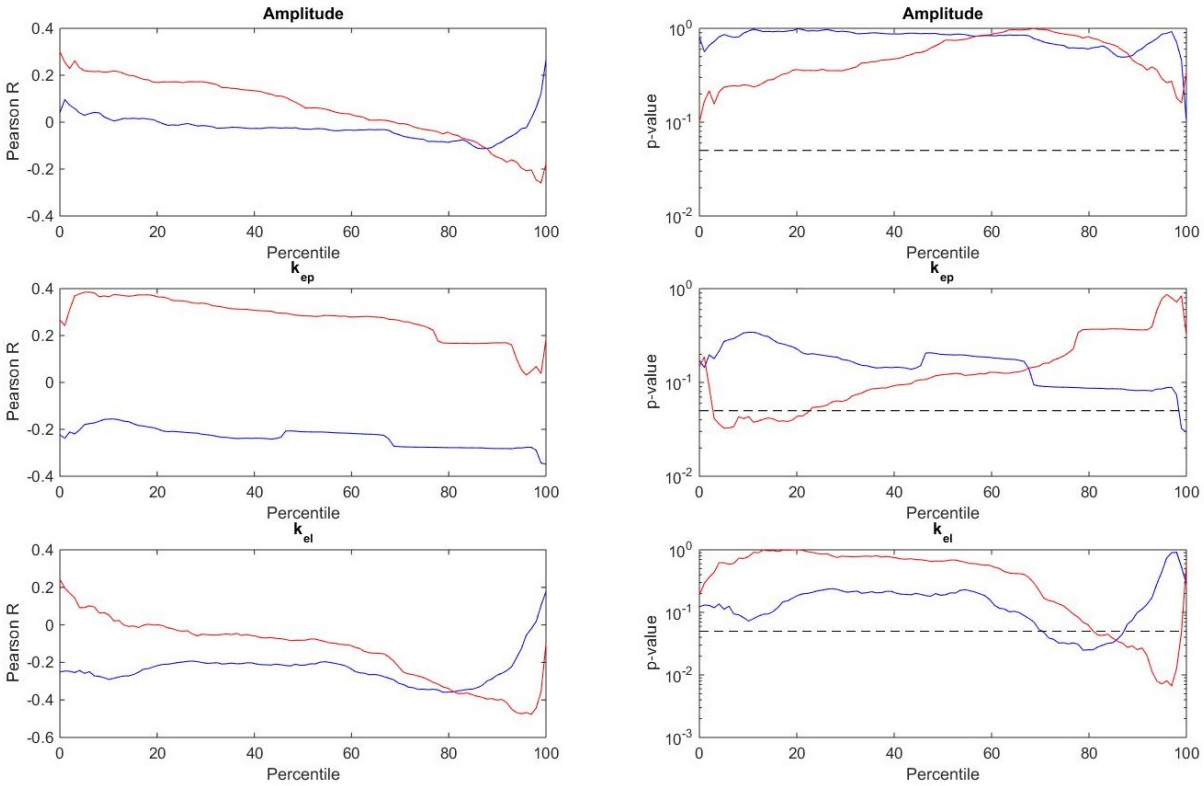

Figure 4.29: Percentile screening of the correlation between the Brix model parameters and pimonidazole score. The IV cohort is shown in blue, and the oral cohort is shown in red. The right column shows the Pearson R-coefficients, and the left column shows the p-values. The stapled black line is the $p = 0.05$ significance line.

4.6 Comparing the Brix model coefficients between index tumor and prostate tissue.

A two sided student t-test rejected the null-hypothesis that there was a difference in the Brix model parameters between the index tumor tissue, and the rest of the prostate gland ($p < 0.001$). Thus, under the assumption that the tissue outside the primary tumor is normal tissue, the Brix model parameters alone are insufficient to discriminate cancerous tissue. Examples of the probability maps generated from a logistic regression, with Brix model parameters as predictors, and location of the index tumor as a binary outcome is shown in figure 4.30.

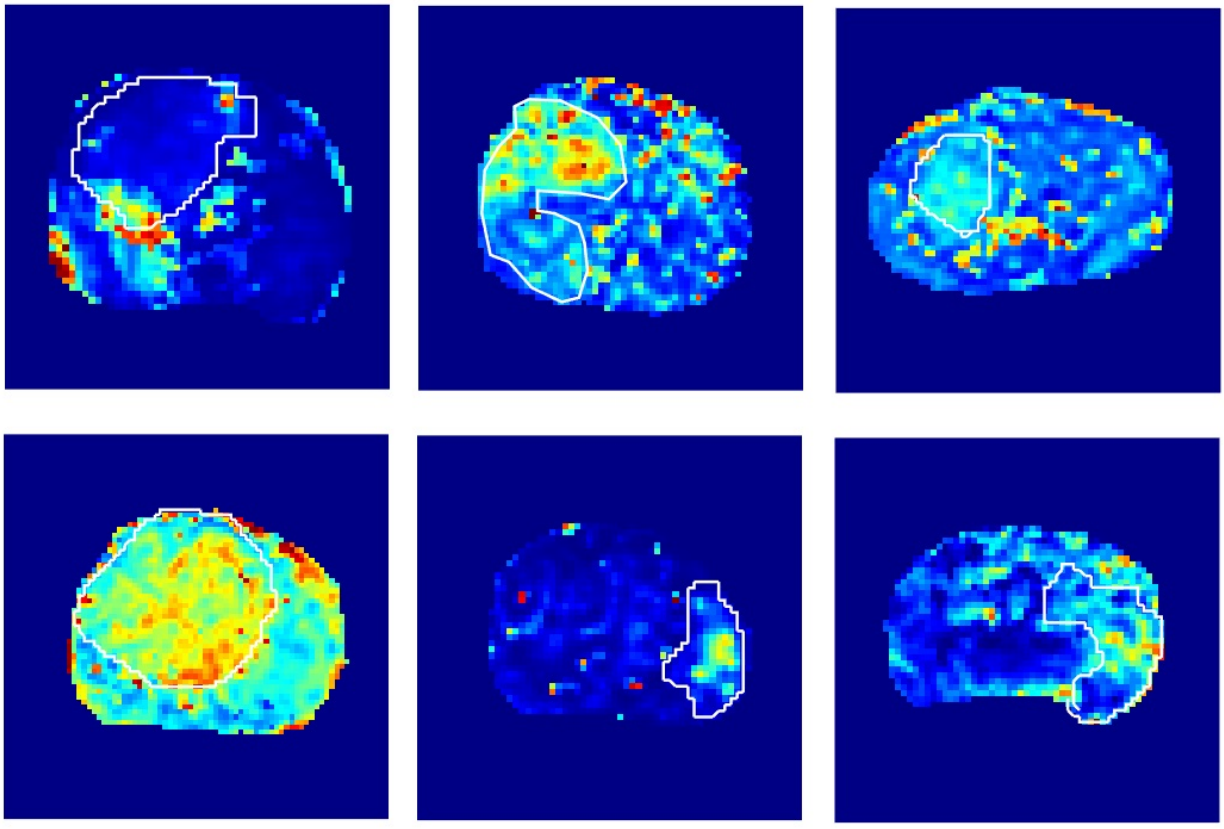

Figure 4.30: Cancer probability maps for six patients, based on the logistic regression of the Brix model parameters. The index tumor is delineated.

Figure 4.30 shows various success in terms of identifying the index tumor. For most of the patients the regression model estimates severe probability of cancer outside the primary tumor, and often in the peripheral zone of the prostate gland. The probability cutoff that gave the highest concordance between the probability maps and the location of the index tumor was a cancer probability of 14%. The Dice and Jaccard similarity coefficients between the location of the primary tumor, and the mask of the probability map generated with a cutoff of 14% are shown by histograms in figure 4.31.

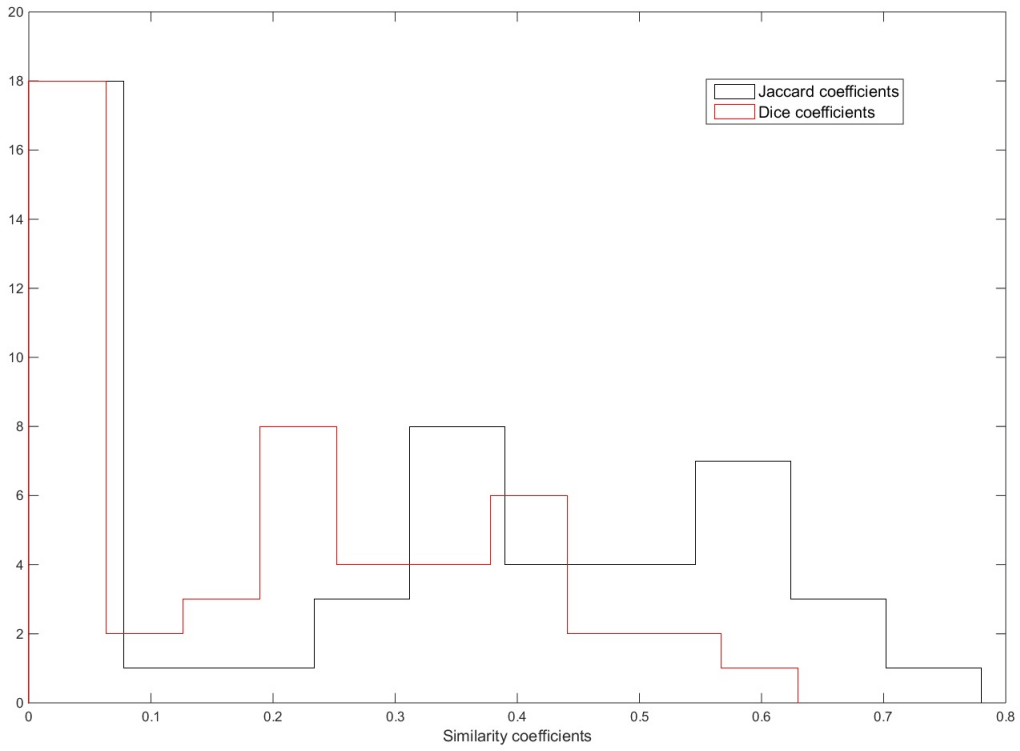

Figure 4.31: Dice- and Jaccard similarity coefficients between the mask of the probability maps and the location of the primary tumor in the first 50 patients. The Dice similarity coefficients (mean = 0.20, SD = 0.18) are shown in red, and the Jaccard similarity coefficients (mean = 0.30, SD = 0.25) are shown in black.

5. Discussion

5.1 Results of this study

In this study the relationship between clinical information, pathological parameters obtained from biopsies and prostatectomy specimens, and pretreatment DCE-MRI parameters for 79 prostate cancer patients has been examined. Particularly the relationship between DCE-MRI parameters and hypoxia has been investigated. Some of the challenges of accurately assessing the extent and aggressiveness of prostate cancer are apparent from table 4.2, where the linear correlations between several malignancy markers for prostate cancer in common clinical use are shown. This table shows no significant correlation between PSA and biopsy Gleason score or T-stage, and only a very weak correlation between PSA and D'Amico risk classification in the IV cohort. Additionally, no significant correlation is shown between Gleason score and T-stage, and the D'Amico risk classification correlates only moderatly to biopsy Gleason score, prostatectomy Gleason score in the IV cohort, and weakly to clinical T-stage and pathological T-stage. This shows the limitations of current methods of risk assessment and survival prediction of patients with prostate cancer, as none of the clinical risk assessment reliably predict cancer aggressiveness. Only two of the clinical parameters showed a significant correlation to the pimonidazole score. Largest tumor extent, and the pathological T-stage both showed moderate correlation to pimonidazole score, showing that larger tumors tends to be more hypoxic.

5.1.1 CA distribution

The uptake of CA within tumors varies largely between patients, and within tumors of the same patient. Figure 4.3 shows that the distribution of CA is severely heterogeneous in the tumors of both patient A and B. The same figure also shows that the two patients has a very different temporal pattern of CA uptake. Patient B, although it shows a fairly homogeneous concentration of CA in the early stages, by the time four minutes have passed, the distribution of the RSI is equally heterogeneous to that of patient A. This difference in CA behavior between patients is also illustrated in the cumulative distribution plots of the semi-quantitative parameters in figure 4.9. This illustrates the complexity of the CA behavior, both between patients, and within single tumors. Going back to figure 4.2, we see that the two voxels in patient A show a similar time required to reach the maximum, but the value of the maximum and the wash-out phase differs substantially. Patient B shows a similar wash-in phase, and wash-out gradient, but with different maximum uptake. These large intra-tumor differences in the RSI time-curves are reflected in the maps of the pharmacokinetic parameters. Figures 4.4 through 4.7 and 4.15 show the same tendencies in the maps of the semi-quantitative and Brix model parameters. This complexity of the contrast enhancement is, however, not reflected by the clinical parameters. Table 4.2 shows no significant linear correlation between the median values of any of the pharmacokinetic parameters and the clinical data, yet comparing only the median values might be too simplistic. As the clinical parameters are reported as a single number representing the entire tumor, it is not known *a priori* which voxel values to extract from a high resolution parameter image to find correlations. A percentile screening of the correlations between image parameters and pimonidazole score is shown in figures 4.28 and 4.29. Using this screening method allows for identifying the part of the parameter distribution with the highest predictive value, and a more nuanced indication of its robustness as a predictive parameter is achieved. Figures 4.28 and 4.29 show a band of significant, although relatively weak, correlations between the pimonidazole score and k_{el} at high percentiles. The oral cohort also showed

significant correlations between the iAUC and pimonidazole score, and between the k_{ep} and the pimonidazole score at low percentiles, but this cohort is relatively small ($n = 31$), and no equivalent result is seen in the IV cohort ($n = 48$). This result is in accordance with a finding by Borren *et al.*[8] who investigated the correlations between Gleason score, microvessel density (MVD), DCE-MRI parameters, and expression of HIF in whole mount prostate specimen. They reported no correlation between expression of HIF and MVD or DCE-MRI parameters($n = 15$). Similarly Gettman *et al.*[18] reported a lack of significance between MVD and PSA, Gleason grade or clinical and/or biochemical recurrence($n = 307$). Assuming the assumption that hypoxia is related to poor prognosis holds, these results raises a question on the relationship between vascular architecture, MVD, and hypoxia. A primary assumption when analyzing DCE-MRI data with respect to hypoxia is that there is a relationship between the presence of CA (blood), the presence of pimonidazole and the level of hypoxia. This relationship probably exists, but it may be more convoluted than initially thought. Several mechanisms, such as rate of oxygen metabolism and rate of pimonidazole metabolism, could affect the levels of hypoxia and the pimonidazole score without beeing reflected by the CA distribution.

5.1.2 Pharmacokinetic parameters

The correlations between the different pharmacokinetic parameters are shown in figure 4.19. This figure illuminates what the semi-quantitative parameters are reporting, in terms of the Brix model parameters. There is for example a strong correlation between the iAUC and the k_{ep}, indicating that a fast uptake of CA is related to what is assumed to be the transfer rate across the vascular membrane. There is also a strong negative correlation between slope of the wash-out curve and the k_{el}, indicating that the wash out curve is reporting on the elimination rate of CA from the plasma. These correlations are, however, expected, as the bi-exponential function (eq. 2.16) used to fit the model to the data are defining the parameters k_{ep}, and k_{el} in terms of the curve shape. Thus, a more interesting question is: Which physiological

traits are the Brix model parameters actually reflecting? The k_{el} is obviously reflecting the rate of elimination of CA from the voxel, yet this is not necessarily the same as the rate of elimination from the plasma compartment. Particularly under the assumption that $C_t = \nu_e C_e$ i.e. that the depicted voxel (unit volume) does not contain a vessel, this assumption requires a negligible transit time of the bolus through the capillary bed, i.e. the CA has to eliminate from the unit tissue at the same rate as the venous elimination from the plasma. However, considering the irregular blood perfusion through the tumor vasculature, there is reason to believe this assumption may be violated in some cases regarding solid tumors. Thus, k_{el} could contain information of capillary blood flow, and could also contain some information on the transfer rate from the EES to the plasma. The transfer rate across the capillary membrane is assumed described by k_{ep}, and is a function of the permeability of the capillary membrane, tissue density, and surface area of the membrane[34]. The Brix model assumes the transfer rates to be equal in both directions across the membrane, i.e. the permeability is assumed equal in both directions. If this assumption is not true, CA concentration in the plasma will not be correctly specified, and the response in the tissue may be erroneously estimated in the early stages of the infusion described by k_{ep}. The amplitude A is a parameter of the Brix model that is particularly difficult to intuitively comprehend. It has been reported to approximately correspond to the size of the EES[34], yet it also includes information on non-tissue specific parameters depending on the relaxation rate, and the infusion rate of CA, and scanner specific parameters such as TR. Additionally the amplitude contains information on the chemical components in the voxel depicted through the relaxation time $T1_0$. Hence its relation to underlying physiology is not clear.

The ambiguity in the interpretation of model parameters is an inevitable result of using a simple model to describe a complicated system. There is always a trade off between model complexity and the number of predictors that can be identified, with low bias or variance, from real data. A more complex model would require a larger data set(i.e. higher temporal resolu-

tion in the images), in order to ensure sufficient predictive performance.

The ultimate arbiter of cancer aggressiveness is survival. Investigating this requires long term follow up, with regular clinical examinations, and is beyond the scope of this thesis. However, other researchers have found correlations between Brix model parameters and clinical outcome of patients with cervical cancer[3]. In this regard, knowledge of the specific physiological trait that is described by the model parameters is not needed, and a simple model generally describing the main response of a complicated system suffices to assess the cancer aggressiveness once the statistical significance, and predictive power of the model is known. Fast influx of CA is a common criteria for differentiation between malignant and benign tissue in several different tissue types[24][29], including prostate cancer, and identifying the kinds of RSI time curves that corresponds to fast CA uptake (the type 3 curve shown in figure 4.2) can confidently be done from either semi-quantitative- or Brix model parameters. However, in this study the goal was to investigate the relationship between DCE-MRI parameters and hypoxia, to try to obtain a more exhaustive assessment of prostate cancer aggressiveness.

In this study an attempt was made at identifying the primary tumor using only the pharmacokinetic parameters from the Brix model through a logistic regression. Figures 4.30 and 4.31 shows that the logistic regression model was unable to identify the tumor, using only the Brix model parameters. The assumption that the tissue outside the primary tumor was normal tissue was a presumption for using this method. This is, however, debatable as metastasis are not reported in the MR images. Additionally, no information on prostatitis or benign hyper prostatic hyperplasia, which both are conditions with the potential of affecting the blood perfusion, are available. The technique of generating probability maps from a logistic regression model is, however, a useful way of creating multiparametric maps that can be compared to corresponding sections from the prostatectomy specimens. In order to make such a comparison, though, a corresponding map of the wanted outcomes is required.

5.2 Critical appraisal

5.2.1 Pimonidazole sections

The pimonidazole score reported is a measure of the fraction of the cancer cells that is shown to have a moderate to strong staining. Normal cells are in other words not included when the pimonidazole score is calculated. This means that the pimonidazole score is not a measure on the total tissue hypoxia, but a measure on the hypoxia of the cancer cells in the tissue. This represents a problem in regions where cancer cells and normal cells are intermixed, as the DCE-MRI doesn't have the ability to make the differentiation between normal and cancerous cells, but rather reflects the blood perfusion independent of tissue type, and its constituent cells. Another challenge when comparing the pharmacokinetic parameters to the pimonidazole score is the absence of spatial resolution in the scoring system. The pimonidazole sections show significant heterogeneity in terms of staining, and sections with low pimonidazole score may contain regions of severely high degrees of hypoxia. Examples of different sections with the same pimonidazole score are shown in figure 5.1. This figure shows four patients with different staining patterns, all with pimonidazole score = 2.5. The tumors can either be composed of small areas showing a large degree of staining, as in patient B, large areas showing moderate degrees of staining, as in patient D, or something in between, as in patient A. These differences in pimonidazole staining patterns are not reflected in the pimonidazole score, as the intra-tumor heterogeneity is not reported.

Comparing absolute values of the pharmacokinetic parameters to a pimonidazole score obtained by the fraction of cancer cells with moderate or high levels of hypoxia may be a comparison under a false analogy, as the heterogeneity of both the maps of the pharmacokinetic parameters and the pimonidazole sections gives reason to doubt whether a measure on the global distribution of hypoxia is reflected in local tissue properties, assessed by the pharmacokinetic parameters.

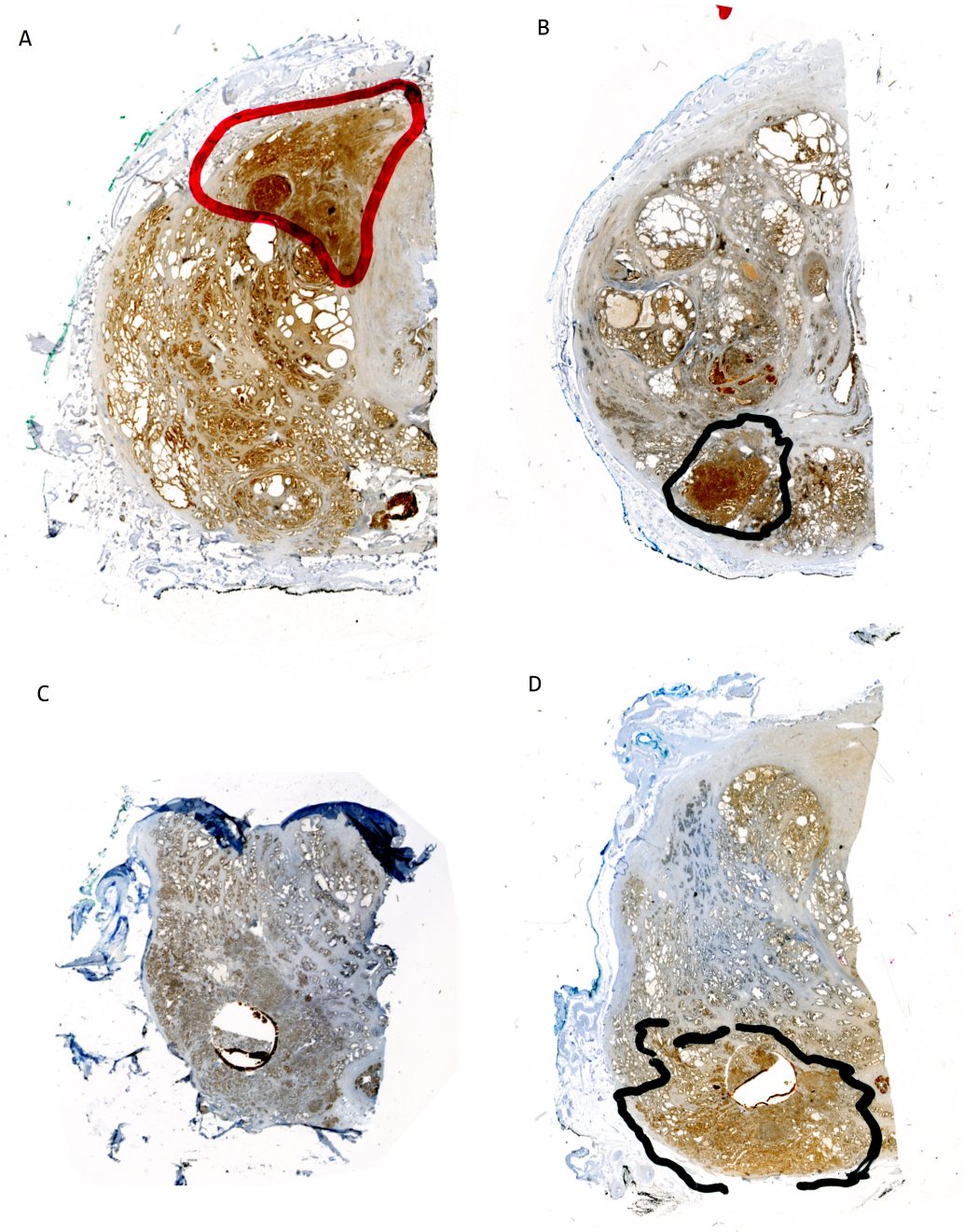

Figure 5.1: Examples of immunostained prostatectomy samples. All the sections in this figure are reported as pimonidazole score = 2.5. Note that the marked lines in the images are not necessarily concordant with the primary tumor.

5.2.2 Determining the time of arrival of CA

The images obtained in this study are acquired at a temporal resolution of four images per minute. Comparing this resolution to a typical heart rate of 60 beats per minute, this means that the sampling resolution of the MRI is insufficient to detect the pulsatile flow of the blood. This poses a problem when determining the time of arrival of the CA in the images. The time of arrival of the CA can not be unambiguously defined in terms of picture frame number, introducing an uncertainty in the determination of S_0. In one of the 30 patients used for controlling the threshold which determined the arrival of CA, the routine disagreed with the manual inspections of the images, introducing an error of approximately 6% in the estimation of S_0(the exact error varies a bit from voxel to voxel). This error is however small compared to the noise in the pre-contrast images of the same patient, lying in the range $18\% - 20\%$, and the routine was deemed acceptably robust to handle the rest of the patients.

5.2.3 Why s_{res} and not R^2?

In the field of pharmacological and biochemical research it appears to be common practice to use the coefficient of determination R^2 when determining the goodness of fit, even for non-linear models[32]. This is however problematic, as using the R^2 as a measure of the proportion of the data being explained by the model implicitly assumes that the sum of square errors adds up in a particular manner. The coefficient of determination is defined according to equation 5.1:

$$R^2 = \frac{\sum_{i=1}^{n}(\hat{y}_i - \bar{y})^2}{\sum_{i=1}^{n}(y_i - \bar{y})^2} = 1 - \frac{\sum_{i=1}^{n}(y_i - \hat{y}_i)^2}{\sum_{i=1}^{n}(y_i - \bar{y})^2} \tag{5.1}$$

Where y_i are the measured data, $\hat{y}_i$ are the model-estimated data, and $\bar{y}$ is the mean of the n datapoints. This definition assumes that the model sum of squares ($MSS = \sum_{i=1}^{n}(\hat{y}_i - \bar{y})^2$) and the residual sum of squares $RSS = \sum_{i=1}^{n}(y_i - \hat{y}_i)^2$) adds up to the total sum of squares $TSS = \sum_{i=1}^{n}(y_i - \bar{y})^2$),

which is not generally the case for non-linear models. This means that R^2 is not confined between 0 and 1, making it less intuitive to interpret, and possibly confound or mislead a reader who is used to interpreting it as the proportion of the total variability in the outcomes that is accounted for by the predictors. In a paper by Spiess *et al.*, where Monte Carlo simulations were used to examine the validity of the coefficient of determination in non-linear regression, R^2 was concluded to poorly represent the performance of a non-linear regression model, and was found to rarely be affected more than in the third or fourth decimal place, even in scenarios with highly inferior models[32].

5.2.4 Comments on the Brix model

In this study the Brix model (eq. (2.16)) was used to analyze the MR images, and obtain physiological parameters. Brix's solution can be shown to be a reduced form of a general solution of the system of equations for a two-compartment model[40]. The general solution has the form:

$$\begin{bmatrix} C_p \\ C_e \end{bmatrix} = \frac{K_{in}}{V_p(\lambda_1 - \lambda_2)} \left(\begin{bmatrix} \lambda_1 + k_{21} \\ V_p k_{12}/V_e \end{bmatrix} \frac{e^{-\lambda_1 t'} - 1}{-\lambda_1} e^{\lambda_1 t} - \begin{bmatrix} \lambda_2 + k_{21} \\ V_p k_{12}/V_e \end{bmatrix} \frac{e^{-\lambda_2 t'} - 1}{-\lambda_2} e^{\lambda_2 t} \right) \tag{5.2}$$

where subscript p stands for the plasma compartment, and subscript e stands for the EES. λ_1 and λ_2 are eigenvalues of the parametric matrix. As before $t' = t$ when $0 < t \leq \tau$, and $t' = \tau$ when $t > \tau$, where τ is the duration of the CA injection. Under the assumption that the transfer velocities were equal in both directions between the plasma and the EES, and that $V_p >> V_e$, the eigenvalues are reduced to $\lambda_1 = -k_{el}$ and $\lambda_2 = -k_{ep}$, giving eq. 2.15. The eigenvalue $\lambda_2 = -k_{ep}$ implies that the AIF (C_p) is assumed to be mono-exponential for a bolus injection of CA, as the term $\lambda_2 + k_{ep} = 0$. Thus the model does not take into account the effect of the EES concentration of CA on the elimination rate from the plasma. Whether this has severe implications

on the validity of the model or not is probably somewhat dependent on the tissue characteristics, but Yang *et al.*[40] advocates the importance of keeping the k_{12} term in the model, and rather make the assumption $k_{ep} >> k_{el}$ and $k_{12} >> k_{el}$, which they argue is more realistic. Including a fourth parameter is, however, increasing the risk of over fitting the model, and would require more data to ensure sufficient predictive performance. Thus exploring a model with a separation between the transfer rates across the capillary wall is not feasible with the current data with limited temporal resolution, and limited number of data points.

6. Conclusion and further work

Through this work there has been shown no convincing correlation between the DCE-MRI data and clinical parameters obtained from preoperative tests, biopsies or prostatectomy specimens. The reasons for this can be many, including some discrepancy between the way in which the clinical data, and the DCE-MRI analysis are reported. Extracting pathological information on a tumor directly from pharmacokinetic parameters alone is difficult, as the parameters generally reflects many different aspects of the tumor physiology, and often reflects parts of the same physiological trait. Thus correlation studies are a useful way of assessing the diagnostic potential of the parameters. The lack of correlations between the DCE-MRI data and, particularly, the pimonidazole staining in this study does not, however, imply that assessement of hypoxia by DCE-MRI as a potential biomarker for prostate cancer is impossible. This work could benefit from extensions in a number of ways. For example the comparison between the pharmacokinetic parameters and the pimonidazole sections could be done in a more refined way.

A potentially more comprehensive comparison could be done by scoring the pimonidazole sections in terms of their level of staining, rather than the fraction of the area that shows high staining. Either by perfoming a histogram-analysis of e.g. the red channel in the digital images of the sections, where a correlation screening of the red channel intensity percentiles can be performed against the parametric maps. Or even better, by mapping the pixels in the images of the sections to the corresponding voxels in the DCE-MR images to obtain high spatial resolution on the hypoxia measurement. Knowing the spatial resolution of the hypoxia levels would allow for an analysis similar

to the logistic regression analysis performed on the Brix model parameters in this study, but with a map of the hypoxic regions of the tumor as a basis for the outcome against which the regression is made. This would ensure a more one to one comparison between the parametric maps and the pimonidazole sections, and result in a higher specificity of the analysis.

Bibliography

[1] A. R. Alberts, I. G. Schoots, and M. J. Roobol. Prostate-specific antigen-based prostate cancer screening: Past and future. *Int. J. Urol.*, 22(6):524–532, Jun 2015.

[2] Bruce Alberts. *Molecular biology of the cell*. Garland Science, New York, 2008.

[3] E. K. Andersen, K. H. Hole, K. V. Lund, K. Sundf?r, G. B. Kristensen, H. Lyng, and E. Malinen. Pharmacokinetic parameters derived from dynamic contrast enhanced MRI of cervical cancers predict chemoradiotherapy outcome. *Radiother Oncol*, 107(1):117–122, Apr 2013.

[4] R. Arora, M. O. Koch, J. N. Eble, T. M. Ulbright, L. Li, and L. Cheng. Heterogeneity of Gleason grade in multifocal adenocarcinoma of the prostate. *Cancer*, 100(11):2362–2366, Jun 2004.

[5] S. L. Barnes, J. G. Whisenant, M. E. Loveless, and T. E. Yankeelov. Practical dynamic contrast enhanced MRI in small animal models of cancer: data acquisition, data analysis, and interpretation. *Pharmaceutics*, 4(3):442–478, 2012.

[6] Atle Bjørnerud. *The Physics of Magnetic Resonance Imaging*. Compendium, FYS-KJM4740, Department of physics, University of Oslo.

[7] Mary Boas. *Mathematical methods in the physical sciences*. Wiley, Hoboken, NJ, 2006.

[8] A. Borren, G. Groenendaal, P. van der Groep, M. R. Moman, A. E. Boeken Kruger, U. A. van der Heide, T. N. Jonges, P. J. van Diest, M. van Vulpen, and M. E. Philippens. Expression of hypoxia-inducible factor-1Î± and -2Î± in whole-mount prostate histology: relation with dynamic contrast-enhanced MRI and Gleason score. *Oncol. Rep.*, 29(6):2249–2254, Jun 2013.

[9] L. K. Boyd, X. Mao, and Y. J. Lu. The complexity of prostate cancer: genomic alterations and heterogeneity. *Nat Rev Urol*, 9(11):652–664, Nov 2012.

[10] G. Brix, W. Semmler, R. Port, L. R. Schad, G. Layer, and W. J. Lorenz. Pharmacokinetic parameters in CNS Gd-DTPA enhanced MR imaging. *J Comput Assist Tomogr*, 15(4):621–628, 1991.

[11] Y. J. Chen, W. C. Chu, Y. S. Pu, S. C. Chueh, C. T. Shun, and W. Y. Tseng. Washout gradient in dynamic contrast-enhanced MRI is associated with tumor aggressiveness of prostate cancer. *J Magn Reson Imaging*, 36(4):912–919, Oct 2012.

[12] M. P. Chung, D. Margolis, S. Mesko, J. Wang, P. Kupelian, and M. Kamrava. Correlation of quantitative diffusion-weighted and dynamic contrast-enhanced MRI parameters with prognostic factors in prostate cancer. *J Med Imaging Radiat Oncol*, 58(5):588–594, Oct 2014.

[13] C. A. Cuenod and D. Balvay. Perfusion and vascular permeability: basic concepts and measurement in DCE-CT and DCE-MRI. *Diagn Interv Imaging*, 94(12):1187–1204, Dec 2013.

[14] J. E. Damber and G. Aus. Prostate cancer. *Lancet*, 371(9625):1710–1721, May 2008.

[15] A. V. D'Amico, R. Whittington, S. B. Malkowicz, D. Schultz, K. Blank, G. A. Broderick, J. E. Tomaszewski, A. A. Renshaw, I. Kaplan, C. J. Beard, and A. Wein. Biochemical outcome after radical prostatectomy, external beam radiation therapy, or interstitial radiation therapy for clinically localized prostate cancer. *JAMA*, 280(11):969–974, Sep 1998.

[16] J. Folkman and R. Kalluri. Cancer without disease. *Nature*, 427(6977):787, Feb 2004.

[17] Jon-Vidar Gaustad. *Blood supply in human melanoma xenografts assessed by DCE-MRI and intravital microscopy*. PhD thesis, University of Oslo, 2009. unpublished thesis.

[18] M. T. Gettman, E. J. Bergstralh, M. Blute, H. Zincke, and D. G. Bostwick. Prediction of patient outcome in pathologic stage T2 adenocarcinoma of the prostate: lack of significance for microvessel density analysis. *Urology*, 51(1):79–85, Jan 1998.

[19] David Griffiths. *Introduction to quantum mechanics*. Pearson Prentice Hall, Upper Saddle River, NJ, 2005.

[20] Eric Hall. *Radiobiology for the radiologist*. Wolters Kluwer Health/Lippincott Williams & Wilkins, Philadelphia, 2012.

[21] A. Heidenreich, J. Bellmunt, M. Bolla, S. Joniau, M. Mason, V. Matveev, N. Mottet, H. P. Schmid, T. van der Kwast, T. Wiegel, and F. Zattoni. [EAU guidelines on prostate cancer. Part I: screening, diagnosis, and treatment of clinically localised disease]. *Actas Urol Esp*, 35(9):501–514, Oct 2011.

[22] D. J. Hernandez, M. E. Nielsen, M. Han, and A. W. Partin. Contemporary evaluation of the D'amico risk classification of prostate cancer. *Urology*, 70(5):931–935, Nov 2007.

[23] E. Hernes, A. Kyrdalen, R. Kvale, E. Hem, O. Klepp, K. Axcrona, and S. D. Fossa. Initial management of prostate cancer: first year experience with the Norwegian National Prostate Cancer Registry. *BJU Int.*, 105(6):805–811, Mar 2010.

[24] U. Hoffmann, G. Brix, M. V. Knopp, T. Hess, and W. J. Lorenz. Pharmacokinetic mapping of the breast: a new method for dynamic MR mammography. *Magn Reson Med*, 33(4):506–514, Apr 1995.

[25] Knut Håkon Hole. *Magnetic resonance guidance for the multidisciplinary management of pelvic malignancies.* PhD thesis, University of Oslo, 2015. unpublished thesis.

[26] Tord Hompland. *Functional magnetic resonance imaging of the microenvironment-associated metastatic potential of tumors.* PhD thesis, University of Oslo, 2013. unpublished thesis.

[27] R. Kvåle, B. M?ller, R. Wahlqvist, S. D. Fossa, A. Berner, C. Busch, A. E. Kyrdalen, A. Svindland, T. Viset, and O. J. Halvorsen. Concordance between Gleason scores of needle biopsies and radical prostatectomy specimens: a population-based study. *BJU Int.*, 103(12):1647–1654, Jun 2009.

[28] oncolex.no. Prostatakreft http://oncolex.no/prostata, 2016.

[29] A. E. Othman, F. Falkner, J. Weiss, S. Kruck, R. Grimm, P. Martirosian, K. Nikolaou, and M. Notohamiprodjo. Effect of Temporal Resolution on Diagnostic Performance of Dynamic Contrast-Enhanced Magnetic Resonance Imaging of the Prostate. *Invest Radiol*, 51(5):290–296, May 2016.

[30] H. B. Ragnum, L. Vlatkovic, A. K. Lie, K. Axcrona, C. H. Julin, K. M. Frikstad, K. H. Hole, T. Seierstad, and H. Lyng. The tumour hypoxia marker pimonidazole reflects a transcriptional programme associated with aggressive prostate cancer. *Br. J. Cancer*, 112(2):382–390, Jan 2015.

[31] G. Sauter, S. Steurer, T. S. Clauditz, T. Krech, C. Wittmer, F. Lutz, M. Lennartz, T. Janssen, N. Hakimi, R. Simon, M. von Petersdorff-Campen, F. Jacobsen, K. von Loga, W. Wilczak, S. Minner, M. C. Tsourlakis, V. Chirico, A. Haese, H. Heinzer, B. Beyer, M. Graefen, U. Michl, G. Salomon, T. Steuber, L. H. Budaus, E. Hekeler, J. Malsy-Mink, S. Kutzera, C. Fraune, C. Gobel, H. Huland, and T. Schlomm. Clinical Utility of Quantitative Gleason Grading in Prostate Biopsies and Prostatectomy Specimens. *Eur. Urol.*, 69(4):592–598, Apr 2016.

[32] A. N. Spiess and N. Neumeyer. An evaluation of R2 as an inadequate measure for nonlinear models in pharmacological and biochemical research: a Monte Carlo approach. *BMC Pharmacol.*, 10:6, 2010.

[33] U. Stenman, J. Leinonen, W. Zhang, and P. Finne. Prostate-specific antigen. *seminars in cancer biology*, 9(2):83–93, Apr 1999.

[34] P. S. Tofts. Modeling tracer kinetics in dynamic Gd-DTPA MR imaging. *J Magn Reson Imaging*, 7(1):91–101, 1997.

[35] P. S. Tofts, G. Brix, D. L. Buckley, J. L. Evelhoch, E. Henderson, M. V. Knopp, H. B. Larsson, T. Y. Lee, N. A. Mayr, G. J. Parker, R. E. Port, J. Taylor, and R. M. Weisskoff. Estimating kinetic parameters from dynamic contrast-enhanced T(1)-weighted MRI of a diffusable tracer: standardized quantities and symbols. *J Magn Reson Imaging*, 10(3):223–232, Sep 1999.

[36] P. Vaupel. Tumor microenvironmental physiology and its implications for radiation oncology. *Semin Radiat Oncol*, 14(3):198–206, Jul 2004.

[37] S. Walker-Samuel, M. O. Leach, and D. J. Collins. Evaluation of response to treatment using DCE-MRI: the relationship between initial area under the gadolinium curve (IAUGC) and quantitative pharmacokinetic analysis. *Phys Med Biol*, 51(14):3593–3602, Jul 2006.

[38] Steve Webb. *Webb's physics of medical imaging*. Taylor & Francis, Boca Raton, 2012.

[39] www.kreftregisteret.no. Kreftregisteret https://www.kreftregisteret.no/generelt/fakta-om-kreft-test/, 2016.

[40] X. Yang, J. Liang, P. Schmalbrock, and M. V. Knopp. Pharmacokinetic modeling of DCE-MRI data with arterial input function. *Proc. Intl. Soc. Mag. Reson. Med*, 15, 2007.

[41] Y. L. Yang, J. Y. Chu, and M. R. Wang. [Tumor genetic heterogeneity]. *Yi Chuan*, 35(1):1–9, Jan 2013.

[42] T. E. Yankeelov and J. C. Gore. Dynamic Contrast Enhanced Magnetic Resonance Imaging in Oncology: Theory, Data Acquisition, Analysis, and Examples. *Curr Med Imaging Rev*, 3(2):91–107, May 2009.

A. Appendix

A.1 Statistical plots

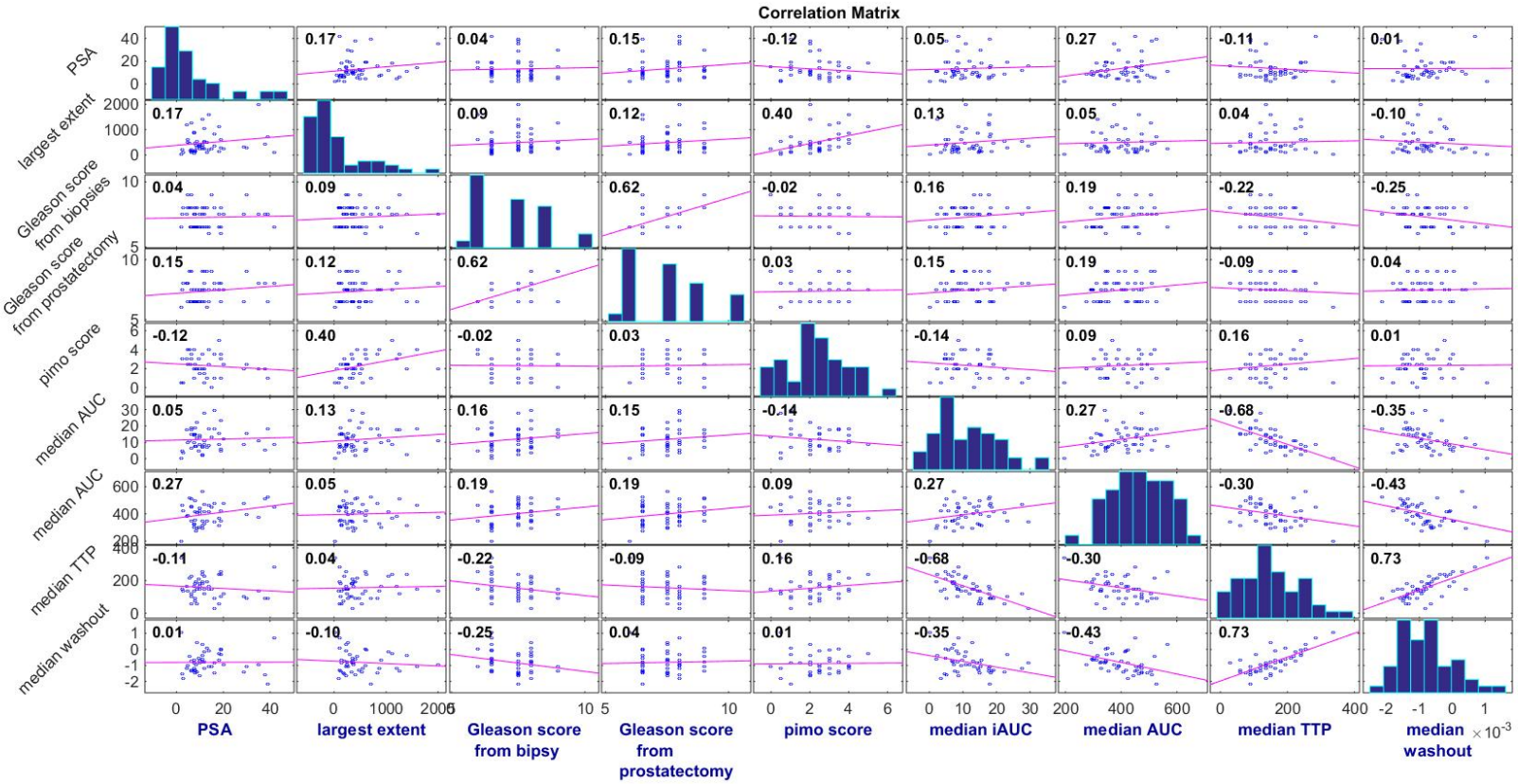

Figure A.1: Scatterplot matrix of correlations between the clinical data and the semiquantitative parameters in the IV cohort. The Pearson correlation coefficient is displayed in the upper left corner of the plots, and the diagonal shows the distributions of the parameters.

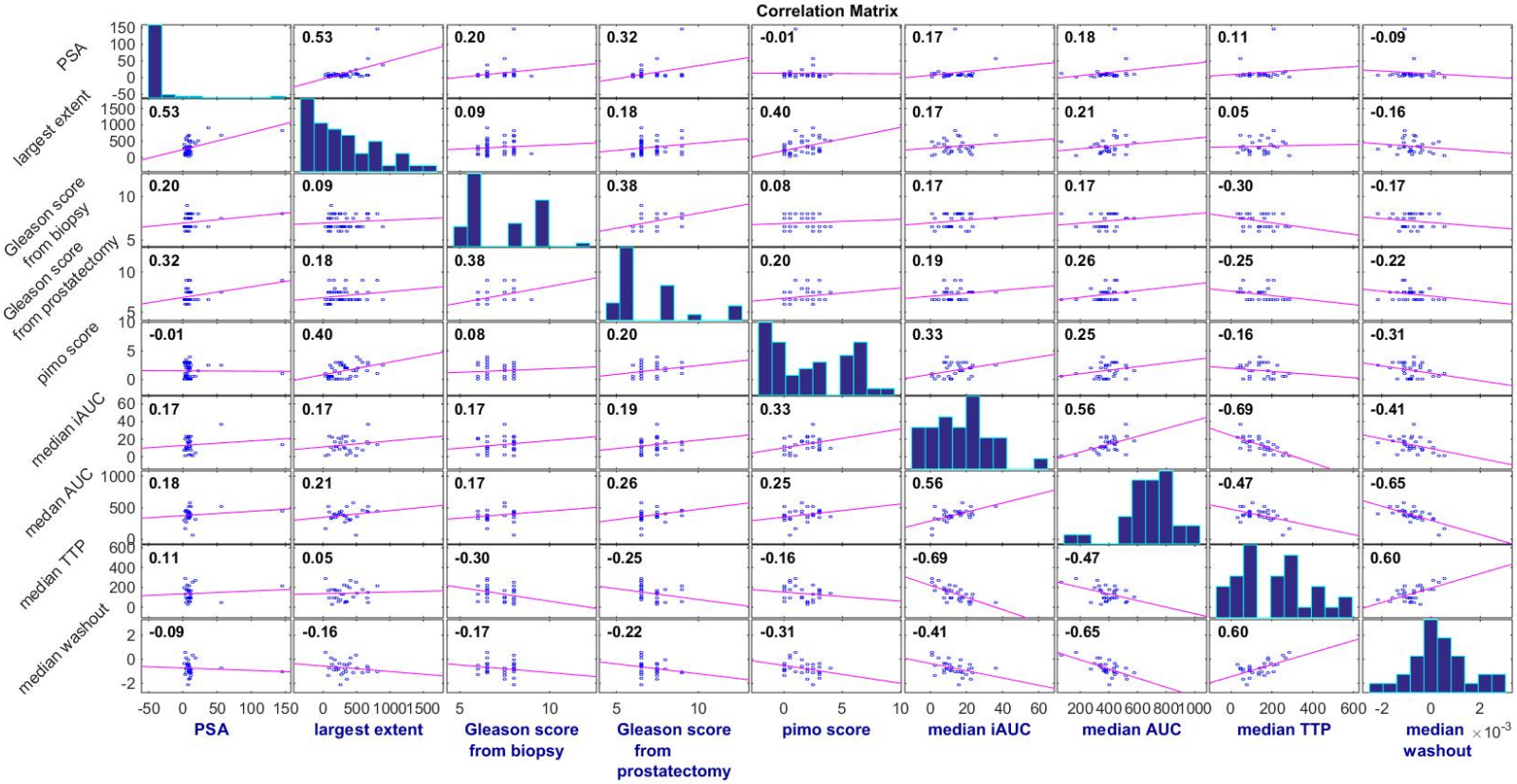

Figure A.2: Scatterplot matrix of correlations between the clinical data and the semiquantitative parameters in the oral cohort. The Pearson correlation coefficient is displayed in the upper left corner of the plots, and the diagonal shows the distributions of the parameters.

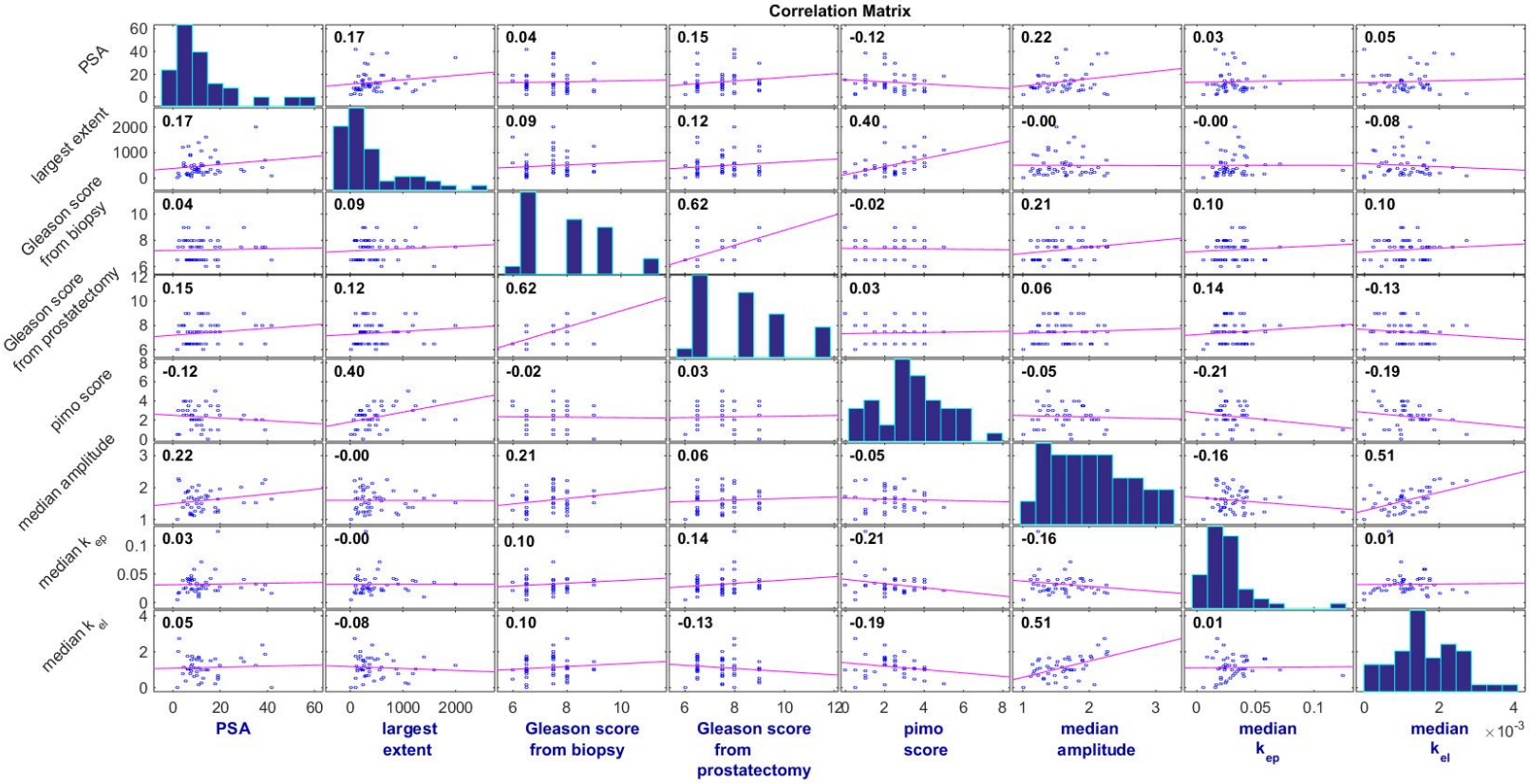

Figure A.3: Scatterplot matrix of correlations between the clinical data and the Brix model parameters in the IV cohort. The Pearson correlation coefficient is displayed in the upper left corner of the plots, and the diagonal shows the distributions of the parameters.

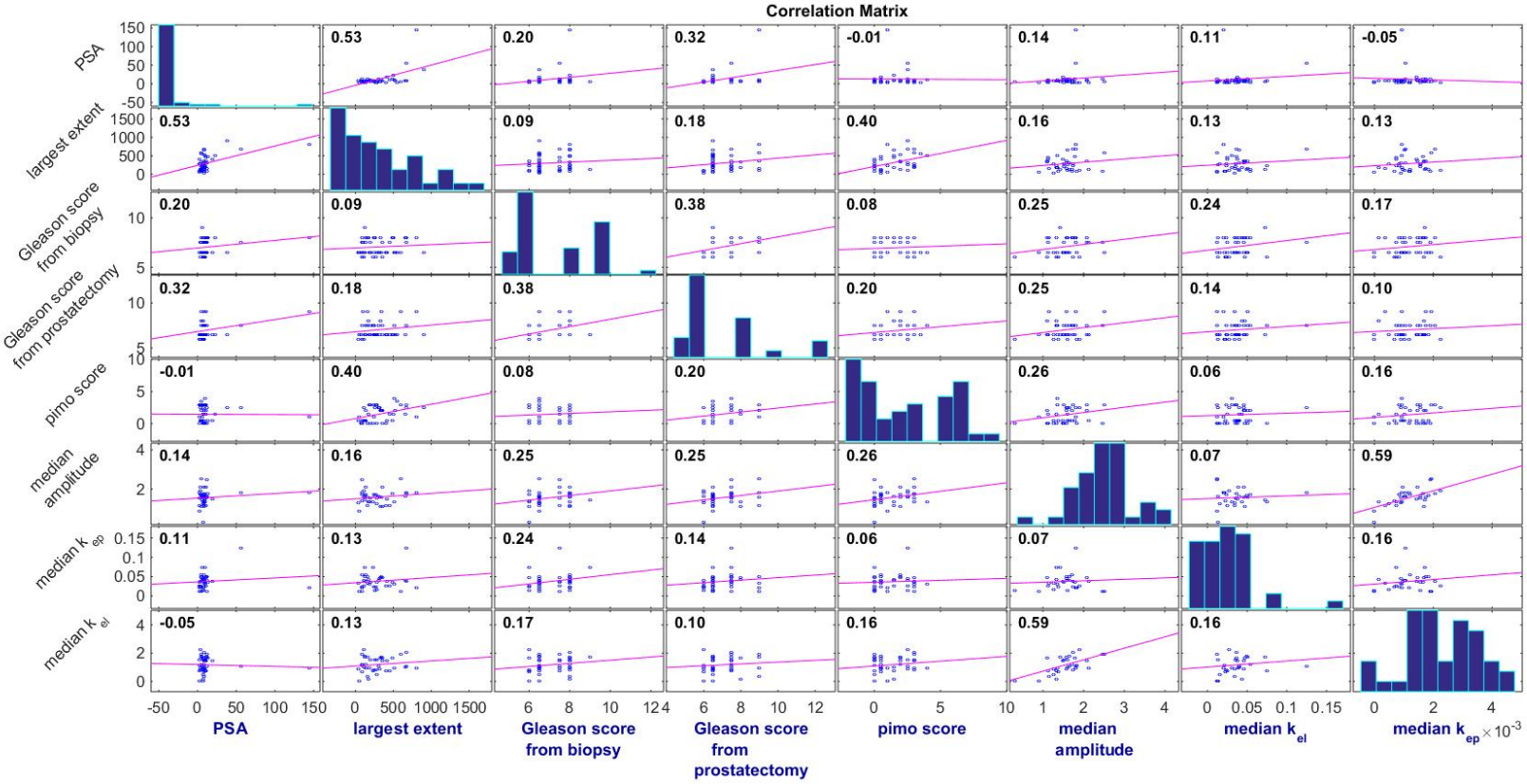

Figure A.4: Scatterplot matrix of correlations between the clinical data and the Brix model parameters in the oral cohort. The Pearson correlation coefficient is displayed in the upper left corner of the plots, and the diagonal shows the distributions of the parameters.

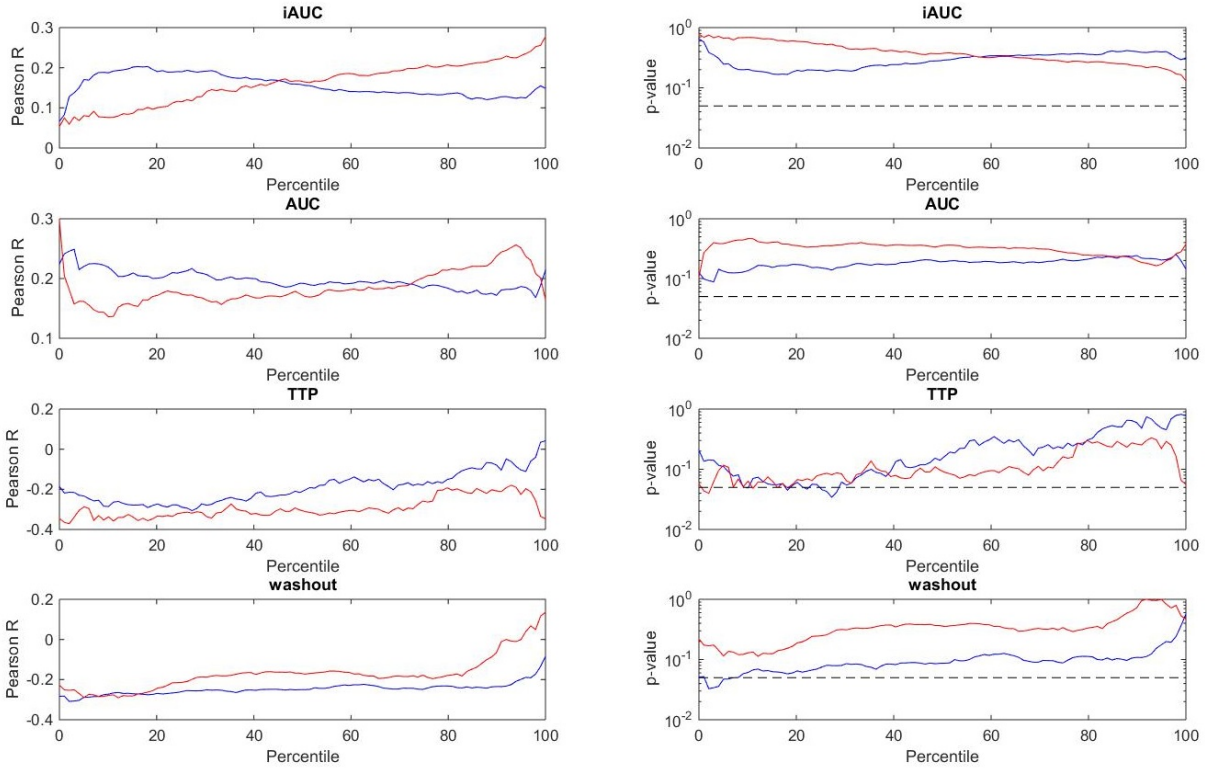

Figure A.5: Percentile screening of the correlation between the semiquantitative parameters and Gleason score from biopsies. The IV cohort is shown in blue, and the oral cohort is shown in red. The right column shows the Pearson R-coefficients, and the left column shows the p-values. The stapled black line is the $p = 0.05$ significance line.

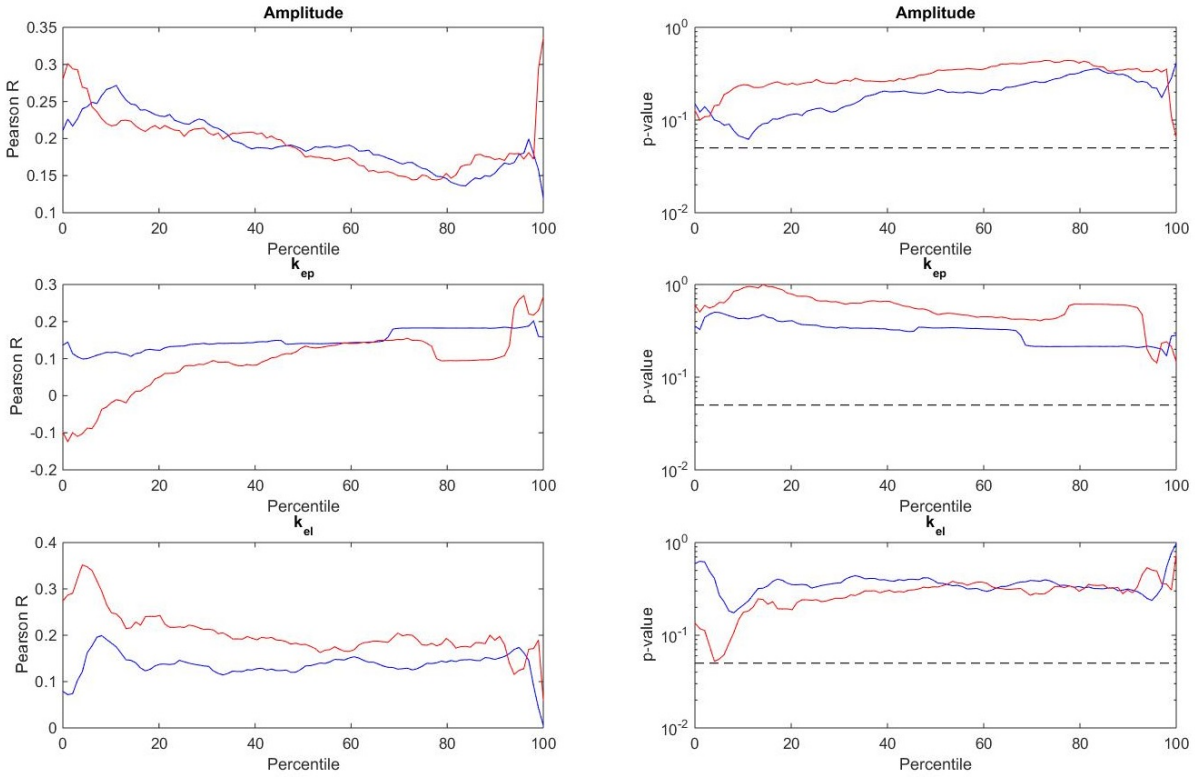

Figure A.6: Percentile screening of the correlation between the Brix model parameters and Gleason score from biopsies. The IV cohort is shown in blue, and the oral cohort is shown in red. The right column shows the Pearson R-coefficients, and the left column shows the p-values. The stapled black line is the $p = 0.05$ significance line.

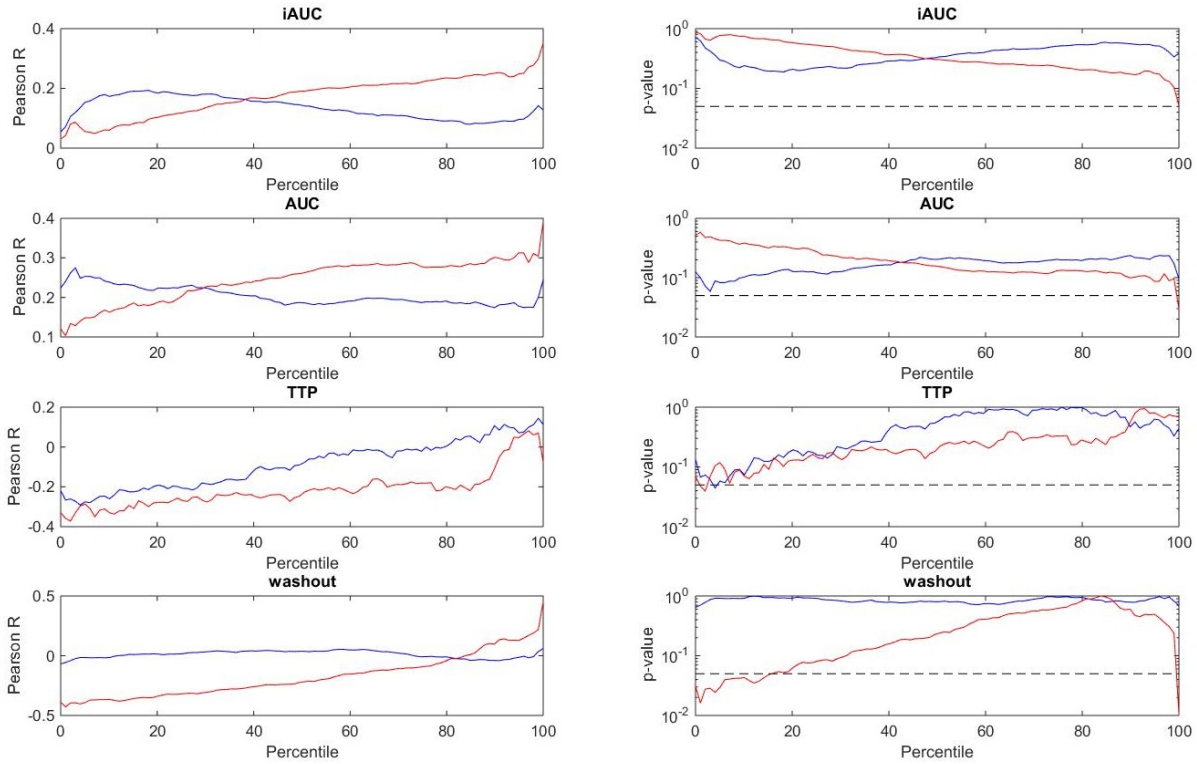

Figure A.7: Percentile screening of the correlation between the semiquantitative parameters and Gleason score from prostatectomy specimens. The IV cohort is shown in blue, and the oral cohort is shown in red. The right column shows the Pearson R-coefficients, and the left column shows the p-values. The stapled black line is the $p = 0.05$ significance line.

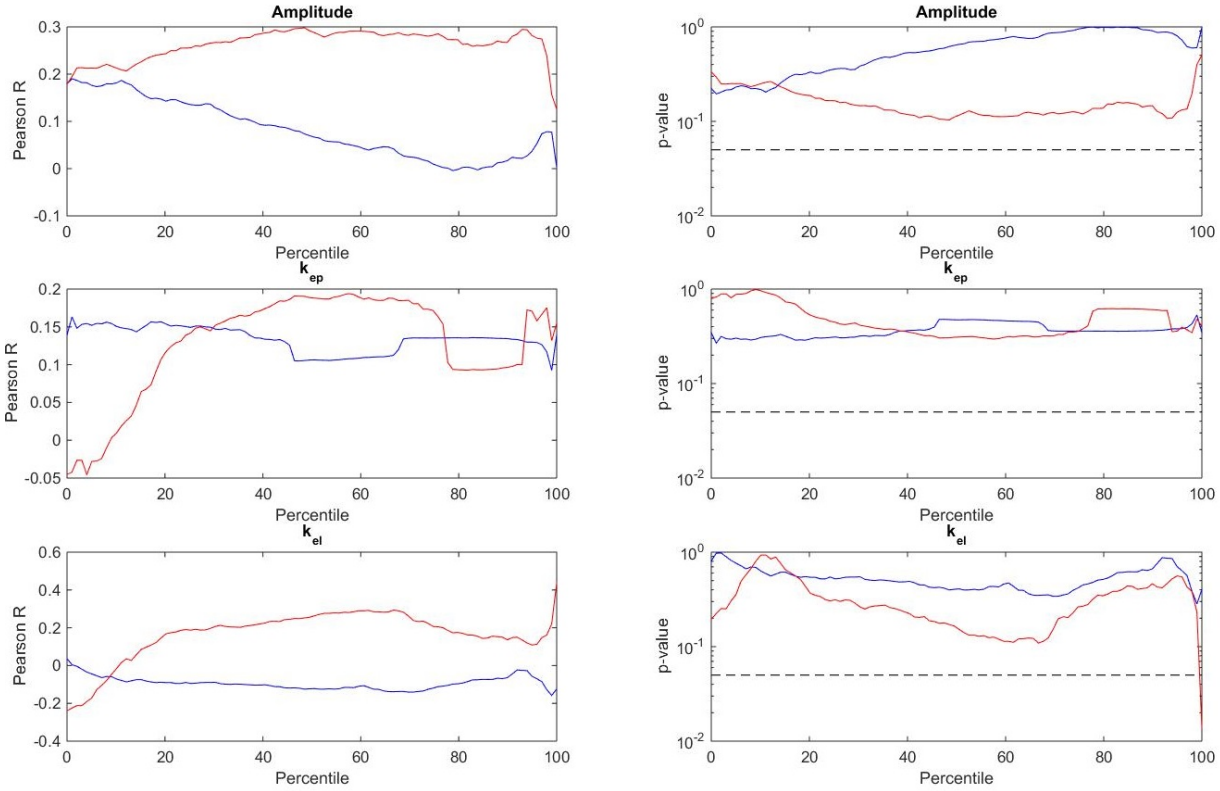

Figure A.8: Percentile screening of the correlation between the Brix model parameters and Gleason score from prostatectomy specimens. The IV cohort is shown in blue, and the oral cohort is shown in red. The right column shows the Pearson R-coefficients, and the left column shows the p-values. The stapled black line is the $p = 0.05$ significance line.

A.2 Computer routines developed in this study

```
% A routine for extracting and sorting the images from the patient folders.
% The region of interest .txt file is located in the same folder,
% and includesthe slice number in which the tumor is drawn.
%This script extracts all the images in the folder that depicts
%this slice, as well as the roi.


clear
omit = [20 34 35 51 53 58 63 64 65 66 67 68 69 72 81 84 88 91 92 ...
    93 94 96 98 99 101 103 105 107 108 109 110 111 112];
for i = 1:110
    %Enter the folder of patient i:
    path = sprintf('C:\\FuncProst\\Patient%03d',i);
    try
        cd(path)
    catch
        continue
    end

    %Find the filenames of the images in the folder.
    %The names of the image-files differs somewhat from patient
    %to patient, but they all contain a number in the title. This number is
    %used by the function sort_nat to sort the files in ascending order
    %according to this number:

    if any(i==omit) == 0;
        files = dir('*.dcm');
        cd('C:\\FuncProst\\Kode')
        name = {files.name};
        fileNames = sort_nat(name);
        numIm = length(fileNames);

        cd(path)
```

```
    %Extract the images from the file, and stores them in the variable
    %IM:
    IM = zeros(256,256,numIm);
    for k = 1:numIm
        fileName = char(fileNames(k));
        IM(:,:,k) = dicomread(fileName);
    end

    %Import the roi from the folder, and extract the number of the
    %slice to be examined:
    roi = dir('*.roi');
    str = roi.name;
    roi = importdata(str);

    try
        Roi = roi.data./3.0;
    catch
        Roi = roi./3.0;
    end

    %Extract the slice number from the roi filename:
    try
        Slice = str2double(str(length(str)-5:length(str)-4));
        assert(~isnan(Slice))
    catch
        Slice = str2double(str(length(str)-4));
    end

    %Pick out the images of the relevant slice from IM:
    for k = 1:30                % # of timesteps is 30
        ImSlice(:,:,k) = IM(:,:,(k-1)*length(IM)/30+Slice);
    end

    slice(i) = Slice;
    ROI(i) = {Roi};
    patients(i) = {ImSlice};
    clearvars ImSlice Roi Slice
end
```

```
end



clearvars -except omit slice ROI patients
cd('C:\\FuncProst\\Kode')

%This part determines the frame in which the CA arrives in the image, using
%the function start_frame:
firstFrames = zeros(1,length(patients));
for i = 1:length(patients)
    if any(i==omit) == 0;
        firstFrames(i) = start_frame(patients{i});
    end
end


%Calculating the relative signal increase for each voxel, at each time
%point, and storing them in a structure called RSI.

RSI = cell(1,length(patients));
RSI_int = cell(1,length(patients));

for k = 1:length(patients)
    ims = patients{k};
    patient = patients{k};
    pre_cont = patient(:,:,1:firstFrames(k)-1);
    s_temp = zeros(size(pre_cont,1));

    %create an s0 image as the average of the pre-contrast images.
    for i = 1:size(pre_cont,3)
        s_temp = s_temp+pre_cont(:,:,i);
    end
    s0 = s_temp./size(pre_cont,3);
    clearvars s_temp

    %calculating the RSI, and setting s0 to one where it is zero, to avoid
    %diverging values for the RSI.
    rsi = zeros(size(s0,1),size(s0,2),size(ims,3));
```

```
    for i = 1:size(s0,1)
      for j = 1:size(s0,2)
          try
        if s0(i,j) ~= 0
         rsi(i,j,:) = (squeeze(patient(i,j,:))-s0(i,j))./s0(i,j);
        else
         rsi(i,j,:) = (squeeze(patient(i,j,:))-1);
        end
          catch
              continue
          end
      end
    end
    try
    RSI(k) = {rsi};      %regular RSI, containing all time-points
    RSI_int(k) = {rsi(:,:,firstFrames(k):end)}; %interpolated RSI
    catch
        continue
    end
end

% This next part calculates the semi-quantitative parameters from the
% interpolated rsi. The parameters are calculated only within the index
% tumor. The parameters are stored in a cell structure called semiquant

for k = 1:length(patients)
    roi = cell2mat(ROI(k));
    rsi = cell2mat(RSI_int(k));
    AUC = zeros(size(rsi,1));
    ttp = zeros(size(rsi,1));
    iAUC = zeros(size(rsi,1));
    washout = zeros(size(rsi,1));
    L = size(rsi,3);
    time = linspace(0,15*(L-1),L);    %Creating the standard time vector
    try
    %Create a mask of the index tumor
    bw = roipoly(patient(:,:,slice(k)),roi(:,1),roi(:,2));
    for i = 1:size(rsi,1)
        for j = 1:size(rsi,2);
```

```
            if bw(i,j) == 1
                RSI = squeeze(rsi(i,j,:));
                AUC(i,j) = trapz(time(1:(30-max(firstFrames))), ...
                    RSI(1:(30-max(firstFrames))));
                iAUC(i,j) = trapz(time(1:3),RSI(1:3));
                [peak,int] = max(RSI);
                ttp(i,j) = time(int);
                fo = fit(transpose(time(round(L/2):end)), ...
                    RSI(round(L/2):end),'poly1');
                lincoeff = coeffvalues(fo);
                washout(i,j) = lincoeff(1);
            end
        end
    end
    catch
    continue
    end
    semiquant(k).AUC = AUC;
    semiquant(k).iAUC = iAUC;
    semiquant(k).timeToPeak = ttp;
    semiquant(k).washout = washout;
end


% The following part calculates the Brix-model parameters by using the least
% squares algorithm provided by lsqcurvefit. It also allows for plotting the
% data and the fitted Brix model consequtively for visual inspection.

%Define the fitting function:
Brix = @(x,t)(x(1)*x(2)*((exp(-x(2)*t)-exp(-x(3)*t))/(x(3)-x(2))));
ub = [8,5,5]; lb = [0.0,0.0,0.0];%Upper and lower bounds for the parameters
x0 = [0.1,0.03,0.001];           %Initial guess value
dt = 15;

opts = optimset('lsqcurvefit');
optimset(opts,'Display','off');

tc = linspace(0,400,1000);
for k = 1:size(patients,2)
```

```
if any(k==omit) == 0;
    patient = patients{k};
    firstFrame = firstFrames(k);
    roi = ROI{k};
    slicenb = slice(k);
    %Create mask of index tumor:
    bw = roipoly(patient(:,:,slicenb),roi(:,1),roi(:,2));
    t = linspace(0,dt*(size(patient,3)-firstFrame), ...
        size(patient,3)-firstFrame+1);
    abrix_bilde = zeros(size(patient,1));
    kep_bilde = zeros(size(patient,1));
    kel_bilde = zeros(size(patient,1));
    resnorm_bilde = zeros(size(patient,1));
    rsi = cell2mat(RSI_int(k));
    residual = zeros(size(patient,1),30-firstFrame+1);
    s0 = zeros(size(patient,1),size(patient,2));
    for i = 1:size(patient,1)
        for j = 1:size(patient,2)
            if bw(i,j) == 1  %Only values in index tumor are calculated
                ydata = transpose(squeeze(rsi(i,j,:)));
                [s_fit,resnorm,res] = lsqcurvefit(Brix,x0,t, ...
                    ydata,lb,ub,opts);
                abrix_bilde(i,j) = s_fit(1);
                kep_bilde(i,j) = s_fit(2);
                kel_bilde(i,j) = s_fit(3);
                resnorm_bilde(i,j) = resnorm;
                for m = 1:length(res)
                    residual(i,j,m) = res(m);
                end
              plot(tc,Brix(s_fit,tc))
              hold('on')
              plot(t,ydata,'*')
              hold('off')
              ylim([0,3.5])
              pause(1/10)

            end
        end
    end
```

```
%       The script stores the parameter images, as well as the residuals,
%       and the square sum of the residuals.
        Abrix_bilde(k) = {abrix_bilde};
        Kep_bilde(k) = {kep_bilde};
        Kel_bilde(k) = {kel_bilde};
        Resnorm_bilde(k) = {resnorm_bilde};
        residuals(k) = {residual};
    end

end

%Finally, all the calculated data are stored in one cell structure for easy
%access.
for i = 1:length(patients)
    results(i).image = patients{i};
    results(i).slice = slice(i);
    results(i).firstFrame = firstFrames(i);
    results(i).RSI = RSI{i};
    results(i).RSI_int = RSI_int{i};
    results(i).iAUC = semiquant(i).iAUC;
    results(i).AUC = semiquant(i).AUC;
    results(i).timeToPeak = semiquant(i).timeToPeak;
    results(i).washout = semiquant(i).washout;
    results(i).abrix = Abrix_bilde{i};
    results(i).kep = Kep_bilde{i};
    results(i).kel = Kel_bilde{i};
    results(i).roi = ROI{i};
    results(i).resnorm = Resnorm_bilde{i};
    results(i).residuals = residuals{i};
end

for i = 1:106
    resnorm = results(i).resnorm;
    s_res = sqrt(resnorm./(30-patient_data(i).firstFrame));
    results(i).s_res = s_res;
end


save('patient_data','patient_data','-v7.3')
```

```
function start = start_frame(Im)
% Callable function to determine the arrival of CA,
% it takes the sorted images of one patient as argument,
% and returns the frame number in which CA arrives.


means = zeros(size(Im,3),1);
for i = 1:size(Im,3)
    bilde = Im(:,:,i);
    means(i) = mean2(bilde);
    sd(i) = std(nonzeros(bilde));
end

noise = sqrt((Im(:,:,1)-Im(:,:,2)).^2);
mean = 0.5*(Im(:,:,1)+Im(:,:,2));
noise2 = sqrt((Im(:,:,2)-Im(:,:,3)).^2);

baseline = mean2(means(1:3));
st = std(means(1:3))/max(means);
sRel = (means-baseline)/max(means);
stRel = st/max(st);

% for j = 1:size(Im,3)
%     if means(j) > 1.2*thresh(k)
%         start(k) = j-2;
%         break
%     end
% end

treshold = 0.02;
for j = 1:size(Im,3)
    if sRel(j) > treshold
        %start(k) = j-1;
        start = j-1;
        break
    end
end

end
```

```
% Routine to extract and sort the clinical data, as well as sorting out
% misfits in the Brix-model, and calculating median and percentile values
% for correlation.

load('results.mat')
k_data = importfile('C:\FuncProst\141127_Database_til_K.xlsx');
pimo_data = xlsread('c:\FuncProst\141218 Storsnitt, fra konsensusm+ te.xlsx ');
pimo_score = pimo_data(:,2);

for i = 1:length(k_data.Patientnr)
    if isnan(k_data.Patientnr(i))
        continue
    else
    p = k_data.Patientnr(i);
    age(p) = k_data.Age(i);
    PSA(p) = k_data.PSA(i);
    cT(p) = k_data.cT(i);
    pT(p) = k_data.pT(i);
    GleasonBiop(p) = k_data.Glscorebiopsi(i);
    GleasonPat(p) = k_data.Glscorepat(i);
    Risk(p) = k_data.Risk_classification(i);
    size(p) = k_data.Largest_extent(i);
    end
end

for ii = 1:length(results)
    results(ii).age = age(ii);
    results(ii).largest_extent = size(ii);
    results(ii).PSA = PSA(ii);
    results(ii).GleasonBiop = GleasonBiop(ii);
    results(ii).GleasonPat = GleasonPat(ii);
    results(ii).cT = cT(ii);
    results(ii).pT = pT(ii);
    results(ii).risk = Risk(ii);
    results(ii).pimo = pimo_score(ii);
    results(ii).mediAUC = median(nonzeros(results(ii).iAUC));
    results(ii).medAUC = median(nonzeros(results(ii).AUC));
    results(ii).medTTP = median(nonzeros(results(ii).timeToPeak));
    results(ii).medWO = median(nonzeros(results(ii).washout));
```

```
    results(ii).medAbrix = median(nonzeros(results(ii).abrix));
    results(ii).medkep = median(nonzeros(results(ii).kep));
    results(ii).medkel = median(nonzeros(results(ii).kel));
end

IVcohort = results(1:53);
Pillcohort = results(54:end);

for k = 1:length(results)
    if isnan(median(nonzeros(results(k).abrix)))
        continue
    else
    abrix = results(k).abrix;
    kep = results(k).kep;
    kel = results(k).kel;
    for m = 1:256
        for n = 1:256
            if results(k).s_res(m,n)>0.4
                abrix(m,n) = 0;
                kep(m,n) = 0;
                kel(m,n) = 0;
            end
        end
    end
    if k < 54
        IVcohort(k).medAbrix = median(nonzeros(abrix));
        IVcohort(k).medkep = median(nonzeros(kep));
        IVcohort(k).medkel = median(nonzeros(kel));
    else
        p = p+1;
        Pillcohort(p).medAbrix = median(nonzeros(abrix));
        Pillcohort(p).medkep = median(nonzeros(kep));
        Pillcohort(p).medkel = median(nonzeros(kel));
    end
    end
end
```

```
% A routine for comparing the Brix model parameters between the index
% tumor and the rest of the prostate gland. This routine also performs
% the logistic regression, and generates the probability maps.

abrix_prost = nonzeros(extractfield(patient_data,'abrix_prost'));
abrix_tum = nonzeros(extractfield(patient_data,'abrix'));
kep_prost = nonzeros(extractfield(patient_data,'kep_prost'));
kep_tum = nonzeros(extractfield(patient_data,'kep'));
kel_prost = nonzeros(extractfield(patient_data,'kel_prost'));
kel_tum = nonzeros(extractfield(patient_data,'kel'));


[Ra,pa] = ttest2(abrix_prost,abrix_tum);
[Rkep,pkep] = ttest2(kep_prost,kep_tum);
[Rkel,pkel] = ttest2(kel_prost,kel_tum);


p = @(b,x)(exp(b(1)+b(2)*x(1)+b(3)*x(2)+b(4)*x(3))/(1+exp(b(1)+ ...
    b(2)*x(1)+b(3)*x(2)+b(4)*x(3))));

p_map = zeros(256,256,50);

for ii = 1:50
    if ii ~= 8
    s1 = length(nonzeros(patient_data(ii).abrix));
    s0 = length(nonzeros(patient_data(ii).abrix_prost));
    x1 = [nonzeros(extractfield(patient_data(ii),'abrix')); ...
        nonzeros(extractfield(patient_data(ii),'abrix_prost'))];
    x2 = [nonzeros(extractfield(patient_data(ii),'kep')); ...
        nonzeros(extractfield(patient_data(ii),'kep_prost'))];
    x3 = [nonzeros(extractfield(patient_data(ii),'kel')); ...
        nonzeros(extractfield(patient_data(ii),'kel_prost'))];
    y = [ones(s1,1);zeros(s0,1)];
    b = glmfit([x1 x2 x3],y,'binomial');

    abrix = patient_data(ii).abrix+patient_data(ii).abrix_prost;
    kep = patient_data(ii).kep+patient_data(ii).kep_prost;
    kel = patient_data(ii).kel+patient_data(ii).kel_prost;
    for m = 1:256
```

```
        for n = 1:256
            if abrix(m,n) == 0
                continue
            else
            x = [abrix(m,n);kep(n,m);kel(m,n)];
            p_map(m,n,ii) = p(b,x);
            end
        end
    end
    else
        continue
    end
    patient_data(ii).p_maps = p_map(:,:,ii);
end
```

```
%Callable function for calculating the similarities between two images

function [DiceCoef,JaccardCoeff] = DICE(roi,p_map)

% set one image non-zero values as 200
roi(roi>0)=200;

% set second image non-zero values as 300
p_map(p_map>0)=300;

% set overlap area 100
OverlapImage = p_map-roi;

% count the overlap100 pixels
[r,~,~] = find(OverlapImage==100);
countOverlap100=size(r);

% count the image200 pixels
[r1,~,~] = find(roi==200);
img1_200=size(r1);

% count the image300 pixels
[r2,~,~] = find(p_map==300);
img2_300=size(r2);

% calculate Dice Coef
DiceCoef = 2*countOverlap100/(img1_200+img2_300);
JaccardCoeff = countOverlap100/(img1_200+img2_300-countOverlap100);
end
```

```
% Routine for identifying the optimal probability cutoff to maximize
% the similarity between the probability maps and the location of the
% primary tumor.

clearvars -except patient_data prob_map

cutoff = linspace(0,1,101);
dice_coeff = zeros(100,1);
jaccard_coeff = zeros(100,1);
maxdice = zeros(50,1);

figure()
for k = 1:50
    for i = 1:100
        patient = k;
        try
        roi_mask = 1*roipoly(patient_data(patient).image(:,:,patient_data(patient)
        prob_mask = 1*(p_map(:,:,k) > cutoff(i));

        [JaccardCoeff, DiceCoeff] = DICE(roi_mask,prob_mask);
        dice_coeff(i) = DiceCoeff;
        jaccard_coeff(i) = JaccardCoeff;
        catch
            continue
        end
    end
    str = sprintf('Pasientnummer %i',k);
    plot(jaccard_coeff,'b')
    hold('on')
    plot(dice_coeff,'r')
    %title(str)
    xlabel('cutoff-p')
    ylim([0,1])
    %pause(0.3)
    %hold('off')
   [maxdice(k),ind(k)] = max(jaccard_coeff);

  best_cutoff(k) = cutoff(ind(k));
    patient_data(k).dice = dice_coeff;
```

```
    patient_data(k).jaccard = jaccard_coeff;
end

threshold = mean(best_cutoff);
CO = round(mean(ind));
for ii = 1:50
    J = patient_data(ii).jaccard;
    D = patient_data(ii).dice;
    Jac(ii) = J(CO);
    Dic(ii) = D(CO);
end


histogram(Jac,10,'DisplayStyle','stairs','EdgeColor','k')
hold('on')
histogram(Dic,10,'DisplayStyle','stairs','EdgeColor','r')
legend('Jaccard coefficients','Dice coefficients')
ylim([0,20])
xlabel('Similarity coefficients')
```